

Dynamics and Structure of Ionic Liquids by Means of Neutron Scattering

Dissertation

zur Erlangung des Grades
des Doktors der Naturwissenschaften
der Naturwissenschaftlich-Technischen Fakultät III
Chemie, Pharmazie, Bio- und Werkstoffwissenschaften
der Universität des Saarlandes.



UNIVERSITÄT
DES
SAARLANDES

von
TATSIANA BURANKOVA

Saarbrücken
2014

Tag des Kolloquiums: 05.06.2014
Dekan: Prof. Dr. Volkhard Helms
Berichterstatter: Prof. Dr. Rolf Hempelmann
Prof. Dr. Dieter Richter
Vorsitz: Prof. Dr. Michael Springborg
Akad. Mitarbeiter: Dr. Volker Huch

Acknowledgements

First and foremost I would like to express my sincere appreciation to my scientific supervisor Jan P. Embs for dedicating so many hours of his time to discussing current results of my work, answering my questions, teaching many practical things concerning the experimental part of the project on FOCUS and proofreading this thesis. I owe my deepest gratitude to Prof. Rolf Hempelmann for giving me the opportunity to work in this project, to participate in the priority program of the German Research Foundation on Ionic Liquids and for his review of this thesis. The experiments would not have been possible without the samples synthesized by Verlainé Fossog, whom I would also like to express my gratitude.

I would like to thank Ekaterina Pomjakushina for her technical support and explanations on DSC-measurements and Tom Fennell for his help in experiments on FOCUS. The experimental work in this thesis would not have been possible without the assistance of the instrument scientists at ILL and FRM II: Andrew Wildes, Goran Nilsen, Tilo Seydel, Jacques Ollivier and Giovanna Simeoni.

I wish to thank all my colleagues at Paul Scherrer Institute for friendly and positive work atmosphere. Life at PSI would not be the same were it not for Verena Städele, Lothar Holitzner, Fanni Juranyi, Stefan Ochsenbein, Thomas Gahl, Matthias and Anna Frontzek, Matti Forster and many others. I am grateful to Christian Rüegg and Christof Niedermayer for resolving administrative and organizational issues.

Lastly, I want to thank my family for their constant encouragement and support.

Abstract

This thesis describes neutron scattering experiments on the materials class of ionic liquids (IL), which has attracted considerable research interest in the past few years due to a range of properties, contributing to their potential as chemical, catalytic and electrochemical reaction media. Many different techniques have been applied to investigate their structure, while there are still plenty of open questions concerning microscopic dynamics in these materials. As a method sensitive to the presence of hydrogen atoms, quasielastic neutron scattering (QENS) was employed to study stochastic motions of ILs with hydrogen-rich cations on the time scale of 0.1–100 ps.

The QENS-spectra of pyridinium-based ILs as well as one alkylammonium-based protic IL have been investigated in a wide temperature range. To consider dynamics on the broadest possible time scale, instruments with different instrumental resolutions were used. While the low-temperature dynamics can be envisaged as thermally activated rotations of the end methyl groups, two distinct dynamical processes can be resolved for higher temperatures. They were ascribed to the unrestricted diffusion and tangled localized processes characterized by similar relaxation times (chain and ring librations, conformational changes, rotations). In order to evaluate their time and spatial characteristics, theoretical models, which could satisfactorily capture this diversity, were proposed.

Furthermore, neutron scattering experiments were also carried out on partially deuterated samples. Owing to the difference in the scattering cross-section of deuterium and hydrogen, the deuterated parts of the ion become masked for the used method. This provided means to disentangle the localized motions of the pyridinium-based ILs and to study the enhanced proton dynamics in the protic ionic liquid.

A rare experiment on separation of coherent and spin-incoherent scattering in ILs was performed. It allowed disclosing the collective nature of the diffusional process in a butyl-pyridinium IL. The spatially restricted motions of the butyl chain and the pyridinium ring were proved to be true single particle dynamics.

Zusammenfassung

Diese Arbeit beschäftigt sich mit der Untersuchung ausgewählter ionischen Flüssigkeiten (IL) mittels quasielastischer Neutronenstreuung. Dank einer Reihe von Eigenschaften, die das Potenzial dieser Substanzklasse als chemisches, katalytisches und elektrochemisches Reaktionsmedium stärken, haben ionische Flüssigkeiten erhebliches Forschungsinteresse in den letzten Jahren erregt. Viele verschiedene Techniken wurden zur Erforschung ihrer Struktur angewendet, dennoch gibt es immer noch eine große Anzahl offener Fragen hinsichtlich der makroskopischen Dynamik in diesen Materialien. Da quasielastische Neutronenstreuung (QENS) gegenüber Wasserstoff empfindlich ist, wurde diese Methode zur Untersuchung von stochastischen Bewegungen dieser Salze mit wasserstoffreichen Kationen im Zeitraum von 0.1–100 ps eingesetzt.

Die QENS Spektren von pyridiniumbasierten ILs und einer alkylammoniumbasierten protischen IL wurden in einem großen Temperaturbereich analysiert. Spektrometer mit unterschiedlichen zeitlichen Auflösungen wurden benutzt, um die dynamischen Prozesse auf einer möglichst großen Zeitskala untersuchen zu können. Während die Tieftemperaturdynamik als die thermisch aktivierte Rotation der Methyl-Endgruppen beschrieben werden kann, wurden zwei verschiedene Prozesse bei höheren Temperaturen aufgelöst. Diese Prozesse entsprechen zum einen der langreichweitigen Diffusion und zum zweiten miteinander gekoppelten lokalisierten Prozessen, die durch ungefähr gleiche Relaxationszeiten charakterisiert sind (Libration der Alkylkette bzw. des Pyridiniumringes, Konformationsänderungen, Rotation). Um ihre zeitlichen und räumlichen Charakteristika zu bestimmen, wurden theoretische Modelle vorgeschlagen, die die Vielfalt der Prozesse erfassen.

Weiterhin wurden Neutronenstreuungsexperimente an Proben mit teil deuterierten Kationen durchgeführt. Infolge des Unterschieds der Streuquerschnitte von Deuterium und Wasserstoff werden die deuterierten Teile des Kations bei der angewendeten Methode maskiert. Durch die so präparierten Proben gelang es die lokalisierten dynamischen Prozesse aufzulösen.

Der Einsatz polarisierter Neutronen ermöglichte die experimentelle Trennung von kohärenten und spin-inkohärenten Streubeiträgen. Dadurch konnte gezeigt werden, dass der

Diffusionsprozess in den pyridiniumbasierten ILs einen kollektiven Charakter besitzt. Die räumlich beschränkten Bewegungen der Butyl-Kette und des Pyridinium-Rings erwiesen sich als echte Ein-Teilchen-Dynamik.

Contents

Acknowledgements	iii
Abstract	iv
Abbreviations	ix
1 Introduction	1
1.1 General information	1
1.2 Motivation and outline of the thesis	6
2 Theoretical principles of thermal neutron scattering	9
2.1 Neutron cross section	9
2.2 Polarisation analysis	12
2.3 Analysis of stochastic motions	13
2.3.1 Self-diffusion	16
2.3.2 Jump diffusion	16
2.3.3 Three-fold jump rotation	17
2.3.4 Continuous rotational diffusion	17
2.3.5 Diffusion in a sphere	18
2.3.6 Gaussian model for localized translational motion	19
3 Materials and Methods	21
3.1 Materials	21
3.1.1 Synthesis and characterisation	23
3.1.2 Characterization by differential scanning calorimetry (DSC)	23
3.1.3 Neutron scattering cross sections of the studied ILs	25
3.2 Neutron scattering methods and instruments	27
3.2.1 Time-of-flight spectrometers	27
3.2.2 Separation of coherent and spin-incoherent scattering by means of polarized neutrons	28
3.2.3 Neutron backscattering	32
4 Data reduction and analysis	35

4.1	Raw data reduction	35
4.2	2D-fitting routine	37
5	Cation dynamics in pyridinium-based ILs	43
5.1	Low-temperature dynamics in [BuPy][Tf ₂ N]	44
5.2	Model independent analysis of the liquid state	48
5.3	Dynamic structure factor models for pyridinium-based ILs	50
5.3.1	Dynamic structure factor for the alkyl chain and the pyridinium ring	54
5.3.2	Dynamic structure factor for the totally protonated pyridinium-based cations	60
5.4	Exploring the relaxation time landscape of the cationic dynamics	64
5.5	Summary	69
6	Cation dynamics in a PIL	71
6.1	Low-temperature dynamics in TEA-TF	72
6.2	Dynamic structure factor for TEA-TF	75
6.3	Summary	82
7	Collective and single particle dynamics	83
7.1	Incoherent contribution	84
7.2	Coherent contribution	88
7.3	Summary	90
8	General conclusions and outlook	93
	Bibliography	97

Abbreviations

[BuPy]	1-butylpyridinium
[C₁₂Py]	1-dodecylpyridinium
DSC	Differential scanning calorimetry
EISF	Elastic incoherent structure factor
ESR	Electron spin resonance
FWHM	Full width at half maximum
FRM II	Forschungsreaktor München II
HWHM	Half width at half maximum
IL	Ionic liquid
ILL	Institut Laue Langevin
INS	Inelastic neutron scattering
MD	Molecular dynamics
MSD	Mean squared displacement
NMR	Nuclear magnetic resonance
[NTf₂] = [TFSI]	Bis(trifluoromethylsulfonyl)imide or triflate
OKE	Optical Kerr effect
PFG-NMR	Pulsed field gradient nuclear magnetic resonance
PIL	Protic ionic liquid
QENS	Quasielastic neutron scattering
SAF	Self attenuation factor
SINQ	Swiss Spallation Neutron Source
SSF	Self shielding factor
TEA	Triethylammonium
TF	Trifluoromethanesulfonate
TOF	Time-of-flight

1. Introduction

1.1. General information

Ionic Liquids (ILs) or molten salts as a class of compounds have aroused a burgeoning scientific interest in the past decades [1, 2] due to their benign properties for many present and potential industrial applications [3]. These materials are usually defined as salts with relatively low melting points, or as salts, which are in the liquid state at room temperature. The class includes diverse compounds, their number being estimated to be around 10^6 in comparison to 600 conventional organic solvents [3, 4]. Despite this huge number, there are still several common properties, which mark out these neoteric materials:

- high thermal stability;
- high electrochemical stability;
- negligible vapor pressure;
- wide liquid range (melting temperatures below 100 °C);
- nonflammability under ambient conditions;
- glass forming ability;
- good solvents for polar solutes;
- tunable catalytic ability;
- high viscosity.

The properties of ionic liquids result from a complex interplay of intermolecular interactions between ions, their geometry and charge distribution. An IL usually consists of an organic cation of low symmetry and an organic or inorganic anion [1, p. 1–40]. Therefore all possible universal (Coulomb, van der Waals, dipole-dipole) and specific (for example H-bonding) intermolecular interactions can define the behaviour of ILs. Coulomb's law governs the long-range order in simple salts, whereas the van der Waals interaction softens electrostatic forces in ionic liquids owing to the bulky size of the ions and their asymmetric shape

with possibly various substituents. As a result ILs exhibit less ordering; their characteristic melting points fall relative to those of simple salts. In addition, ILs may also form an amorphous glass on cooling [5–7]. In comparison with common molecular solvents ILs are characterized by charge ordering that extends over larger distances than usual density oscillations, one could expect for a liquid, as well as mesoscopic organisation may occur [8, 9]. Thus, exactly the above mentioned stronger interaction between charged particles leads to those properties, which distinguish ILs from conventional organic solvents and arose a number of research fields, where organic solvents can be substituted by ILs.

As ILs are characterized by negligible vapour pressure and considered to be nonvolatile, it is common that ILs are often mentioned as “environmentally friendly” compounds in connection with the concept of “green chemistry” [2, 10–12]. Non volatility is also essential for the applicability of ILs as effective catalysts, for their recovery and reuse [13, 14]. Their polar nature facilitates physical adsorption when used as lubricants; high thermal and electrical conductivity being valuable properties, which promote heat dissipation during sliding [15]. Furthermore, high thermal stability is crucial for the usage of ILs as heat transfer fluids [16]. ILs can dissolve extensive quantities of lignocellulosic biomass, which is necessary for efficient production of bioethanol and biodiesel [17, 18]. ILs have started to be exploited for separation of CO₂ from flue gas or natural gas, resulting in higher combustion efficiencies [19], for gas storage and reversible adsorption of pollutant gases [20].

An extremely fruitful application field of ILs is electrochemistry [21], where their intrinsic electrical conductivity is used directly. As electrolytes, these materials can be exposed to a high potential difference without undergoing redox reactions, owing to their wide electrochemical windows. Here is a far from exhaustive list of possible applications of ILs: solar cells [22–24], fuel cells [25], organic conductors and superconductors [26], batteries [27–29], capacitors [30], transistors [31], electrochemical sensors [32, 33], electrodeposition [30, 34].

A relatively new group of ILs are room temperature magnetic ionic liquids, which exhibit promising magnetic, photophysical/optical and electrochromic behaviour [35].

ILs have indeed proved to be multifunctional solvents. One of the reasons for this popularity is a relative easiness to tune physical-chemical properties of this class of materials. A structural variation of the cation or anion may lead to a new IL with targeted functionality. Therefore these materials are often referred to as designer solvents or task specific ILs [1, 13].

So far, the last years have shown that these compounds are of considerable interest for various fields. A huge number of potential cation and anion families and their many derivatives allow the desired properties for specific application to be selected. That is why a deeper insight into the fundamental properties of ILs is of the essence to realize the maximum potential of ILs. Regarding the structure of ILs, there is a huge number of research papers

published on both experimental and theoretical investigations [8, 24, 28, 36–47], which allow access to the information about the correlation between bulk properties and morphology in the liquid and solid state [48, 49].

However, structure knowledge is only a static snapshot of complex interactions in ILs, whereas the majority of fields of usage mentioned above require the knowledge of their dynamical characteristics such as viscosity, diffusivity, conductivity. Diversity and tunability of ILs drive search for prediction of their physicochemical properties. In this situation molecular dynamics (MD) simulations have become an invaluable tool for understanding of intra- and intermolecular processes and analysing transport properties of ILs [49–51]. This approach is crucial, because experimental investigation of even a fraction of these compounds were infeasible, to say nothing of synthesizing all possible and potentially useful cation-anion compositions. MD simulations give access not only to the above mentioned transport characteristics, but reveal their mutual relationship with each other, predict their temperature dependent trends, capture dynamical behaviour not only of different species (cations, anions) and their collective excitations, but also of their parts (alkyl chain or ring librations). A MD investigation of 1-N-butyl-3-methylimidazolium bis(trifluoromethanesulfonyl)imide [52] showed that the cations possess higher diffusivity than the anions despite their bigger size and bulky shape. In consequence of non-uniform distribution of the counter-ions around the imidazolium cation the direction along the plane of the ring becomes preferential for translational motion. As it also turned out, the cations feature a broader frequency range of dynamical processes than the anions do. In addition, the simulations predicted the existence of ion pairs characterized by the lifetime of 0.3 ps. Urahata and Ribeiro proposed in their paper [53] that the alkyl chain of the 1-alkyl-3-methylimidazolium cation started its fast rattling and libration on a subpicosecond scale in a temperature range below the actual melting point of the crystal, after which much slower translational and reorientational diffusion sets in. Their later paper [49] was devoted to collective excitations in 1-butyl-3-methylimidazolium chloride, where the authors demonstrated that the flexible alkyl chain damps acoustic modes along its direction.

Theoretical investigations performed on ILs so far have shown that ILs feature dynamical heterogeneity on a broad time-scale. For example, mean squared displacement (MSD) curves usually show up several regions, which can be attributed to a ballistic regime at short times, an intermediate cage regime and a diffusive regime at long times [54–57]. Especially the plateaulike behaviour at intermediate times is of great importance. It is commonly referred to as β -relaxation and is typical for supercooled liquids and glass forming systems [58]. Del Popolo and Voth [57] also interpreted the large difference between the relaxation rotational times and mean collision times of velocity correlations functions as a sign of the existence

of long-lived cages, in which ions are rattling surrounded by their counter ions. Quite a compelling finding made by Hu and Margulis [54] is that there are subsets of more and less mobile particles clustered in space and marked by correlated dynamics. Similarly, the signatures of mutual diffusion (i.e., strong coupling of the motion of both the anion and the cation) were pointed out by Habasaki and Ngai [56]. This distinguishes ILs from conventional liquids, which are homogeneous.

No doubt, MD simulations possess tremendous predictive potential. But the basics of any classical MD simulation is an empirical force field [59], by means of which complex interactions between charged particles of ILs are modelled. So simulation results totally depend on the quality and accuracy of the chosen force field. Quite often calculated dynamical parameters from MD simulations are over- or underestimated. Therefore, experimental data are required to refine force fields and validate their empirical parameters [60], although strongly increasing power of computational resources provides means for application of more expensive but precise methods [61]. Thus experimental methods remain of great importance. Several techniques can provide information about dynamics in ILs: NMR, ESR, dielectric spectroscopy, optical Kerr effect, luminescence and neutron scatterings spectroscopy [62, 63]. These methods probe various dynamical processes on different time-scales and whatever experimental approach is used, pronouncedly heterogeneous, broadly distributed dynamics of ILs are indicated.

Pulsed gradient resonance NMR technique is an informative tool for studying diffusion in the time-window of several milliseconds [64–66]. For example, complicated diffusional behaviour of halogen-free boron based ILs was observed from the stimulated echo diffusion decays [67]. At lower temperatures the cations and anions are characterized by different diffusion coefficients, which can be related to the two liquid phases of this IL. Owing to “hydrophobic interaction” of the hydrocarbon chains there are slower regions enriched by the cations, while anions are included mostly to faster phases. As the temperature rises this heterogeneity gradually disappears and the transport properties of ions are described by one diffusion coefficient.

By means of time-resolved fluorescence spectroscopy and anisotropy measurements solvation processes can be analysed on the time-scale from nanoseconds to picoseconds [68]. These data are valuable for description of diffusion limited reactions and their rates in ILs. Fluorescence relaxation functions often show non-exponential time dependence, thus providing evidence for several relaxation pathways. Solvent modes on a time scale from sub-100-fs to 200-ps can be investigated by optical Kerr effect (OKE) spectroscopy [9, 69–72]. The polarization-anisotropy decay is influenced in this range by diffusive reorientation motion of individual molecules or ion-pairs (several picoseconds and more), intermolecular librational

motions (on a 100-fs to 1-ps time scale) and intramolecular vibrational motions (on a sub-100-fs time scale). As a rule, ILs (in particular imidazolium based ILs) are characterized by a broadly distributed spectrum in the wavenumber range of 0–200 cm^{-1} and several out-of-plane librational modes of the ring can be detected. These non-diffusive dynamics affect chemical reaction rates and, therefore, are an interesting object for investigation [71]. In a combined dielectric relaxation and optical Kerr effect study Turton et al. [72] observed an intense additional low-frequency relaxation mode (sub- α) in comparison with the fundamental single “molecule” α -relaxation. The sub- α process implies a fluctuation in a mesoscale aggregation, for example, in cation-stacked or micelle-like clusters. Xiao et al. [9, 69, 70] focused on the temperature dependence of the OKE spectra of 1,3-pentylmethyimidazolium cations; the observed temperature dependence was ascribed to the existence of density inhomogeneity due to nanostructurally organized domains, i.e. polar and nonpolar regions.

Quasielastic neutron scattering (QENS) and inelastic neutron scattering (INS), which have been demonstrated to be an informative tool for studying different materials [73–75], can be applied as well to yield comprehensive information about various stochastic processes ranging from a fraction of picoseconds to nanoseconds in ILs [76, 77]. Incoherent neutron spectroscopy is particularly sensitive to hydrogen atoms and can be applied to unravel the dynamics of hydrogen-rich materials. In comparison with the other above mentioned spectroscopic techniques, QENS and INS allow measuring both energy- and momentum transfer of scattered neutrons and thus to simultaneously derive information about both time and space characteristics of studied processes. The kinetic energy of cold and thermal neutrons fits excitation energies in condensed matter, the length scales explored in an experiment being comparable with the wavelength of incident neutrons, which is of the order of interatomic distances in solids and liquids. For X-rays with a wavelength of a few Å the energy amounts to several keV, whereas for Raman or Brillouin light scattering the energy range corresponds to excitation energies in condensed matter, but the wavelength is far too large. Typical parameters, amenable to evaluation in a QENS-experiment, are vibrational displacements, jump distances, correlation lengths, diffusion coefficients, reorientational times and so on. Moreover, the (E, Q) -range covered in QENS and INS corresponds to the range probed in molecular dynamic simulations, so that this experimental method can be used to prove the accuracy of computations.

The first papers on QENS investigation of imidazolium-based IL were published in 2003 [77, 78]. The authors studied dynamics of these ILs over a broad temperature range. In the first paper Roche et al. discussed the nature of the phase transitions at lower temperatures and observed the effect of alkyl chain motion on the increase of anion mobility and thus of conductivity at low temperature by means of the backscattering technique. The further

research on [bmim][PF₆] was focused on a higher temperature range, when the IL is in the liquid state. Two different relaxation processes have been detected. The faster of the two motions exhibited neither a Q - nor T -dependence; this fast β -process was attributed to the motion of the molecules inside a cage. The slow α -process, on the other hand, showed a non-Debye and non-Arrhenius behaviour. A finer resolution of the BASIS spectrometer provided a better insight into the latter diffusional process and allowed to distinguish between its two components (true unrestricted and spatially constrained diffusion), which are typically approximated by a single stretched exponential α -process [76, 79]. Since the first publications a decade has passed, during which almost only neat ILs have been studied by means of neutron scattering [76, 79–81], although some recently published papers are devoted to the investigation of an IL in ordered mesoporous carbon [82, 83], which is used in battery and capacitor applications. However, the number of these publications remains very limited.

1.2. Motivation and outline of the thesis

Despite the impressive activities in the field and numerous complimentary techniques applied for studying ILs, a clear microscopic picture is still missing and thus highly demanded. On the other hand, QENS may provide comprehensive details on the dynamics, being connected with the other methods as well (dielectric spectroscopy, optical Kerr spectroscopy, molecular dynamics simulations). Nevertheless, neutron scattering methods have not been extensively used over the past decade and some of their advantages (deuteration labelling, polarization analysis) have not been employed at all. This fact determined the main objectives of this thesis.

The overall structure of the work will be as follows:

In Chapter 2 theoretical concepts of cold and thermal neutron scattering, relevant for data interpretation, are presented and several analytical models, employed for the description of the spectra, are outlined.

Chapter 3 provides a summary of the combination of experimental techniques used and of corresponding technical aspects; it introduces the compounds, chosen for this work, and some of their physicochemical properties.

As one of the main features of ILs is their decidedly heterogeneous dynamics and, hence, theoretical models, which can be applied to describe their QENS-spectra, include a number of parameters, a more robust approach in fitting experimental data to analytical expressions is required. Therefore, a program module for the 2D-fitting routine was elaborated in the framework of this thesis and is briefly presented in Chapter 4.

Chapter 5 deals with two compounds, which represent a special class of pyridinium-based ILs and differ by the length of the alkyl substituent in the cation. The aim of this part of the work was to establish the influence of the alkyl chain length on the cation dynamics on a picosecond time scale in a wide temperature range. Partial deuteration was used to attain a better understanding of the spatially restricted processes of the alkyl-pyridinium cation.

Chapter 6 is intended to present a QENS-study on a protic ionic liquid with the focus on the dynamics of the proton, which serves as a charge carrier and allows anhydrous conductivity, important for designing electrochemical devices.

Chapter 7 addresses the issue of collective and single-particle dynamics in ILs and demonstrates the influence of the structure and local environment on the stochastic processes: long-range diffusion and spatially restricted dynamics. This insight was provided by means of experimental separation of coherent and spin-incoherent scattering.

The results obtained within the research activities and summarized in this thesis have been fully or partially published in peer-reviewed scientific journals and conference proceedings as listed below:

1. J. P. Embs, T. Burankova, E. Reichert, R. Hempelmann. Cation dynamics in the pyridinium based ionic liquid 1-N-butylpyridinium bis((trifluoromethyl)sulfonyl) as seen by quasielastic neutron scattering. *The Journal of Physical Chemistry B*, 116(44):13265–13271, 2012
2. J. P. Embs, T. Burankova, E. Reichert, V. Fossog, and R. Hempelmann. QENS study of diffusive and localized cation motions of pyridinium-based ionic liquids. *Journal of the Physical Society of Japan*, 82(Suppl.A):SA003, 2013

Publications in preparation:

1. T. Burankova, E. Reichert, V. Fossog, R. Hempelmann, J. P. Embs. The Dynamics of cations in pyridiniumbased Ionic Liquids by means of quasielastic and inelastic neutron scattering. *Journal of Molecular Liquids* (accepted)
2. T. Burankova, V. Fossog, R. Hempelmann, J. P. Embs. Collective ion diffusion and localized single particle dynamics in pyridinium-based ionic liquids
3. T. Burankova, V. Fossog, R. Hempelmann, J. P. Embs. Proton diffusivity in the protic ionic liquid triethylammonium triflate probed by QENS

2. Theoretical principles of thermal neutron scattering

Almost all experiments in this work were performed using neutron scattering methods and their advantages for studying hydrogen-rich materials were shortly mentioned in the Introduction. Many years of the successful application of this experimental technique have led to the publication of several excellent and comprehensive textbooks [73, 74, 84, 85], as well as some reviews [86–89], which differ by how rigorous theoretical aspects are treated and so address a broad, multidisciplinary audience. The intention of the present chapter is to provide reference to the relevant terms, concepts and models, which are employed for the analysis of the acquired neutron scattering data.

2.1. Neutron cross section

During an elementary scattering event the neutron undergoes a change in momentum and can lose or gain energy. This is the key to determine the structure and the dynamics of the target. The basic quantity directly measured in neutron scattering experiment is the number of neutrons scattered per second into a solid angle $d\Omega$ ($d\Omega = dS/r^2$ see Fig. 2.1) with final energy between E and $E + dE$, or the double differential cross section

$$\frac{d^2\sigma}{d\Omega dE}$$

Figure 2.1 displays the typical geometry of scattering experiment. The incident neutrons with the wavevector \vec{k}_i ($k_i = |\vec{k}_i|$), which are described by a planar wave,

$$\psi_i = \exp(ik_i z) \tag{2.1}$$

interact with the target and are scattered by it. As the scattering is spherically symmetric for thermal neutrons, the wavefunction of the scattered neutrons with the wavevector \vec{k}_f in

the direction θ , ϕ at the distance r from the target can be written in the form of a spherical wave

$$\psi_{sc} = -\frac{b}{r} \exp(ik_f r) \quad (2.2)$$

where b denotes the scattering length and is independent of the direction, at which the neutrons are scattered. The value of the scattering length is determined by the type of the particular nucleus (isotope) and the spin state of the nucleus-neutron system.

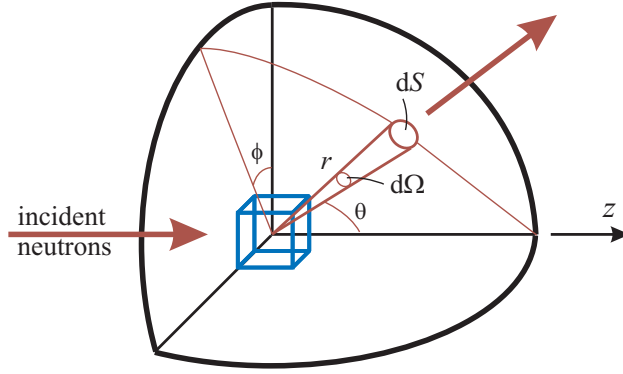


Figure 2.1. Geometry of a scattering experiment

The neutron has spin $1/2$. If it is scattered by a nucleus with a non-zero spin I , then the spin of the nucleus-neutron system is either $I + 1/2$ or $I - 1/2$ with different scattering lengths b^+ and b^- , respectively. So the interaction of the neutron spin $1/2$ with nuclear spins produces two states with total spins parallel or antiparallel. This creates some kind of distribution of scattering lengths over the whole sample. The corresponding average scattering lengths read

$$\langle b \rangle = \left(\frac{I+1}{2I+1} \right) b^+ + \left(\frac{I}{2I+1} \right) b^- \quad (2.3)$$

$$\langle b^2 \rangle = \left(\frac{I+1}{2I+1} \right) (b^+)^2 + \left(\frac{I}{2I+1} \right) (b^-)^2 \quad (2.4)$$

It is necessary to mention that some distribution can be caused by the presence of different isotopes as well. But as the scattering by hydrogen nuclei, characterized by the incoherent scattering cross section 10–20 times larger than other scattering cross sections, will be in the focus of this work, in other words, a system with only one species, the theory concerning isotopic incoherent scattering will be omitted.

The total double differential cross section can be presented as the sum of the coherent and incoherent contribution.

$$\frac{d^2\sigma}{d\Omega dE} = \left(\frac{d^2\sigma}{d\Omega dE} \right)_{\text{coh}} + \left(\frac{d^2\sigma}{d\Omega dE} \right)_{\text{inc}} \quad (2.5)$$

The summands have the following physical interpretation. The coherent scattering could be observed from the same system, where all the particles have the same value b of the scattering length. The deviation of the actual system from this ideal one gives the origin to the incoherent scattering. The total double differential cross section can be also expressed via the dynamic structure factor, or the scattering law $S(Q, E)$ as follows

$$\frac{d^2\sigma}{d\Omega dE} = N \frac{k_f}{k_i} \left\{ \frac{\sigma_{\text{coh}}}{4\pi} S_{\text{coh}}(Q, E) + \frac{\sigma_{\text{inc}}}{4\pi} S_{\text{inc}}(Q, E) \right\} \quad (2.6)$$

where $\sigma_{\text{coh}} = 4\pi\langle b \rangle^2$ and $\sigma_{\text{inc}} = 4\pi(\langle b^2 \rangle - \langle b \rangle^2)$ are the coherent and incoherent cross sections, N is the number of nuclei in the scattering system. Henceforth $E = E_f - E_i$ stands for the energy transfer and $\vec{Q} = \vec{k}_f - \vec{k}_i$ denotes the wavevector transfer. The next expression determines connection between the dynamic structure factor and inter-particle correlations and their time evolution.

$$S_{\text{coh}}(Q, E) = \frac{1}{2\pi\hbar} \sum_{jj'} \int_{-\infty}^{\infty} \langle e^{\{-i\mathbf{Q}\mathbf{r}_j(0)\}} e^{\{i\mathbf{Q}\mathbf{r}_{j'}(t)\}} \rangle \exp\left(-i\frac{E}{\hbar}t\right) dt \quad (2.7a)$$

$$S_{\text{inc}}(Q, E) = \frac{1}{2\pi\hbar} \sum_j \int_{-\infty}^{\infty} \langle e^{\{-i\mathbf{Q}\mathbf{r}_j(0)\}} e^{\{i\mathbf{Q}\mathbf{r}_j(t)\}} \rangle \exp\left(-i\frac{E}{\hbar}t\right) dt \quad (2.7b)$$

Formulas 2.7a–2.7b express the both contributions in terms of the position operators of the particles of the scatterer. One can notice that the equation for the coherent contribution contains the double sum over j, j' and the equation for the incoherent scattering contains only the simple sum over j . To put it differently, the coherent scattering originates from interference effects, as it depends on the correlations between the positions of the different nuclei at different times including the correlation between the positions of the same nucleus at different times. Since the incoherent scattering depends only on the correlation between the positions of the same nucleus at different times, it has another physical interpretation and is described as single-particle scattering.

The Van Hove correlation functions [90] allow another form of the mathematical expressions 2.7a–2.7b.

$$S_{\text{coh}}(Q, E) = \frac{1}{2\pi\hbar} \int_{-\infty}^{\infty} G(\mathbf{r}, t) \exp\left(i\left(\mathbf{Q}\mathbf{r} - \frac{E}{\hbar}t\right)\right) d\mathbf{r} dt \quad (2.8a)$$

$$S_{\text{inc}}(Q, E) = \frac{1}{2\pi\hbar} \int_{-\infty}^{\infty} G_s(\mathbf{r}, t) \exp\left(i\left(\mathbf{Q}\mathbf{r} - \frac{E}{\hbar}t\right)\right) d\mathbf{r} dt \quad (2.8b)$$

The coherent contribution is related to the time-dependent correlation function $G(\mathbf{r}, t)$, which provides information about the correlation between the presence of another particle or the same particle in position $\mathbf{r}' + \mathbf{r}$ at time $t' + t$ and the presence of a particle in position \mathbf{r}' at time t' [90]. Otherwise stated, it is the probability that, if an atom is at the origin of the chosen reference system at time 0, an atom will also be found within unit volume at \mathbf{r} at time t [84]. The incoherent contribution is related to the self part of the Van Hove function $G_s(\mathbf{r}, t)$, to the probability of finding at \mathbf{r} and time t the atom that was at the origin at time 0. So the Van Hove functions have intuitively clear physical meaning and can be applied for both classical and quantum systems.

2.2. Polarisation analysis

The only experimental way to unambiguously separate coherent and spin-incoherent contributions is to make use of polarized neutrons. A time-of-flight experiment with polarization analysis implies that one simultaneously measures the change in direction and energy of the scattered neutrons, as well as the change in the spin state upon scattering [91–93]. The double differential cross section for a scattering process, in which the neutron spin changes from state s_i to s_f , while the scattering system goes from state q_i to q_f reads [91]

$$\frac{d^2\sigma^{s_f s_i}}{d\Omega dE} = \sum_{q_i} P_q \sum_{q_f} \frac{k_f}{k_i} \left(\frac{m_n}{2\pi\hbar^2}\right)^2 \left| \left\langle s_f q_f \left| \int d\mathbf{r} e^{i\mathbf{Q}\mathbf{r}} V(\mathbf{r}) \right| s_i q_i \right\rangle \right|^2 \times \delta\left(\frac{\hbar^2}{2m_n}(k_f^2 - k_i^2) + E\right) \quad (2.9)$$

where P_q is the probability that the system is in the initial state q_i and $V(r)$ is the interaction potential. Then the total double differential cross section is a sum over all possible initial and final states of both the neutron and the nuclei. In terms of atomic scattering amplitudes $U_i^{s_f s_i}$ the double differential cross section is given by

$$\frac{d^2\sigma^{s_f s_i}}{d\Omega dE} = \sum_{q_i} P_q \sum_{q_f} \frac{k_f}{k_i} \left| \left\langle q_f \left| \sum_i e^{i\mathbf{Q}\mathbf{r}} U_i^{s_f s_i} \right| q_i \right\rangle \right|^2 \delta\left(\frac{\hbar^2}{2m_n}(k_f^2 - k_i^2) + E\right) \quad (2.10a)$$

$$U_i^{s_f s_i} = \langle s_f | (b_i - p_i \mathbf{S}_{\perp i} \cdot \boldsymbol{\sigma} + B_i \mathbf{I}_i \cdot \boldsymbol{\sigma}) | s_i \rangle \quad (2.10b)$$

where $\boldsymbol{\sigma}$ is the neutron-spin operator, \mathbf{I} is a nuclear-spin operator, B is the spin-dependent nuclear amplitude, and p is the magnetic amplitude. \mathbf{S}_{\perp} is defined in terms of the atomic-spin operator \mathbf{S}

$$m_n = 1,675 \cdot 10^{-27} \text{ kg}$$

$$\hbar = 1,055 \cdot 10^{-34} \text{ m}^2\text{kg/s}$$

$$\mathbf{S}_{\perp} = \hat{S} - (\hat{S} \cdot \hat{Q}) \hat{Q} \quad (2.11)$$

If the initial neutron spin states are designated as \uparrow and \downarrow , and the final spin states are denoted in the same way, then four atomic scattering amplitudes can be calculated using the properties of the Pauli-spin operators

$$U^{\uparrow\uparrow} = \langle b \rangle - pS_{\perp z} + BI_z \quad (2.12a)$$

$$U^{\downarrow\downarrow} = \langle b \rangle + pS_{\perp z} - BI_z \quad (2.12b)$$

$$U^{\uparrow\downarrow} = -p(S_{\perp x} + iS_{\perp y}) + B(I_x + iI_y) \quad (2.12c)$$

$$U^{\downarrow\uparrow} = -p(S_{\perp x} - iS_{\perp y}) + B(I_x - iI_y) \quad (2.12d)$$

$U^{\uparrow\uparrow}$ and $U^{\downarrow\downarrow}$ do not change the neutron spin state after a scattering event and therefore are commonly referred to as the non-spin-flip amplitudes. The $U^{\uparrow\downarrow}$ and $U^{\downarrow\uparrow}$ involve a change in the spin state and are known as the spin-flip amplitudes. It is evident upon examination of Eq. 2.12 that coherent nuclear scattering is always non-spin-flip scattering.

In the case of a nonmagnetic system ($\mathbf{S}_{\perp} = 0$) and randomly oriented nuclear spins ($\bar{I}_x = \bar{I}_y = \bar{I}_z = 0$) the cross section per atom can be written, after the averaging procedure [92], as follows:

Coherent scattering	Incoherent scattering
$\frac{d\sigma^{\uparrow\uparrow}}{d\Omega} = \frac{d\sigma^{\downarrow\downarrow}}{d\Omega} = 4\pi\langle b \rangle^2$	$\frac{d\sigma^{\uparrow\uparrow}}{d\Omega} = \frac{d\sigma^{\downarrow\downarrow}}{d\Omega} = 4\pi\frac{1}{3}B^2I(I+1)$
$\frac{d\sigma^{\uparrow\downarrow}}{d\Omega} = \frac{d\sigma^{\downarrow\uparrow}}{d\Omega} = 0$	$\frac{d\sigma^{\uparrow\downarrow}}{d\Omega} = \frac{d\sigma^{\downarrow\uparrow}}{d\Omega} = 4\pi\frac{2}{3}B^2I(I+1)$

As it was stated earlier, the coherent nuclear scattering is purely non-spin flip. The nuclear spin-incoherent scattering has both contributions: spin-flip and non-spin-flip. Nevertheless, the ratio between these contributions is 1 to 2, irrespective of the incident polarization direction, which makes it feasible to perform separation of the coherent and spin-incoherent neutron scattering on the basis of this theory.

2.3. Analysis of stochastic motions

For cold and thermal neutrons' ($5 \cdot 10^{-5} \div 0.025$ eV) energy gain or loss during a single scattering event due to stochastic motions of the particles (diffusion or rotation) makes up a comparable fraction of their initial kinetic energy. The method of QENS investigates these small amounts of energy exchange with spectral distribution, centred at the elastic position

with zero energy transfer. In the case of hydrogen rich materials the origin of this broadening is single-particle dynamics and the nature of scattering is incoherent.

For ionic liquids one can allow for self-diffusion, rotational motion on the whole and of different parts and vibration behaviour of the ions. Assuming no correlation between these motions (as their energy scale differs greatly), one defines the dynamic structure factor as a convolution of the corresponding dynamic structure factor for different types of motions.

$$S(Q, E) = S_{\text{trans}}(Q, E) \otimes S_{\text{rot}}(Q, E) \otimes S_{\text{vib}}(Q, E) \quad (2.15)$$

Vibrations and torsional vibrations are usually outside the accessible energy range of QENS experiments; in the quasielastic region the vibrations are considered to contribute only to the intensity through the Debye-Waller factor $\exp(-2W)$ [73]. The elastic or quasielastic intensity is reduced with Q due to the energy redistribution to the inelastic region. Thus, the incoherent scattering law in the quasielastic region is a convolution of the translational (global) and rotational (localized) dynamic structure factors, multiplied by a Debye-Waller factor.

$$S(Q, E) = \exp(-2W)S_{\text{glob}}(Q, E) \otimes S_{\text{loc}}(Q, E) \quad (2.16)$$

In the model-independent approach the global and localized dynamics can be presented by a Lorentzian function:

$$S_{\text{glob}}(Q, E) = \frac{1}{\pi} \frac{\Gamma_{\text{glob}}(Q)}{\Gamma_{\text{glob}}^2(Q) + E^2} \quad (2.17)$$

$$S_{\text{loc}}(Q, E) = \text{EISF}(Q)\delta(E) + [1 - \text{EISF}(Q)] \frac{1}{\pi} \frac{\Gamma_{\text{loc}}(Q)}{\Gamma_{\text{loc}}^2(Q) + E^2} \quad (2.18)$$

The two linewidths Γ_{glob} and Γ_{loc} describe the broadening in the energy domain caused by the global and local dynamic processes, respectively. $\text{EISF}(Q)$ in Eq. 2.18 stands for the elastic incoherent structure factor of the localized motion and provides insight into the geometry of the spatial confinement, in which the localized process occurs. This concept was introduced by Lechner in 1971 [74, 87] and is very helpful for the extraction of structural information on confined motions. Its physical meaning can be interpreted in terms of the self-part of the Van Hove correlation function $G_s(\mathbf{r}, t)$, which can be split into the sum of its asymptotic value in the long-time limit and a time-dependent term:

$$G_s(\mathbf{r}, t) = G_s(\mathbf{r}, \infty) + G'_s(\mathbf{r}, t) \quad (2.19)$$

$G_s(\mathbf{r}, \infty)$ equals 0 for long range diffusion or it is a finite non-zero function of \mathbf{r} in the case of a localized motion, whereas $G'_s(\mathbf{r}, t)$ tends to 0 as $t \rightarrow \infty$. After Fourier transformation (Eq. 2.8b–2.19) the dynamic structure factor satisfies the relation:

$$S(Q, E) = S_{\text{el}}(Q)\delta(E) + S_{\text{qe}}(Q, E) \quad (2.20)$$

A closer inspection of Eq. 2.18 and 2.20 shows that the intensity of the elastic line is directly related to the EISF. On the other hand, the elastic line is the result of the diffraction on the particle spatial distribution taken at infinite time and averaged over all its possible initial positions. Therefore, it is possible to derive information about spatial characteristics of localized processes in quite a straightforward way from incoherent scattering.

The simplest form of the incoherent dynamic structure factor (Eq. 2.16–2.18) has been successfully applied to a number of complex systems, such as macromolecules (proteins, DNA) [94–97], or medium-chain alkanes [98, 99], or compounds with alkyl substituents [100–102]. Hence, this model-independent approach can be considered as a good starting point for the interpretation of QENS data on ILs.

The distribution of wavevector and energy transfers, given by the dynamic structure factor, would be detected, when a monochromatic neutron beam is scattered by the probe. In consequence of beam divergence, uncertainties in flight paths and, as a result, uncertainties in wavelengths, sample and detector thickness, every spectrometer is characterized by a certain resolution $R(Q, E)$. Therefore, correction for resolution distortion [103] has to be carried through. Accordingly, the following form of the scattering law, which contains a convolution operation with the resolution function, should be used to fit experimental spectra

$$S_I(Q, E) = I_0(Q) \cdot [S(Q, E) \otimes R(Q, E)] + a + bE \quad (2.21)$$

where $I_0(Q)$ includes an intensity factor and the Debye-Waller factor; the term $a + bE$ represents a linear background, which accounts for processes faster than the instrument range.

The model-independent approach provides means to estimate the number of processes distinguishable on the time-scale of a measuring apparatus, to judge their character (unrestricted diffusion or confined motions), to estimate some parameters. However, it is quite a descriptive method. For more comprehensive analysis theoretical models of stochastic motions have to be included in the dynamic structure factor.

2.3.1 Self-diffusion

The small Q -range ($0.1\text{--}0.5 \text{ \AA}^{-1}$) is favourable to explore motions occurring over “large” distances ($R = 2\pi/Q \sim 10\text{--}60 \text{ \AA}$) as, for example, self-diffusion. In this case the self-part of the Van Hove correlation function obeys Fick’s second law with the self-diffusion coefficient D_S :

$$\frac{\partial}{\partial t} G_S(\mathbf{r}, t) = D_S \Delta G_S(\mathbf{r}, t) \quad (2.22)$$

This yields the dynamic structure factor in the form of one Lorentzian curve [73, 74]:

$$S(Q, E) = \frac{1}{\pi} \frac{\hbar D_S Q^2}{(\hbar D_S Q^2)^2 + E^2} \quad (2.23)$$

It is a rare case when the simple self-diffusion model satisfactorily describes long-range dynamics in a broader Q -range [104, 105]. In practice one deals with more complicated mechanisms of diffusion, which require a more sophisticated theoretical treatment. Nevertheless, the so-called Q^2 -law is generally valid at small Q -values.

2.3.2 Jump diffusion

The jump diffusion model proposed by Singwi and Sjölander [106] has become quite popular for the description of global molecular motions in liquids [76, 79, 81, 107, 108]. The authors derived the differential cross section for the case when a particle oscillates for a mean time τ_0 and then diffuses continuously for a mean time τ_1 , repeatedly changing the type of movement. The probabilities that the particle remains in the state of either oscillatory or diffusive motion were presumed to decay exponentially with time. It was established that the shape of quasielastic broadening is, in general, not a Lorentzian, but can be reduced to it for the limiting case ($\tau_1 \ll \tau_0$). In this case the HWHM then reads:

$$\Gamma(Q) = \frac{\hbar D Q^2}{1 + D Q^2 \tau_0} \quad (2.24)$$

with the actual diffusion coefficient given by

$$D = \frac{R^2 + l^2}{6(\tau_0 + \tau_1)} \quad (2.25)$$

where l^2 is the mean squared displacement during the time τ_1 in the diffusion mode; R^2 is the mean squared radius of the fully developed thermal cloud in the oscillatory motion.

The analogous formula can be obtained from a slightly different approach based on a modification of the Chudley–Elliott model [109], in which a particle is enclosed in a cage

formed by other atoms or molecules and from time to time performs a jump into a neighbouring cage. For liquids the jump lengths can not be determined by the lattice constant and their distribution can be taken into account. In the particular case of Eq. 2.24 an exponential distribution of jump lengths is assumed.

2.3.3 Three-fold jump rotation

The three-fold jump rotation model is a particular instance of the general jump model among N sites for $N = 3$ [110, 111]. If the probabilities of finding a particle at all three sites located on the circumference of a circle are identical, the dynamic structure factor for a powder sample is

$$S(Q, E) = \frac{1}{3} \left(1 + 2j_0(QR\sqrt{3}) \right) \delta(E) + \frac{2}{3} \left(1 - j_0(QR\sqrt{3}) \right) \frac{1}{\pi} \frac{3\hbar/(2\tau)}{(3\hbar/(2\tau))^2 + E^2} \quad (2.26)$$

where R is the circle's radius, τ is the residence time at any site and $j_0(x)$ is the zeroth-order spherical Bessel function.

The three-fold jump rotation model is of importance for analysing thermally activated hopping of methyl groups over energy barriers [112–116], as it is justifiable to assume that methyl substituents move in a three-fold potential with three equivalent energy minima.

2.3.4 Continuous rotational diffusion

Localized dynamics of methyl groups [113] or freely rotating small molecules [107, 117–119] can be envisaged and modelled as rotational diffusion on the surface of a sphere. In other words, the orientation vector of the particle $\boldsymbol{\Omega}$ performs small-angle random rotations, the orientation probability $P(\boldsymbol{\Omega}, t)$ obeying Fick's second law [73, 110]:

$$\frac{\partial}{\partial t} P(\boldsymbol{\Omega}, t) = D_R \Delta_{\Omega} P(\boldsymbol{\Omega}, t) \quad (2.27)$$

where D_R stands for the rotational diffusion coefficient and has the dimension of inverse time. Instead of D_R the relaxation time for rotation $\tau_R = 1/6D_R$ may be used. Analytical calculations lead to the following incoherent scattering function:

$$S(Q, E) = j_0^2(QR)\delta(E) + \sum_{k=1}^{\infty} (2k+1)j_k^2(QR) \frac{1}{\pi} \frac{k(k+1) \frac{\hbar}{6\tau_R}}{\left(k(k+1) \frac{\hbar}{6\tau_R}\right)^2 + E^2} \quad (2.28)$$

where R is the rotational radius and $j_k(x)$ is the k -th order spherical Bessel function. It should be noted that in praxis only a limited number of the summands (5–10) is used, because the higher order terms of the series converge quickly to zero.

2.3.5 Diffusion in a sphere

The next model considers a particle diffusing in the interior of a sphere with an impermeable surface or, in other words, in the infinite potential well of spherical symmetry [120]. This theoretical system is realized in a number of real physical situations [76, 99, 121] and is used to describe internal or restricted dynamics. If the radius of the sphere is denoted as a , the diffusion coefficient of the localized motion is denoted as D , then the incoherent scattering law reads:

$$S(Q, E) = A_0^0 \delta(E) + \frac{1}{\pi} \sum_{\{l,n\} \neq \{0,0\}} (2l+1) A_n^l(Q) \frac{(x_n^l)^2 D/a^2}{((x_n^l)^2 D/a^2)^2 + E^2} \quad (2.29)$$

where the structure factors A_n^l are expressed in the following way:

$$A_n^l(Q) = \frac{6(x_n^l)^2}{(x_n^l)^2 - l(l+1)} \left[\frac{Qa j_{l+1}(Qa) - l j_l(Qa)}{(Qa)^2 - (x_n^l)^2} \right]^2, \quad Qa \neq x_n^l, \{l, n\} \neq \{0, 0\} \quad (2.30a)$$

$$= \frac{3}{2} j_l^2(x_n^l) \frac{(x_n^l)^2 - l(l+1)}{(x_n^l)^2}, \quad Qa = x_n^l, \{l, n\} \neq \{0, 0\} \quad (2.30b)$$

In particular the EISF is

$$A_0^0 = \left[\frac{3j_1(Qa)}{Qa} \right]^2, \quad \{l, n\} = \{0, 0\} \quad (2.31)$$

For $Qa \rightarrow \infty$ the analytical expression of the QENS broadening reduces to one Lorentzian with the linewidth recovering the DQ^2 -behaviour. In general, the scattering law already resembles that of unrestricted translational diffusion for $Qa > \pi$, whereas it is similar to the rotational model for $Qa < \pi$.

The first 99 coefficients x_n^l were numerically computed and can be found in the original work by Volino [120]. Unfortunately, the series in Eq. 2.29 is slowly convergent and for a proper direct fitting routine and parameter evaluation at least these 100 summands are required. To circumvent the problem, elastic intensity and hence EISF can be determined first, which gives access to the radius of the sphere. However, it is important to be sure in this case that the linewidth of the resolution function is much narrower than D/a^2 and the elastic line is really well separated.

2.3.6 Gaussian model for localized translational motion

The model for localized dynamics based on Gaussian statistics is close to the previous one, but it considers the restricted diffusion in a confinement with a “soft” boundary. As the analytical expression of this model is much simpler, its application may be in many cases more advantageous in comparison with more robust calculations for the diffusion in a sphere model. It is necessary to mention that this model has been only recently introduced by Volino et al. [122] and it has been tested on a handful of real systems [123–125].

In contrast to the previous model, a continuous and infinitely derivable potential is used, that corresponds to restricted dynamics in a sphere with a soft boundary. For a one-dimensional case the displacement of a particle moving along the x -axis is assumed to be a centred Gaussian random variable, for which the normalized equilibrium density probability $p(u_x)$ reads:

$$p(u_x) = \frac{1}{\sqrt{2\pi\langle u_x^2 \rangle}} \exp \left[-\frac{u_x^2}{2\langle u_x^2 \rangle} \right] \quad (2.32)$$

Assuming that the process is stationary, the correlation function $\rho(t)$ of this variable is given by

$$\langle u_x(t)u_x(0) \rangle = \sigma^2 \rho(t) \quad (2.33)$$

where $\sigma^2 = \langle u_x^2 \rangle$ characterizes the size of the domain, in which the particle is diffusing. The boundary conditions of the correlation function are $\rho(0) = 1$ and $\rho(\infty) = 0$. For a three dimensional case ($\langle u_x^2 \rangle = \langle u_y^2 \rangle = \langle u_z^2 \rangle$) the intermediate scattering function $I(Q, t)$ has the following form:

$$I(Q, t) = \exp \left[-Q^2 \langle u^2 \rangle (1 - \rho(t)) \right] \quad (2.34)$$

Different functional expressions can be used to describe how the memory about the initial position is lost. The simplest form is, however, exponential with the characteristic time τ_0 :

$$\rho(t) = \exp \left(-\frac{t}{\tau_0} \right) \quad (2.35)$$

At this point one can define the diffusion coefficient of the localized motion D_{loc} :

$$D_{\text{loc}} = \langle u^2 \rangle / \tau_0 = \sigma^2 / \tau_0 \quad (2.36)$$

Its physical meaning becomes more clear in the limiting case of an infinite medium, in other words, for $Q^2 \langle u^2 \rangle \ll 1$. It is evident upon examination of Eq. 2.34 that $I(Q, t)$ will

have significant values only when $\rho(t) \rightarrow 1$ or from Eq. 2.35 when $t/\tau_0 \ll 1$. Then the intermediate scattering function in the first approximation equals:

$$I(Q, t) \approx \exp \left[-Q^2 \langle u^2 \rangle \frac{t}{\tau_0} \right] \quad (2.37)$$

Equation 2.37 recovers the usual law for continuous diffusion in an infinite medium with the diffusion coefficient expressed by Eq. 2.36.

In order to change to the frequency or energy domain, the intermediate scattering function can be written in the form of a series expansion:

$$\begin{aligned} I(Q, t) &= A_0(Q) + \sum_{n=1}^{\infty} A_n(Q) \rho(t)^n = \\ &= A_0(Q) + \sum_{n=1}^{\infty} A_n(Q) \exp \left(-\frac{nt}{\tau_0} \right) \end{aligned} \quad (2.38)$$

where the elastic ($n = 0$) and quasielastic ($n > 0$) incoherent structure factors $A_n(Q)$ are given by

$$A_0(Q) = \exp [-Q^2 \sigma^2] \quad (2.39a)$$

$$A_n(Q) = \exp [-Q^2 \sigma^2] \frac{(Q^2 \sigma^2)^n}{n!} \quad (2.39b)$$

After performing Fourier transform with respect to time

$$S(Q, E) = \frac{1}{2\pi\hbar} \int_{-\infty}^{\infty} I(Q, t) \exp(-i\frac{E}{\hbar}t) dt \quad (2.40)$$

and expressing τ_0 through D_{loc} , the final formula for the incoherent scattering law can be obtained:

$$S(Q, E) = e^{-Q^2 \sigma^2} \left[\delta(E) + \sum_{n=1}^{\infty} \frac{(Q^2 \sigma^2)^n}{n!} \frac{1}{\pi} \frac{\hbar n D_{\text{loc}} / \sigma^2}{(\hbar n D_{\text{loc}} / \sigma^2)^2 + E^2} \right] \quad (2.41)$$

For practical issues it is necessary to truncate the series expansion, which is not an ideal case for the high- Q region. Nevertheless, the comparison of Eq. 2.41 and 2.29–2.31 shows a definite advantage of the Gaussian model: it involves only a single-index series, which turns out to be better convergent as well. Moreover, it is likely to better describe real physical systems because of the soft boundary.

3. Materials and Methods

3.1. Materials

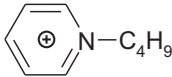
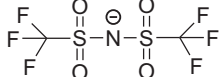
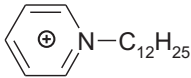
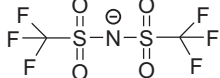
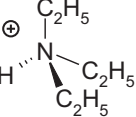
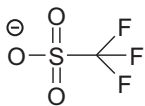
A large number of different classes of ILs exist. Some of them have been extensively investigated by different methods. Examples are imidazolium, pyridinium, phosphonium, quaternary ammonium, and pyrrolidinium salts. In this work, it has been decided to focus on those ILs, which fulfil the following requirements:

- ILs chosen for the study should be relatively well-known and some data on their most common properties should be available in the literature;
- compounds should possess promising properties from the point of view of possible applications;
- ILs should contain an organic cation rich with hydrogen atoms, so that one can profit from an intense incoherent signal in a QENS-experiment; at the same time, no hydrogen atoms should be included in the anion structure in order to simplify the analysis;
- in order to make advantage of deuterium labelling, a possibility to synthesize partially deuterated samples should exist.

The choice has been made in favour of the compounds listed in Table 3.1. The two first ILs belong to the class of pyridinium-based salts. Recently Docherty [126] et al. have shown that they are generally more environmentally friendly, concerning biodegradability, than their more popular imidazolium-based counterparts. Besides, they show some beneficial properties for such applications as dye-sensitized solar cells [127] and ionogels, based on the confinement of an IL in a thermally stable inorganic skeleton [128]. This family of ILs has been also selected because the cation can be easily modified concerning the alkyl chain length.

The third compound is a representative of a sub-class of protic ionic liquids (PIL) [129], which are produced by combining a Brønsted acid and a Brønsted base. The main advantages of PILs arise from their anhydrous proton conductivity. A proton is transferred from the acid to the base, leading to the presence of proton-donor and -acceptor sites and hence

Table 3.1. List of ionic liquids investigated

compound	cation structure	anion structure	abbreviation
1-butylpyridinium bis(trifluoromethylsulfonyl)imide			[BuPy][Tf ₂ N]
1-dodecylpyridinium bis(trifluoromethylsulfonyl)imide			[C ₁₂ Py][Tf ₂ N]
trifluoromethanesulfonyl of triethylammonium			TEA-TF

of a hydrogen-bond network. The proton conductivity of PILs is of interest for fuel cells, dye-sensitive solar cells, or double-layer electrochemical capacitors. TEA-TF studied in this work was reported to be applicable for high-temperature proton exchange membrane fuel cells (HT-PEMFC) [130, 131] and for electro-catalytic oxidative cleavage of lignin [17].

Table 3.2. Physical properties of the studied ionic liquids

	[BuPy][Tf ₂ N]	[C ₁₂ Py][Tf ₂ N]	TEA-TF
molecular weight M , g/mol	416.363	528.579	252.277
mass density (25 °C) ρ , g/cm ³	1.4547 ^[132] 1.4476 ^[133] 1.4539 ^[134]	1.2488 ^[133]	1.2546 ^[135] 1.41 ^[136]
self-diffusion coefficient (117 °C) $D_{\text{cation}} \cdot 10^{-10}$, m ² /s	2.940 ^[134, 137]	–	2.110 ^[130]
self-diffusion coefficient (117 °C) $D_{\text{anion}} \cdot 10^{-10}$, m ² /s	2.428 ^[134, 137]	–	1.820 ^[130, 136]

Table 3.2 summarizes recently published physical properties of the studied ILs relevant for this work. Diffusion coefficients are measured by means of PFG-NMR and their temperature dependence follows Vogel-Fulcher-Tamman equation, which is quite common for supercooled liquids. Information on [C₁₂Py][Tf₂N] is not available, but comparing viscosity data for pyridinium-based ILs, one can expect the diffusion coefficient to be less than that of [BuPy][Tf₂N]. Oliveira et al. [138] assumed that it can be connected with the formation of both charged and non-polar microstructures, the latter being formed by the alkyl chains.

In the case of TEA-TF self-diffusion coefficients were determined for three types of particles: trifluoromethanesulfonate (TF), triethylammonium (TEA) and H^+ . It turned out that all three species are characterized by different mobility. The diffusion coefficients of H^+ and TEA are similar but higher than that of TF. It proves that the amine mainly provides proton transport [130, 136].

3.1.1 Synthesis and characterisation

All the samples were obtained from the research group of Professor Hempelmann, Saarland University, Saarbrücken. They were synthesized and purified, using previously published methods [125]. The partially deuterated ILs were prepared by the same procedure, but with deuterated educts. The samples were stored as dry as possible in a desiccator, as the different water content may substantially influence physicochemical properties of ILs. The water content (< 150 ppm) was controlled by means of Karl Fischer titration, 1H NMR spectra were used to check the purity of the samples and the quality of partial deuteration ($98.16 < \%D < 99.70$). The complete list of the used samples is presented below:

1. [BuPy][Tf₂N] or [NC₅H₅-C₄H₉][Tf₂N]
2. [Bu_DPy][Tf₂N] or [NC₅H₅-C₄D₉][Tf₂N] (chain deuterated)
3. [BuPy_D][Tf₂N] or [NC₅D₅-C₄H₉][Tf₂N] (ring deuterated)
4. [C₁₂Py][Tf₂N] or [NC₅H₅-C₁₂H₂₅][Tf₂N]
5. TEA-TF or [NH(C₂H₅)₃][SO₃CF₃]
6. TEA_D-TF or [NH(C₂D₅)₃][SO₃CF₃] (partially deuterated)

3.1.2 Characterization by differential scanning calorimetry (DSC)

For characterization of the studied ionic liquids, determination of the temperatures of phase transitions, DSC measurements have been carried out with a Netzsch DSC 204F1 System. Measurements were performed on heating and cooling with a rate of 5–10 K/min using 20–30 mg samples encapsulated in standard Al crucibles with a pinhole at the top of them. An empty aluminium crucible was used as a reference. An argon stream served as a protective gas during the whole experiment. The samples were dried in situ in the differential scanning calorimeter by holding the sample at 100 °C for 30 minutes. It is important, because it is often reported that the presence of water can affect the glass transitions and melting temperatures [6, 7]. Measurements were performed on cooling the samples from 100 °C to -150 °C, followed by heating from -150 °C to 100 °C. Melting and crystallization temperatures were determined as the onset of the transition both at the rate of 5 °C/min and 10 °C/min.

Table 3.3. Temperatures of crystallization (T_{cr}), cold-crystallization (T_{cc}) and melting (T_m) obtained from the DSC-curves shown in Fig. 3.1

cycle	transition [°C]	5 K/min	10 K/min	literature
[BuPy][Tf ₂ N]				
cooling	T_{cr}	-37.0	-19.0	-
heating	T_m	24.5	24.5	26 ^[134]
[C ₁₂ Py][Tf ₂ N]				
cooling	T_{cr}	-3.0	-5.0	-
heating	T_{m1}	-38.0	-38.0	-
	T_{cc}	-11.5	-6.5	-
	T_{m2}	14.0	14.0	-
TEA-TF				
cooling	T_{cr}	-22.0	-26.0	-
heating	T_{cc}	-82.5	-77.5	-72.5 ^[139]
	T_{m1}	-45.0	-43.5	-43.5 ^[139]
	T_{m2}	27.5	28.5	32.0 ^[139]

The main sources of uncertainty in the temperature measurements are inexact placement of the sample in the furnace and instrument variability. In addition, even slight impurities in ILs, especially traces of water, are likely to cause larger errors than any other uncertainties and lead to non-reproductive results [6]. Furthermore, the DSC curves of all samples exhibit distinct dependence on the temperature history and scanning rate. Both crystallization and cold crystallization points are affected by the rate of cooling or heating. Nevertheless, the onset points for melting peaks seem to be independent of the applied heating/cooling rate. Table 3.3 contains the results of the measurements and the reported literature values.

The main feature common for all of the three DSC-traces (Fig. 3.1) is a huge difference between the temperature of crystallization on cooling and the temperature of melting on heating. Many ILs as glass forming materials can be supercooled below the melting temperature by as much as 50 or even 200 °C [7]. However, weak glass transitions were not detected with confidence on the obtained DSC-curves. The characteristic changes in the heat capacity were too small to see a significant step in the traces.

Three types of thermal behaviour have been differentiated for other ILs [6, 7]. The first group of ILs crystallizes on cooling and melts at a distinct temperature on heating. The DSC-trace of [BuPy][Tf₂N] demonstrates this behaviour under the experimental conditions

employed. The second group of ILs does not feature any true phase transition but only the formation of an amorphous glass. The third type of behaviour is characterized by the presence of so-called cold-crystallization peaks on heating. At first the compound turns from the glass to a subcooled liquid phase and then it actually crystallizes upon heating and undergoes melting at higher temperatures. $[\text{C}_{12}\text{Py}][\text{Tf}_2\text{N}]$ and TEA-TF can be assigned to the last type of behaviour. Besides, TEA-TF has two melting transitions on the obtained DSC-curves, which are usually ascribed to melting of the water-TEA-TF (~ 28 °C) and the pure PIL (~ 44 °C) domains, respectively [139, 140]. It is worth noting that comparison of the two pyridinium-based ILs shows the same tendency observed for imidazolium based ILs: the longer the alkyl chain, the lower the melting temperature is [66].

3.1.3 Neutron scattering cross sections of the studied ILs

The efficiency of interaction between an incident neutron and a target nucleus is represented by means of the quantity called nuclear cross section. As the neutron can be either scattered or absorbed by the target, the values of the scattering (σ_{scatt}) and absorption (σ_{abs}) cross sections, respectively, are of relevance for planning a neutron scattering experiment. The scattering cross-section can be further subdivided into coherent (σ_{coh}) and incoherent (σ_{inc}) scattering cross sections, which show whether collective effects or uncorrelated motions will influence the spectrum of the scattered neutrons. Table 3.4 summarizes the above mentioned cross sections of all the species investigated.

In order to minimize absorption effects, an annular hollow cylindrical sample holder made of aluminium was used. It has an outer diameter of 14.00 mm and an inner diameter of 12.60 mm, the thickness of the walls being equal 0.25 mm. That yielded the distance between the inner and outer cylinder of 0.20 mm. Such a sample thickness guarantees that neutron beam transmission through the sample exceeds 90 %. Thus, the effects of multiple scattering are negligible and unwanted absorption can be considered to be suppressed.

The values in Table 3.4 indicate that single-particle dynamics of the hydrogen-bearing cations is predominantly probed by neutrons, since hydrogen is a very strong incoherent neutron scattering element. The anions give rise only to coherent scattering, which nevertheless remains much less intense than the incoherent one. However, one can see that the situation can be drastically influenced by hydrogen–deuterium exchange. For that reason the analysis of the spectra in this work is generally based on the assumption that coherent contribution can be excluded from consideration. The cases, when it is not actually valid, will be discussed later in Chapter 7.

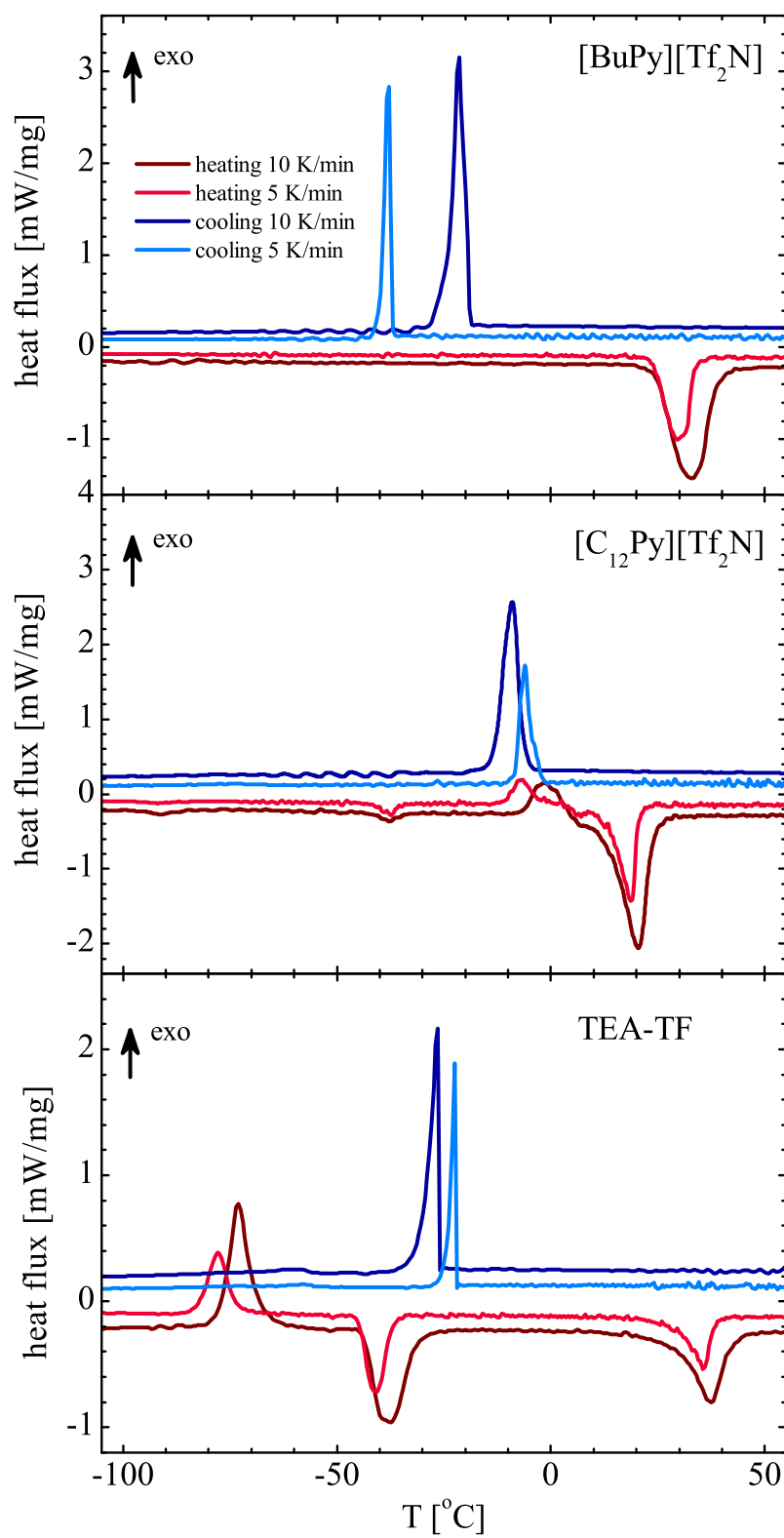


Figure 3.1. DSC traces observed on heating and cooling

Table 3.4. Summary of the neutron scattering cross sections of the studied species. σ_{abs} is given for neutrons with the wavelength of 5.75 Å. 1 b = 10^{-28} m².

	σ_{scatt} [b]	σ_{abs} [b]	σ_{inc} [b]	σ_{coh} [b]	$\frac{\sigma_{\text{inc}}}{\sigma_{\text{scatt}}}$ [%]
[Tf ₂ N]	65.70	9.68	0.52	65.18	0.80
[BuPy]	1209.87	21.07	1124.29	85.59	92.93
[BuPy][Tf ₂ N]	1275.58	30.74	1124.81	150.76	88.18
[Bu _D Py]	540.40	11.51	420.31	120.09	77.78
[Bu _D Py][Tf ₂ N]	606.10	21.19	420.83	185.27	69.43
[BuPy _D]	835.89	15.76	731.14	104.75	87.47
[BuPy _D][Tf ₂ N]	901.60	25.43	731.66	169.93	81.15
[C ₁₂ Py]	2566.74	38.18	2408.62	158.13	93.84
[C ₁₂ Py][Tf ₂ N]	2632.45	47.85	2409.14	223.31	91.52
TF	31.33	1.80	0.01	31.32	0.04
TEA	1357.27	23.16	1284.83	72.45	94.66
TEA-TF	1388.60	24.96	1284.84	103.77	92.53
TEA _D	241.48	7.23	129.95	111.53	53.82
TEA _D -TF	272.81	9.03	129.97	142.84	47.64

3.2. Neutron scattering methods and instruments

3.2.1 Time-of-flight spectrometers

Neutron time-of-flight spectroscopy is a powerful method, by means of which several points in the (Q, E) -space can be simultaneously detected. To obtain this, many time-resolved detectors are mounted to cover a large solid scattering angle. Energies of incident and scattered neutrons are calculated from the times the neutron travels a known distance.

The majority of the QENS experiments in this work were performed on the cold neutron time-of-flight spectrometer FOCUS (Fig. 3.2) at the Swiss spallation source SINQ [141–143]. Some additional measurements were carried out on the chopper time-of-flight spectrometers IN5 [144] at ILL and TOFTOF [145] at FRM2. All of the instruments have direct geometry and high flexibility in changing the wavelength of incident neutrons and hence the width of the resolution function ($\Delta\epsilon_{\text{res}}$). Figure 3.3 demonstrates the landscape of possible observation times ($\sim \hbar/\Delta\epsilon_{\text{res}}$) attainable on FOCUS for different monochromators and wavelengths of incident neutrons. Different parameters and settings of the spectrometers, which have been applied, are briefly summarized in Table 3.5. Empty sample holder runs at different

temperatures and vanadium runs were performed for every setting accordingly. The resolution of the spectrometers was determined either from the vanadium spectra or, when it was possible, from the spectra of the protonated samples at very low temperatures. The latter is more desirable, as the geometry of the experiment is completely reproduced, which is not the case for vanadium samples.

Table 3.5. Characteristics of the TOF-spectrometers

parameter	FOCUS	IN5	TOFTOF
incident wavelengths λ , Å	2.0–16.0	1.80–20.0	1.4–16.0
elastic energy resolution FWHM, μeV			
$\lambda=3.20$ Å	450	–	370
$\lambda=5.00$ Å	110	90	–
$\lambda=5.75$ Å	60	–	–
$\lambda=12.0$ Å	–	–	7.5
accessible Q -range, Å ⁻¹			
$\lambda=3.20$ Å	0.70–2.80	–	0.80–3.20
$\lambda=5.00$ Å	0.50–1.90	0.7–2.00	–
$\lambda=5.75$ Å	0.40–1.70	–	–
$\lambda=12.0$ Å	–	–	0.10–0.85
energy transfer range ΔE , meV			
$\lambda=3.20$ Å	[-6.0;6.0]	–	[-6.0;6.0]
$\lambda=5.00$ Å	[-2.0;2.0]	[-2.0;2.0]	–
$\lambda=5.75$ Å	[-1.4;1.4]	–	–
$\lambda=12.0$ Å	–	–	[-0.4;0.4]

3.2.2 Separation of coherent and spin-incoherent scattering by means of polarized neutrons

An experiment on separation of the coherent and spin-incoherent neutron scattering of the pyridinium-based ionic liquid [BuPy][Tf₂N] has been performed on the cold neutron multi-detector spectrometer with polarization analysis D7 at ILL [92, 146]. It had the option of polarizing the incident beam and equipped with supermirror analyser detector banks over a 132° angular range, allowing uniaxial and XYZ polarization analysis. A magnetic guide field of about 10–20 G (1.0–2.0 mT) is maintained along the path of the incident and scattered neutrons everywhere within D7 to preserve the spin state of the neutron. Using a vertically and horizontally focusing pyrolytic graphite monochromator incident neutrons of wavelength

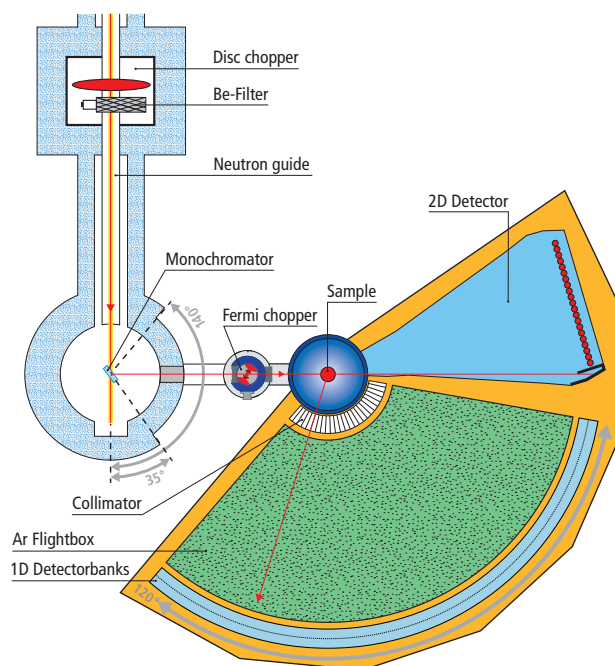


Figure 3.2. FOCUS instrument layout [141]

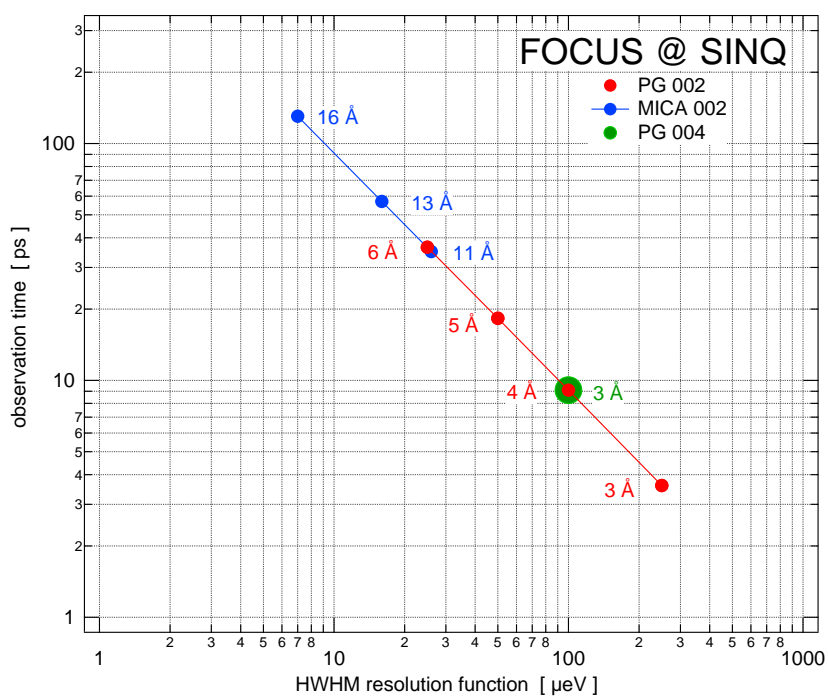


Figure 3.3. FOCUS observation time and energy resolution as a function of the wavelength of incident neutrons [141]

4.86 Å were selected. The addition of a Fermi chopper allowed us to take advantage of the TOF-mode with longitudinal polarization analysis. The efficiency of the detectors was calibrated by measuring a vanadium sample. The vanadium spectra were also used as the resolution function of the instrument, the corresponding energy resolution (FWHM) being equal to 0.14 meV. For the selected wavelength of incident neutrons the dynamic range amounted to $[-2.0;2.0]$ meV, the wavevector transfer covering the region of $0.6\text{--}2.2$ Å⁻¹.

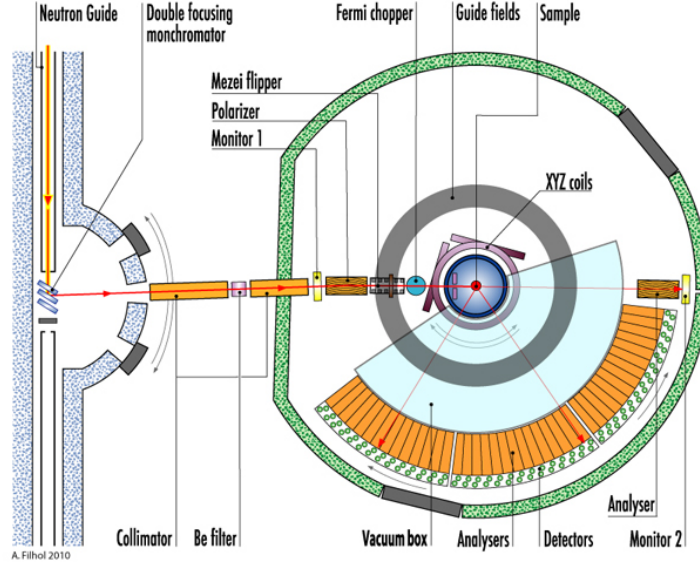


Figure 3.4. D7 instrument layout

As it follows from the theoretical principles of the polarization analysis considered in Chapter 2.2, the total scattering intensities without ($I_{\uparrow\uparrow}$, non-spin-flip intensity) and with ($I_{\uparrow\downarrow}$, spin-flip intensity) the change in the neutron-spin state are given by:

$$I_{\uparrow\uparrow} = I_{\text{coh}} + \frac{1}{3}I_{\text{inc}} \quad (3.1a)$$

$$I_{\uparrow\downarrow} = \frac{2}{3}I_{\text{inc}} \quad (3.1b)$$

Equations 3.1 are only valid in the ideal case; in practice the properties of the measuring equipment and its imperfections should be taken into consideration. The quality of the instrument is characterized by the quantity called “flipping ratio”, measured in an additional run for each detector with a quartz standard, which is a purely coherent scatterer in theory. Despite that, the scattering with the change in the neutron-spin state will be detected in a real experiment. Neither the polariser, nor the analysers are perfectly polarizing, the chopper producing additional depolarizing effect. Assuming that the quartz transmission was equal to 0.9, the flipping ratio $R = I_{\uparrow}/I_{\downarrow}$ was calculated for each detector (Fig. 3.5). The detectors, for which R -value was less than 5 were excluded from the further data reduction process. The

high 2θ -value range was affected most of all, resulting in the reduction of the theoretically possible Q -space, accessible for analysis.

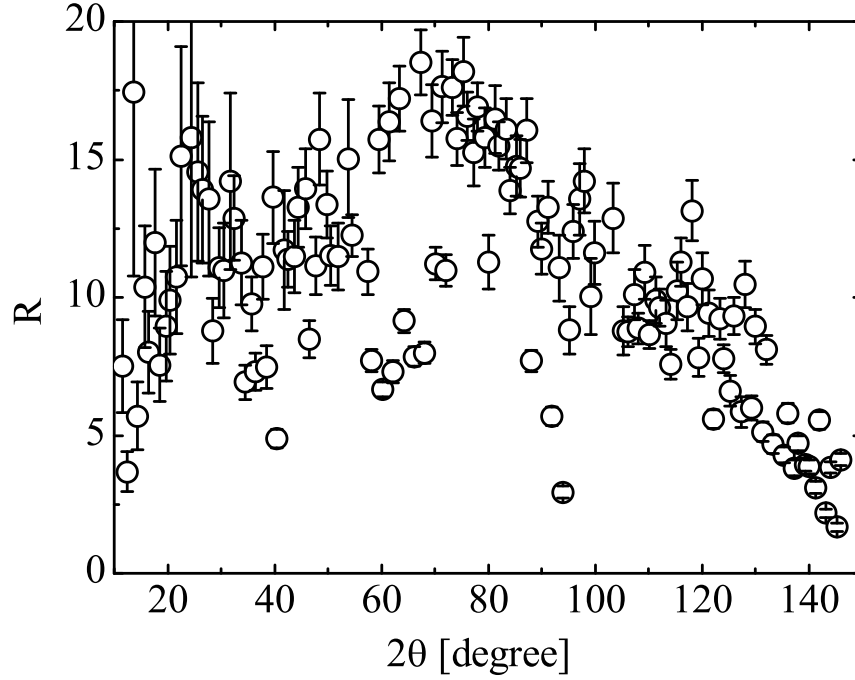


Figure 3.5. Flipping ratio R as a function of the scattering angle 2θ

After this the flipping ratio correction of the registered intensities can be performed as follows [93]:

$$I_{corr}^{\uparrow\uparrow} = I^{\uparrow\uparrow} + \frac{1}{R-1} [I^{\uparrow\uparrow} - I^{\uparrow\downarrow}] \quad (3.2a)$$

$$I_{corr}^{\uparrow\downarrow} = I^{\uparrow\downarrow} - \frac{1}{R-1} [I^{\uparrow\uparrow} - I^{\uparrow\downarrow}] \quad (3.2b)$$

and the final expressions for the coherent and spin-incoherent scattering read:

$$I_{coh} = I_{corr}^{\uparrow\uparrow} - \frac{1}{2} I_{corr}^{\uparrow\downarrow} \quad (3.3a)$$

$$I_{inc} = \frac{3}{2} I_{corr}^{\uparrow\downarrow} \quad (3.3b)$$

3.2.3 Neutron backscattering

Backscattering techniques, applied for a wide variety of problems, provide a very good energy resolution, typically $\Delta E \leq 1\mu eV$, that corresponds to the time-scale of nanoseconds.

To study dynamical processes in the ILs at low temperatures both elastic scan measurements on heating and cooling and QENS-experiments at several temperatures were carried

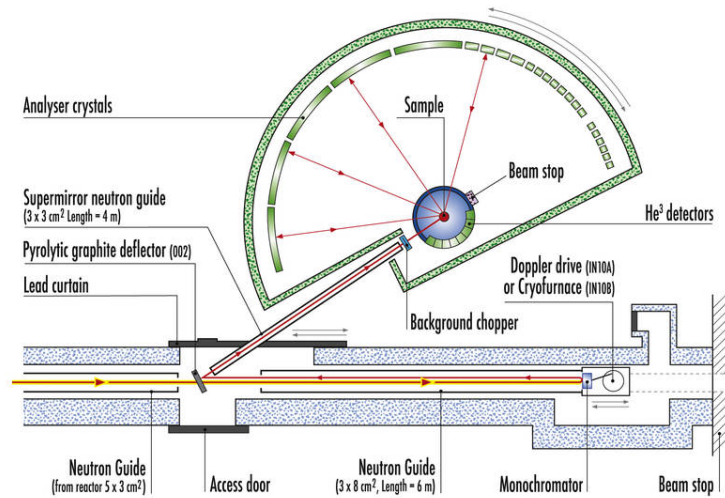


Figure 3.6. IN10 instrument layout

out on the IN10 backscattering spectrometer at ILL [147]. Figure 3.6 presents the instrument layout. By choosing a suitable combination of monochromator and analyser crystals (Si(111)) the wavelength of incident neutrons of $\lambda = 6.3 \text{ \AA}$ was achieved. The energy resolution FWHM equalled $0.8 \mu\text{eV}$ (time window for the elastic line $\sim 1 \text{ ns}$). Seven detectors, covering the Q -range $0.5\text{--}2.0 \text{ \AA}^{-1}$, provided a moderate momentum transfer resolution (the corresponding length window $\sim 1\text{--}10 \text{ \AA}$).

In the QENS mode the energy transfers were scanned by varying the incident energy by Doppler shifting with the frequency of 10.10 Hz. The efficiency of the detectors was calibrated by measuring a vanadium sample. For the background subtraction empty can runs were performed. Taking into account that the QENS signal is very weak and broad relative to the dynamic range of the instrument, the resolution function was determined using the protonated sample at low temperatures where all dynamics are “frozen”. Numerical convolution of a model function with the resolution was employed for a fitting procedure.

In the elastic scan mode the temperature range of 2–320 K was covered. In the interest of time an empty can measurement was carried out only at several temperatures; afterwards the background contribution was estimated by interpolation using the temperature dependence of the Debye-Waller factor for aluminium [148]; then the standard procedure for analysis of elastic scans was applied [149].

The elastic intensity is proportional to the experimentally measured intensity in the channel at $E = 0$, i.e. the elastic peak is integrated over the whole energy transfer range with the resolution function $R(E)$. As the resolution function falls to zero at higher E , for the sake of simplicity the limited dynamical range of the instrument can be extended to an infinite one:

$$\tilde{S}(Q, E = 0) = \int_{-\infty}^{\infty} R(E')S(Q, -E')dE' \quad (3.4)$$

Next, as a first step of data evaluation, an intensity normalisation to the intensity measured at a low temperature was performed, where no significant motion is present. Assuming that for $T \approx 0$ K $S(Q, E) = I_0(Q)\delta(E)$, the normalized elastic intensity reads:

$$I_{\text{el}}(Q) = \frac{\int_{-\infty}^{\infty} R(E')S(Q, -E')dE'}{I_0(Q)R(E = 0)} \quad (3.5)$$

This procedure should be carefully carried out, allowing for a coherent contribution, which may cause, especially at low temperatures, a sufficiently large contribution, where the static structure factor has its maxima. The normalization may cancel this contribution only in the case of negligible thermal expansion.

To simplify fitting of elastic scans the experimentally measured resolution function in Eq. 3.5 can be substituted by either a Gaussian or a Lorentzian curve [150]. To some extent a Gaussian curve might be preferred [114, 149] and it fits the resolution function of IN10 slightly better than a Lorentzian curve does. But it was decided in favour of Lorentzian with $\text{HWHM}=\Gamma_{\text{res}}$ because of its mathematical simplicity regarding convolution process. Under the condition that the harmonic approximation may be used for the Debye-Waller factor and in the case of one of the simplest incoherent scattering laws, given by:

$$S(Q, E) = \text{EISF}(Q)\delta(E) + [1 - \text{EISF}(Q)]L(E, \Gamma) \quad (3.6)$$

where $L(E, \Gamma)$ is a Lorentzian curve with the linewidth Γ , the dependence of the elastic intensity on temperature reads [151]:

$$\ln(I_{\text{el}}) = -\frac{CT}{3}Q^2 + \ln \left\{ \frac{\text{EISF}(Q)}{\pi\Gamma_{\text{res}}} + \frac{[1 - \text{EISF}(Q)]}{\pi(\Gamma + \Gamma_{\text{res}})} \right\} \quad (3.7)$$

where C is the temperature coefficient of the mean squared displacement ($\langle u^2 \rangle = CT$).

4. Data reduction and analysis

4.1. Raw data reduction

QENS method permits almost the direct determination of the scattering function $S(E, Q)$, which is also commonly referred to as the dynamical structure factor (except the neutron spin echo technique, which measures the intermediate scattering function $I(Q, t)$ [152, 153]). Time-of-flight (TOF) spectrometers employed for this work (FOCUS at SINQ, Switzerland [141]; D7 [146], IN5 [144] and IN10 [147] at ILL, France) provide spectra, which are 2D-data sets, where intensity counts depend on the time, when a neutron is registered at a detector, and the angle of this detector ($S(t, 2\theta)$). For further analysis, data reduction is required, which computes the dynamic structure factor $S(E, Q)$. This quantity is independent of the instrument parameters such as chopper speed, the number of time channels and their width, detector angles, or the length of the flight paths. Data reduction normally comprises several steps:

- elimination of bad detectors;
- TOF correction (wavelength calibration);
- conversion from time to energy domain;
- self-shielding correction and background subtraction;
- detector efficiency correction, vanadium normalization;
- energy (E) and wavevector (Q) transfer binning;
- normalization to the monitor value.

A time-of-flight raw data file from FOCUS, for example, contains the information about the speed of the Fermi and disk choppers, the distances from the Fermi chopper to the sample l_{FCtoS} , from the sample to the detectors l_{StoD} and so on, the monitor rate counts I_{mon} and the 2D-array of the rate counts of all the detectors $I_{\text{d}}[i, j]$, the vectors of their polar angles $2\theta[j]$ and of the time channels $t[i]$. The wavelength λ_0 of incident neutrons can be used as given in the data file or can be calculated from sample runs at the step of

wavelength calibration. Let $t_0 = l_{\text{FCtoS}}\lambda_0 m_n / (2\pi\hbar)$ be the time, when the neutrons reach the sample, then $t_f[i] = t[i] - t_0$ is the time, during which a neutron travels from the sample to a detector. Their velocities and wavevectors after the scattering event can be calculated as $v_f[i] = l_{\text{StoD}}/t_f[i]$ and $k_f[i] = m_n l_{\text{StoD}} / \hbar t_f[i]$, respectively. The measured counts at the j -th detector within one time channel $\Delta t[i] = t_f[i+1] - t_f[i]$ are proportional to the incoming neutron flux Φ , the double differential cross section of the sample, the solid angle $\Delta\Omega[j]$, subtended by the detector, the efficiency of the detector η and the corresponding energy interval $\Delta E[i] = E_f[i+1] - E_f[i]$:

$$I_d[i, j] \Delta t[i] = \frac{d^2\sigma}{d\Omega dE} \eta \Phi \Delta\Omega[j] \Delta E[i] \quad (4.1)$$

The time and energy intervals are related to each other as:

$$\Delta E[i] = \frac{m_n}{2} (v^2[i+1] - v^2[i]) = \frac{m_n l_{\text{StoD}}^2}{2} \left(\frac{1}{t_f^2[i+1]} - \frac{1}{t_f^2[i]} \right) \approx -m_n l_{\text{StoD}}^2 \frac{\Delta t[i]}{t_f^3[i]} \quad (4.2)$$

Taking into account Eq. 2.6, the final formula for the experimentally determined scattering law reads:

$$\frac{\sigma_{\text{inc}}}{4\pi} S_{\text{inc}}(2\theta, E) + \frac{\sigma_{\text{coh}}}{4\pi} S_{\text{coh}}(2\theta, E) = \frac{2\pi\hbar t_f^4[i]}{N\eta\Phi\Delta\Omega[j]m_n^2 l_{\text{StoD}}^3 \lambda_0} I_d[i, j] \quad (4.3)$$

The detector efficiency can be corrected by normalizing the data with the integrated intensity of a vanadium sample with identical to the sample container scattering geometry, because vanadium is a dominant incoherent scatterer. As the incoming neutron flux Φ may vary in time, the count rate at the detectors should be also normalized to the rate counts of the control monitor I_{mon} , mounted in front of the sample.

Background subtraction is not straightforward; simple subtraction of the empty can runs from the sample runs would produce an error. A proper treatment of the shielding effect due to absorption and scattering should be undertaken [154]. For the annual geometry with a hollow cylinder the intensity at the scattering angle 2θ can be written as a sum over four regions (Fig. 4.1):

$$I(2\theta) = \sum_{k=1}^4 I_k(2\theta), \quad I_k(2\theta) = \Phi V_k \mu_k(2\theta) f_k^m(2\theta) \Delta\Omega / 4\pi \quad (4.4)$$

where V_k is the illuminated volume of region k and μ_k is the macroscopic differential cross section for the scattering from region k into the detector at the scattering angle 2θ . The self-shielding factors (SSFs), denoted as $f_k^m(2\theta)$, depend not only on the scattering angle and the region, but on the type of the measurement (sample or empty can runs). The sample

container used in this work was made of aluminium (region 2 and 4); region 1 was normally evacuated; and finally region 3 was filled with an IL.

For the empty can (EC) measurement there are contributions from regions 2 and 4:

$$I^{\text{EC}} = \Phi(\Delta\Omega/4\pi)\mu_{\text{Al}}(2\theta) [V_2 f_2^{\text{EC}}(2\theta) + V_4 f_4^{\text{EC}}(2\theta)] \quad (4.5)$$

whereas for the full can (FI) measurement there are contributions from regions 2,3, and 4:

$$I^{\text{FI}} = \Phi(\Delta\Omega/4\pi) \{ \mu_{\text{Al}}(2\theta) [V_2 f_2^{\text{FI}}(2\theta) + V_4 f_4^{\text{FI}}(2\theta)] + \mu_{\text{sam}}(2\theta) V_3 f_3^{\text{FI}}(2\theta) \} \quad (4.6)$$

After some algebraic manipulation the macroscopic differential cross section of the sample can be written in the following form:

$$\mu_{\text{sam}}(2\theta) = \frac{1}{\Phi(\Delta\Omega/4\pi)V_3 f_3^{\text{FI}}(2\theta)} [I^{\text{FI}}(2\theta) - I^{\text{EC}}(2\theta)g(2\theta)] \quad (4.7)$$

where

$$g(2\theta) = \frac{V_2 f_2^{\text{FI}} + V_4 f_4^{\text{FI}}}{V_2 f_2^{\text{EC}} + V_4 f_4^{\text{EC}}} \quad (4.8)$$

Sometimes the latter factor is called the sample attenuation factor (SAF). In order to calculate it within a constant, SSFs are needed in addition to the volumes and the measured intensities of the two runs (FI and EC). Software for neutron scattering data reduction usually provides means for numerical calculation of SSFs for different experimental geometries.

The software package DAVE (the **D**ata **A**nalysis and **V**isualization **E**nvironment) [155] was used for the reduction of FOCUS spectra; data acquired on the ILL and FRM II instruments were accordingly treated in LAMP (**L**arge **A**rray **M**anipulation **P**rogram) [156].

4.2. 2D-fitting routine

After data are transformed into the (Q, E) -space, spectra can be analysed via fitting the scattering function by model functions convoluted with the resolution function of an instrument. Model functions usually depend both on energy- (E) and wavevector- (Q) transfer of neutrons and the fitting procedure is performed for a selected Q -group. Thus Q is handled as a fixed parameter. After all Q -groups are fitted, a user gets Q -dependences of different parameters such as, for example, linewidth, intensity, radius of confinement, relaxation time, which can be further analysed. Such an approach is used in the DAVE package in the frame of the general-purpose curve-fitting application called PAN (for **P**eaK **A**nalysis). It is a very convenient tool, which provides means for factoring the instrumental

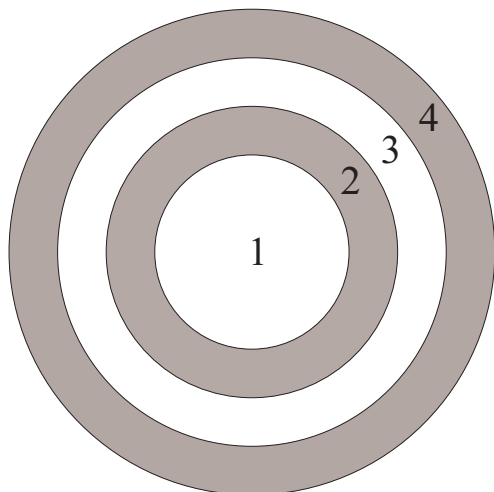


Figure 4.1. Hollow cylinder (top view); regions 2 and 4 represent the material, the container is made of, while region 3 is to be filled with the liquid

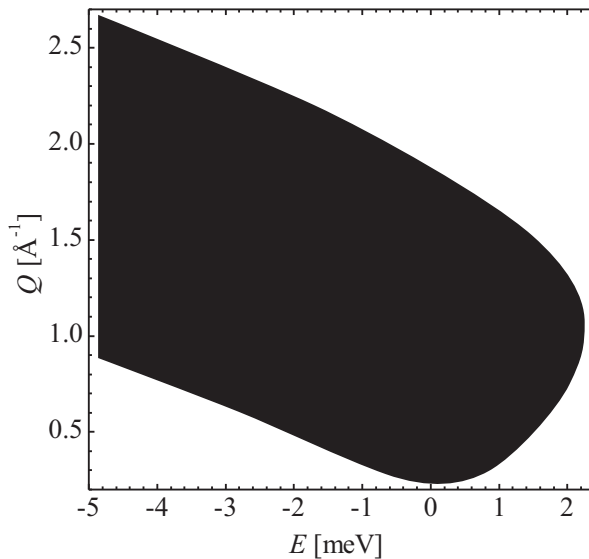


Figure 4.2. (E, Q) -space, available for probing with the wavelength of incident neutrons of $\lambda=5.75 \text{ \AA}$

resolution function into the data analysis, contains a library of pre-defined functions and has an option to define simple user-functions and save it for later use. But if a studied system cannot be described by a simple model with a small number of adjustable parameters, the fitting routine becomes unstable, because several local minima may exist. This can already be the case for a two-component scattering function (an elastic line and one Lorentzian, or two Lorentzians), to say nothing of more than two components. According to experience it is usually impossible to obtain compatible stable fit results for all Q-groups at the same time [73]. The way out is to use an advanced two-dimensional surface fit, when both energy transfer and wavevector transfer are considered to be independent variables, or even a three-dimensional fit with the temperature as an additional variable [157, 158]. An advantage of this approach is also less stringent requirements on the statistical quality of spectra. The RAINS module (for **R**efinement **A**pplication for **I**nelastic **N**eutron **S**cattering) within the DAVE-package was elaborated for this kind of tasks. However, its functionality and the number of model functions included are limited.

Therefore the program code for the 2D-fitting program module (Fig. 4.3) has been written by means of the IDL programming language on the bases of the `mpcurvefit` procedure (non-linear least squares curve fitting) [159, 160], which was used as given. The core of the procedure is the Levenberg–Marquardt algorithm (the damped least-squares method) [161], which allows surface fitting. The same procedure is used both in PAN and RAINS and shows

good efficiency and convergence within reasonable computational time.

The main structure of the program module, which is initialized on starting it, is shown below:

```
state = {resPtr:ptr_new(/allocate_heap), $
        funPtr:ptr_new(/allocate_heap), $
        maskPtr:ptr_new(/allocate_heap), $
        errorPtr:ptr_new(/allocate_heap), $
        xvalsFunPtr:ptr_new(/allocate_heap), $
        xvalsResPtr:ptr_new(/allocate_heap), $
        xvalsFitPtr:ptr_new(/allocate_heap), $
        QvalsPtr:ptr_new(/allocate_heap), $
        fitPtr: ptr_new(/allocate_heap), $
        ParamPtr: ptr_new(/allocate_heap), $
        ParamNamesPtr: ptr_new(/allocate_heap), $
        fitfunc: '', $
        xRegion: [-1.0,1.0], $
        Qregion: IntArr(2), $
        thisPath:'', $
        indexWin:0, $
        indexErr:0, $
        fixedParmList: ''}
```

The structure contains the pointers to the 2D-arrays of the spectrum (`funPtr`), of the resolution function (`resPtr`), and of the convolution of the fit model and the resolution function (`fitPtr`). As the arrays of energy transfer may be different in all cases (different energy binning for the resolution function and the spectrum, or E -bins are not equally spaced), the corresponding pointers `xvalsFunPtr`, `xvalsResPtr`, `xvalsFitPtr` have been included as well. The user can define energy-window for fitting, in other words, arbitrary cut the spectrum at those E -values, where the intensity is very low and the signal is very noisy. This user setting is stored in the structure field `xRegion`. The array of one more independent variable (wavevector transfer) is pointed by `QvalsPtr`. The user can decrease the number of Q -groups as well by changing the field `Qregion`. `errorPtr` pointers to the array of signal errors. The 2D-fitting program module reads spectra saved in *.dave format [162, 163], which is automatically created if the data reduction have been performed in DAVE. In other cases conversion must be carried out.

The field `maskPtr` warrants further attention. In comparison to RAINS, which allows working only with a rectangular region of (E, Q) - space where all histogram points are defined, the proposed code can fit spectra for the region limited by a user on one side (via

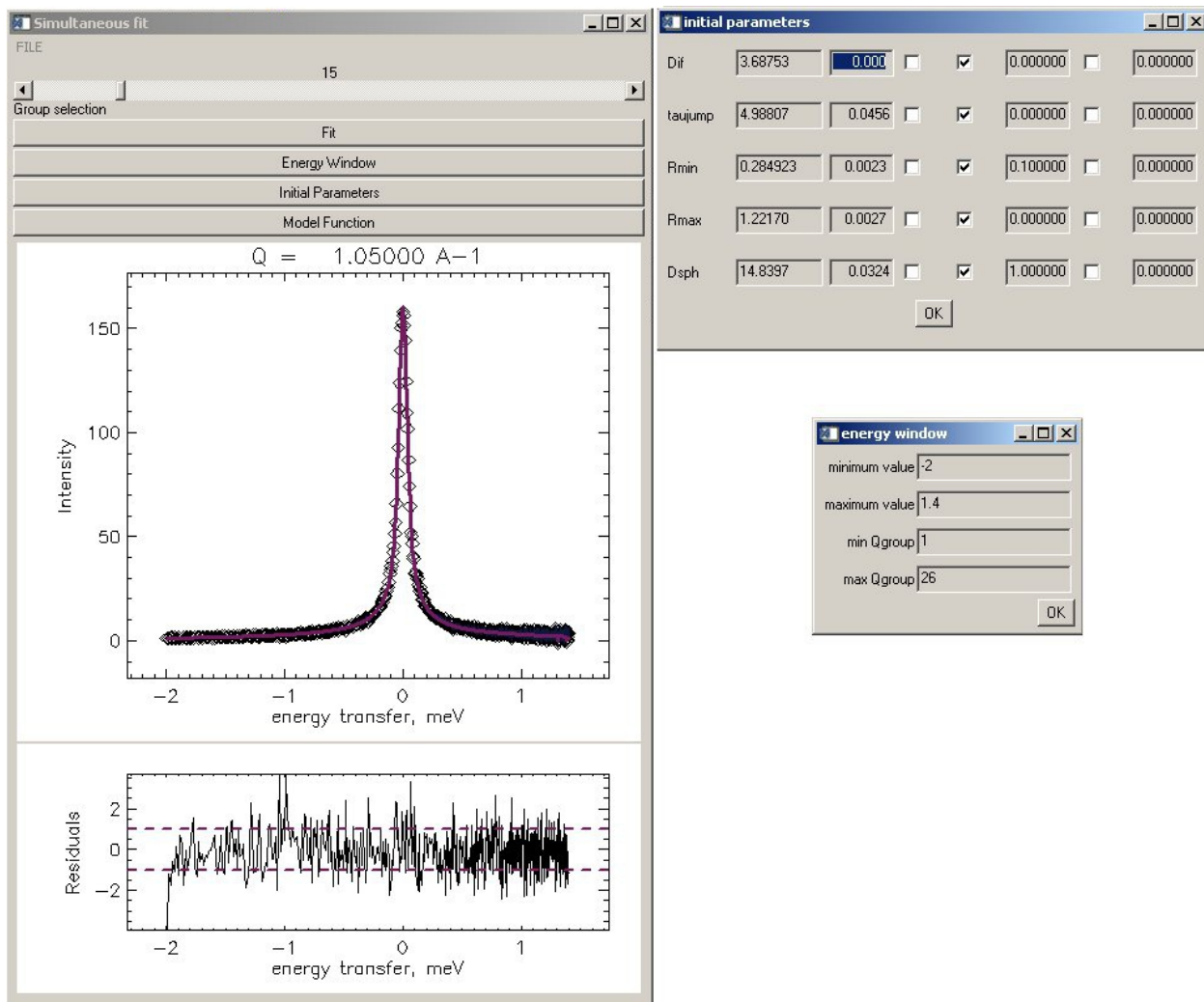


Figure 4.3. A screenshot of the 2D-fitting program module

xRegion) and the conservation laws on the other side (Fig. 4.2) at the same time. This allows to increase the energy window for high Q -values, where a QENS-spectrum is usually much broader and larger energy transfer values are required for an unambiguous analysis. The program module finds those points, which belong to the rectangular region defined by the user, but with the error value being equal to -1 (undefined). This information is stored in the array `mask` and undefined points are not taken into account, while calculating χ^2 in the fitting routine.

The model functions were written as separate IDL-procedures, so that new ones can be easily added on request. Functions can include build-in functions as Bessel functions or they can be defined as series or integrals of other standard functions. The name of the corresponding procedure is stored in the field `fitfunc`. `ParamPtr` and `ParamNamesPtr` are the pointers to the arrays with the adjustable parameters and their names respectively. All parameters can be divided in two groups. The first group (`single_parmnames`) does not

depend on Q -values and is usually explicitly defined in a theoretical model of the scattering law, for example, diffusion coefficients, radii of confinement, relaxation times. The second group (`multi_parmnames`) contains parameters, which are different for every Q -group and might not even have any meaningful dependence on Q , as for example, center of the line or misalignment parameter; flat background, which contains a part of the temperature dependent phonon density of states; intensity. If to consider all multiparameters as adjustable in the fitting routine, it can unpredictably increase computation time or lead to malfunction. Therefore, some of them can be calculated by fitting every Q -group separately in PAN, saved as a csv-file and transferred to the 2D-fitting program module. This approach is implemented via the reference to the csv-file in the field `fixedParmList`. The syntax of model functions is shown below:

```
pro function_name, xvals, parms, yout,$
    parmnames = parmnames, $
    single_parmnames = single_parmnames, $
    multi_parmnames = multi_parmnames, $
    _Extra = extra ;
```

As `mpcurvefit` accepts only 1D-vectors as independent variables, it is necessary to concatenate E - and Q - vectors in `xvals` and pass to the model function and the fitting procedure. The reverse extraction of the independent vectors is performed in the body of every model function. The necessary information for this step is passed via `_Extra` functionality. `_Extra` is a structure with several fields: number of E - and Q - bins, the pointer to the instrument resolution function (The Levenberg-Marquardt algorithm requires numerous evaluations of the fit function, so passing the array would slow down the performance), the array `mask` and the array of externally determined fixed parameters as line centres or intensities. `parms` is a 1D-array with adjustable parameters, `yout` is the 2D-result of the whole procedure, or the convolution of the model function with the instrument resolution function. The procedure `mpcurvefit` implies weighted fit, when one gives less weight to the less precise measurements and more weight to more precise measurements. The weights are calculated from the experimental histogram errors as $weight = 1/error^2$. The uncertainties in the adjustable parameters returned by `mpcurvefit` are based on the curvature of the χ^2 surface [162].

For handling adjustable parameters a user can call the window “initial parameters”, where he can set an initial guess for any parameter, lower or/and upper limits of its value or fix the parameter (Fig. 4.3). The procedure for saving and restoring adjustable parameters is implemented as well (`SaveFitPar`, `RestFitPar`). A part of the graphical user-interface are the procedures (`drawcurves`, `SelectGroup`), which allow a user to select a Q -group and to

see the results of the fitting (a spectrum and residuals) in the plot window. Thus the user can estimate the quality of the fit and the applicability of the chosen model function.

The validity of the 2D-fitting program module was tested on the generated QENS-data with the predefined model.

5. Cation dynamics in pyridinium-based ILs

This chapter contains the results of the QENS-studies on the pyridinium based ILs [BuPy][Tf₂N] and [C₁₂Py][Tf₂N]. As introduced in Chapter 3 these compounds belong to the class of ILs with important properties for potential electrochemical applications. Besides, the demand for the physical-chemical data on these ILs is likely to increase on account of their better biodegradability.

The goal of the study was twofold. First, fundamental understanding of the influence of the alkyl chain on microscopic dynamics is essential for designing molten salts. Many groups of ILs have alkyl side groups, which allow to change their physicochemical properties (viscosity, diffusivity, density, conductivity, phase transition temperatures). This way, the self diffusion coefficients of both the cations and the anions decrease with increase in the number of carbon atoms in the alkyl chain of imidazolium-based ILs [60, 66]. The diffusion of ions is governed by electrostatic forces, as well as by inductive forces. The latter are affected by at least two factors: the size of the ion and its shape [164]. With increase in the alkyl chain length, the role of the inductive interaction becomes much more influential, resulting in higher viscosity values. Frictional forces between aggregates and clusters and steric hindrance may additionally come into interplay. On the other hand, Tsuzuki et al. [165] showed that conformational flexibility and internal rotations of alkyl side chains enhance the microscopic dynamics. The authors also emphasized that the planar shape of aromatic cations is usually more favourable for diffusivity in comparison with some other more bulky ions [53].

Second, in order to unravel complex motions overlapping on the nano- and picosecond time scale, it was decided to derive benefit from deuterium labelling. With respect to the internal dynamics of a pyridinium-based cation, one may expect to observe contributions from the alkyl chain (torsional rotations, libration of the whole chain, methyl group rotations) and from the pyridinium ring (out-of-plane libration and rotation). Thus, two partially deuterated samples of [BuPy][Tf₂N] were investigated: either the chain of the cation [Bu_DPy][Tf₂N] or the ring [BuPy_D][Tf₂N] were deuterated. To the best of our knowledge this approach has

not been widely used for ILs so far. Hence it may shed more light on the heterogeneous dynamics of ILs.

5.1. Low-temperature dynamics in [BuPy][Tf₂N]

To disclose the nature of the low-temperature processes both elastic scan measurements and QENS-experiments on three samples (totally protonated [BuPy][Tf₂N], and partially deuterated [Bu_DPy][Tf₂N] and [BuPy_D][Tf₂N]) were performed on IN10. Figure 5.1 presents the results of the elastic scan measurements carried out upon cooling and heating at the rate of 0.25–0.50 K/min (lower scan rates were used for the partially deuterated samples). The temperature range covered in the experiments was 2–320 K.

The abrupt decrease at $T = 300$ K and increase around 275 K of the elastic intensity for both samples are evidently connected with the solid-liquid phase transitions, which are also observable in DSC-curves as a melting and crystallization peak (Fig. 3.1). The position of the latter strongly depends on the cooling rate. In Figure 5.2 the low temperature range of the elastic scans at $Q = 1.85 \text{ \AA}^{-1}$ is displayed. This Q -value was chosen for analysis and fitting to minimize unwanted coherent scattering, which is substantial around structural maxima at low temperatures observed for the other detectors. The elastic scattering intensity from the pyridinium ring falls gradually with temperature increase. For the sample with the protonated chain the dependence changes its inclination twice (at 100 K and 160 K). This is an indication that a dynamical process is activated and energy exchange occurs between the sample and the incident neutrons. The gradual drop of the elastic intensity resembles analogous dependences of other compounds with methyl groups, which rotation is considered to be thermally activated [112–114, 166]. The dynamic scattering law can be described by the three-fold jump rotation model or by the rotational diffusion model (see 2.3.3–2.3.4). Both models are characterized by a relaxation time, which follows an Arrhenius temperature dependence, $\tau = \tau_0 \exp(E_a/RT)$, where E_a is the activation energy of the corresponding processes. The value of the latter parameter can be estimated from the temperature variations of the elastic intensity [151]. In the two limiting cases ($\hbar/\tau \ll \Gamma_{\text{res}}$ and $\hbar/\tau \gg \Gamma_{\text{res}}$) two straight almost parallel lines will be observed, whereas in the temperature range, where $\hbar/\tau \sim \Gamma_{\text{res}}$, the logarithm of the elastic intensity will fall faster with temperature increase. Assuming either the three-fold jump rotation model (Eq. 2.26) or the rotational diffusion model (Eq. 2.28) and taking into account Eq. 3.6–3.7, the temperature dependency of elastic intensity scans reads:

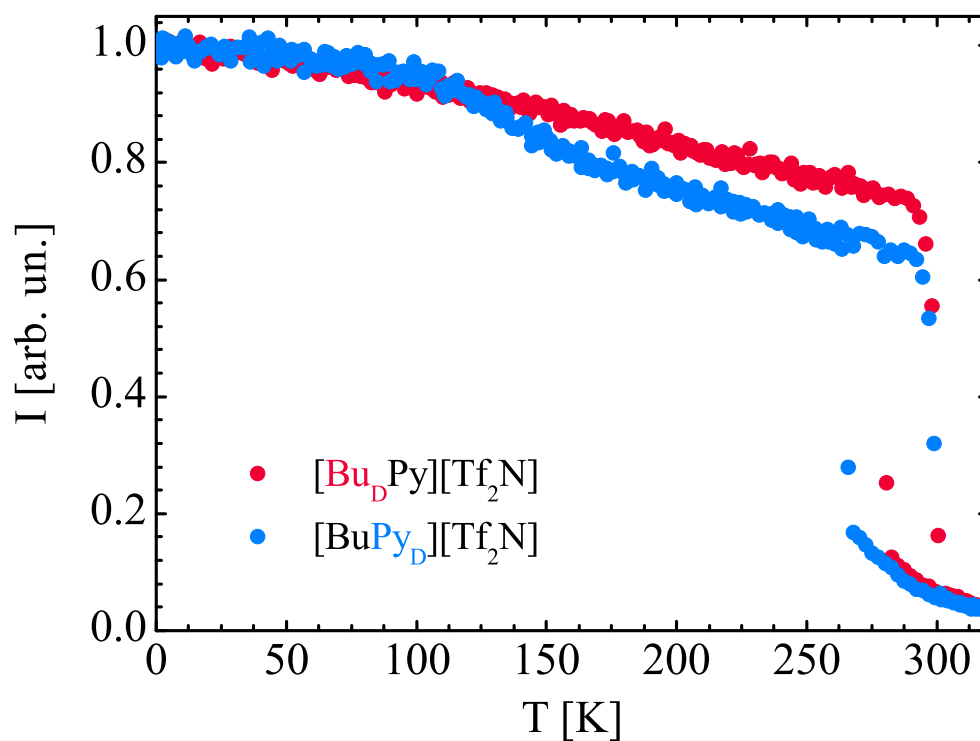


Figure 5.1. Elastic scan measurements on the partially deuterated pyridinium-based ionic liquids

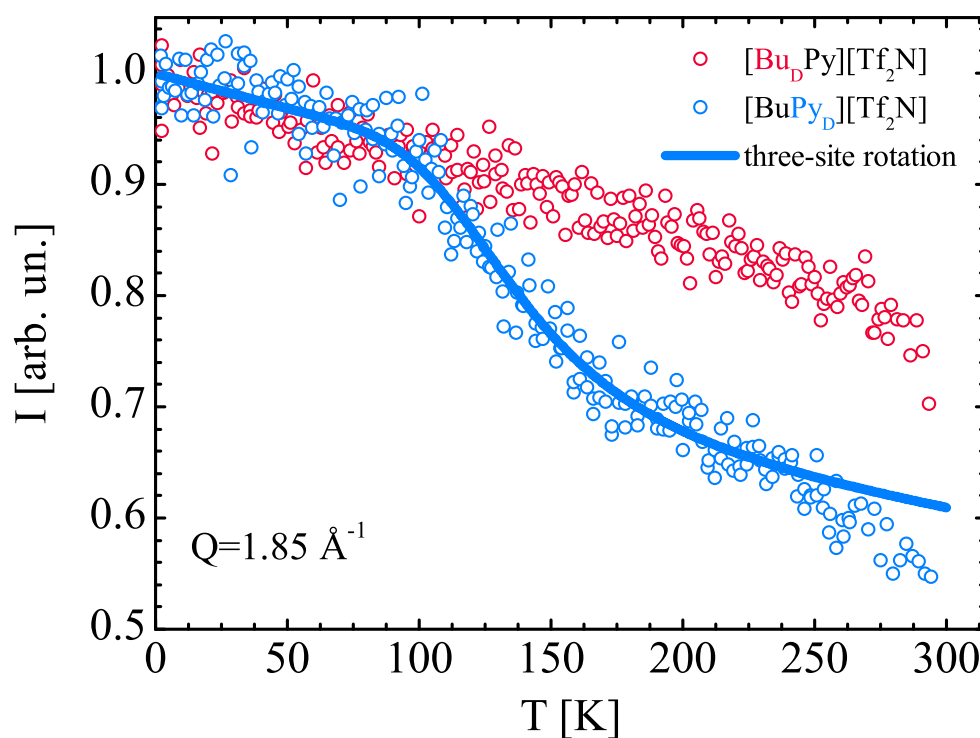


Figure 5.2. Elastic scan data for the partially deuterated samples at $Q = 1.85 \text{ \AA}^{-1}$. A solid blue line represents the result of the fit using Eq. 5.1

Table 5.1. Fit results of the elastic intensity scans according to Eq. 5.1 and 5.2

	three-fold jump rotation	rotational diffusion
τ_0 , ps	9.0 ± 1.6	2.0 ± 0.4
E_a , kJ/mol	6.5 ± 0.5	7.0 ± 0.6
R , Å	1.10 ± 0.03	1.12 ± 0.04
p_{mob}	0.37 ± 0.02	0.33 ± 0.02

$$\ln I_{\text{el}}(T, Q) = A - \frac{CT}{3}Q^2 + \ln \left[1 - p_{\text{mob}} + p_{\text{mob}} \times \left\{ \frac{1}{3} \left(1 + 2j_0(QR\sqrt{3}) \right) + \frac{2}{3} \left(1 - j_0(QR\sqrt{3}) \right) \frac{\Gamma_{\text{res}}}{\Gamma_{\text{res}} + 3\hbar/(2\tau)} \right\} \right] \quad (5.1)$$

$$\ln I_{\text{el}}(T, Q) = A - \frac{CT}{3}Q^2 + \ln \left[1 - p_{\text{mob}} + p_{\text{mob}} \times \left\{ j_0^2(QR) + \sum_{k=1}^{\infty} \frac{(2k+1)j_k^2(QR)\Gamma_{\text{res}}}{\Gamma_{\text{res}} + \frac{k(k+1)\hbar}{6\tau}} \right\} \right] \quad (5.2)$$

where Γ_{res} is the half width of the resolution function, p_{mob} is the fraction of hydrogen atoms involved in the methyl group rotation. Our data are compatible with both models, yielding the parameter values presented in Table 5.1. The fraction of mobile hydrogen atoms is around 1/3. This number corresponds to the three protons at the end of the alkyl chain, whereas the total number of protons in the butyl chain is nine. The radius of the sphere is 1.1 Å, which is in agreement with the characteristic length of the C-H bond in the methyl group [167, p. 151].

The geometry of the localized dynamics at low temperatures was also considered by analyzing QENS-spectra. Unfortunately, the available energy-window ($[-12.5; 12.5]$ μeV) did not allow to obtain reliable information about the timescale of the localized motion of the alkyl chain and the pyridinium ring, as the observed QENS-broadening was either comparable with the energy-window or much wider and had a visible contribution only for high Q -values, resulting in relatively high EISF-values (0.7–1.0). This can be explained by the assumption that a certain part of hydrogen atoms is immobile in the given temperature range and, hence, contributes to the elastic signal. We applied the rotational diffusion model to analyze QENS-data for the two partially deuterated samples. The results of the fits are listed in Table 5.2. At $T = 290$ K the localized motion of the pyridinium ring can be envisaged as a diffusion on a sphere with a radius $R = 1.5$ Å and a relaxation time $\tau = 12$ ps. The portion of mobile atoms amounts to 0.20. The QENS-broadening of $[\text{Bu}_D\text{Py}][\text{Tf}_2\text{N}]$ might be connected with out-of-plane librations of the ring and the dynamics are essentially “frozen”

Table 5.2. Fit results of the QENS-spectra according to the rotational diffusion model

	τ , ps	R , Å	p_{mob}
$T=290$ K			
[Bu _D Py][Tf ₂ N]	12	1.5	0.20
[BuPy _D][Tf ₂ N]	20	1.0	0.35
$T=250$ K			
[Bu _D Py][Tf ₂ N]	16	1.5	0.15
[BuPy _D][Tf ₂ N]	~20	1.0	0.32
$T=175$ K			
[Bu _D Py][Tf ₂ N]	~20	1.5	0.07
[BuPy _D][Tf ₂ N]	≫20	1.0	0.30
$T=130$ K			
[Bu _D Py][Tf ₂ N]	–	–	~0
[BuPy _D][Tf ₂ N]	≫20	1.0	0.26

at the lower temperatures, as p_{mob} does not reach high values. It is anyway clear that the observed broadening is not a trace of a weak incoherent contribution from the deuterated butyl chain. Otherwise the elastic scans of the two samples would look similar; the difference would become apparent only in the size of a step connected with the thermally activated methyl-group rotation process. With the temperature decrease p_{mob} drops almost to zero, while the relaxation time of the pyridinium ring libration increases. As for the sample with the protonated butyl chain, the obtained values for the radius of confinement and the fraction of mobile atoms are in agreement with the values evaluated from the elastic intensity scans ($R = 1.0$ Å, $p_{mob} \approx 0.3$). So we may conclude that we observe the dynamics of the end methyl-group of the alkyl chain.

From the Q -dependence of elastic temperature scans the mean squared displacement (MSD) for single-particle motions can be calculated in Gaussian approximation.

$$\langle u^2(T) \rangle = -3Q^{-2} \ln [I_{el}(Q, T)/I_{el}(Q, T \rightarrow 0)] \quad (5.3)$$

Here $\langle u^2(T) \rangle$ stands for a full amplitude of a variety of hydrogen motions localized inside the instrumental length- and time-window. This empirical approach is widely applied to study molecular flexibility and resilience of proteins [168–171]. However, it is important to remember that the Gaussian approximation is valid only for small Q -values ($\langle u^2(T) \rangle Q^2 \leq 2$).

The MSD analysis of [BuPy][Tf₂N] at low temperatures was complicated by the presence

of coherent contribution at small Q -values, which are most valuable for this kind of data characterization (a static structure factor can not be cancelled by normalization if sufficient thermal expansion is present and the structural maxima shift to lower Q -values with temperature increase), so only the temperatures, for which the studied ionic liquids are in the liquid state, were considered. Figure 5.3 presents the temperature dependence of MSD for all the three studied samples. On the time-scale of 1 ns the influence not only of faster internal motions but also of global diffusion and rotation are expected to be observable, as it follows from both the theoretically predicted [52, 53, 172] and experimentally proved [173] results. But it is practically impossible to disentangle all these kinds of motions just by analysing MSD dependencies for a limited temperature range. From the comparison of MSD of the partially deuterated samples it is evident that the flexibility of the alkyl chain contributes more to the energy exchange between the sample and neutrons than the ring.

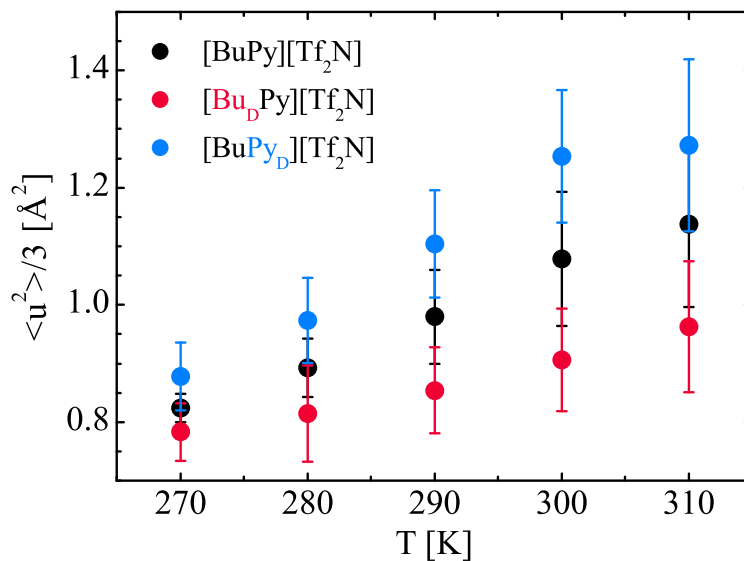


Figure 5.3. Mean squared displacement for the partially deuterated and the totally protonated pyridinium-based ionic liquid

5.2. Model independent analysis of the liquid state

For the temperatures above the melting points (Table 3.3) both the global (translational motion and rotation of the whole cation) and internal dynamics (different internal rotations and librations) of ILs become more diverse. As the first step, model independent fits were applied (see Chapter 2.3), which are, nevertheless, sufficient to reveal some differences between the samples with the butyl ([BuPy]) and dodecyl ([C₁₂Py]) substituents.

The data sets presented and compared in this part are collected on FOCUS ($\lambda = 5.75 \text{ \AA}$). Figure 5.4 demonstrates that the measured quasielastic spectra of both samples can be satisfactorily well described as a superposition of two Lorentzian curves and a linear background (Eq. 2.21); i.e., no elastic contribution is present in all the measured spectra.

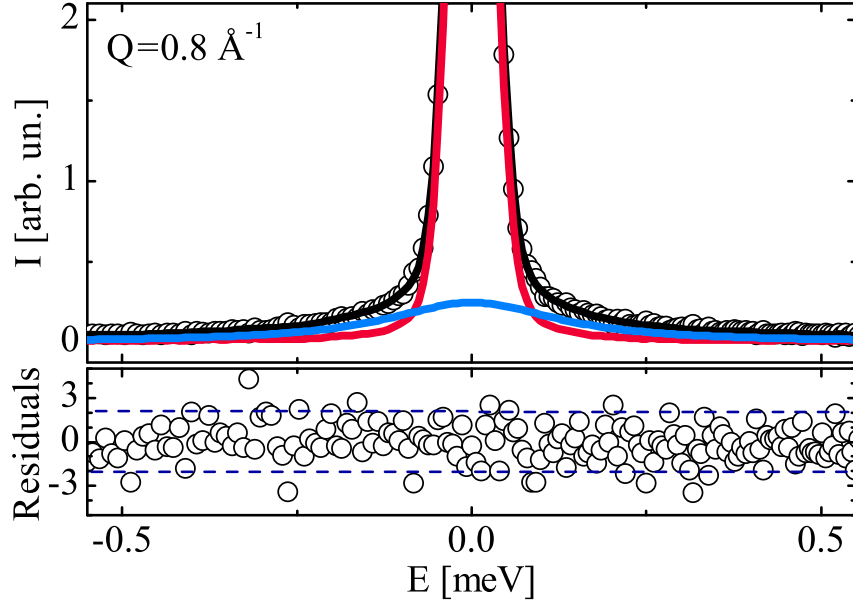


Figure 5.4. QENS spectrum of a completely protonated [BuPy][Tf₂N] sample, measured on FOCUS at $T=300 \text{ K}$ and $Q = 0.8 \text{ \AA}^{-1}$ (symbols) with the fit function (black solid line). The red and blue lines represent Lorentzian functions, which compose the total fit function. In the lower panel the residuals between the fit function and the measured intensities are presented.

The Q - and T -dependence of the parameters in Eq. 2.21 disclose some information about the time-scale and nature of the observed stochastic motions (Fig. 5.5). The narrower Lorentzian contribution $\Gamma_{\text{glob}}(Q)$ tends to 0 at small Q -values (1a–1b) in the same way as for long-range diffusional processes (see 2.3.1–2.3.2). Comparing the two pyridinium-based cations, one can see that unrestricted motion of the heavier [C₁₂Py] cation is slower, in agreement with the tendency for other groups of ILs discussed in the introduction of this chapter. This linewidth $\Gamma_{\text{glob}}(Q)$ is visibly affected by temperature, while the broader Lorentzian contribution $\Gamma_{\text{loc}}(Q)$ (Fig. 5.5; 2a–2b) exhibits a less pronounced temperature dependent character. The latter tends to an almost constant non-zero value at small Q -values, thus, giving an indication of a movement in a confined region. This plateaulike behaviour can be deduced from the “diffusion in a sphere” model or the Gaussian model (see 2.3.5–2.3.6). The higher Q -value region, where a gradual increase in the linewidth occurs, corresponds to shorter lengths, which are less than the size of the confinement, and the restricted diffusion can be treated as long-ranged. So the more rapid increase of the [BuPy]-dependence

for $Q > 0.8 \text{ \AA}^{-1}$ might point to faster localized dynamics than for $[\text{C}_{12}\text{Py}]$. The confinement might be either due to the surrounding ions, which may form a cage-like structure, or due to the restricted geometry of the cation (chain and ring librations, conformational changes in the chain etc.). For more details it is necessary to analyse the EISF-dependences (Fig. 5.5; 3a–3b), which turned out to be almost identical for both samples regardless of their shape and size. This means that cage-like effects and global rotations inside this cage are likely to be out of the scope of the length- and time-scale of the measurements in agreement with the theoretical predictions [52]. Otherwise, the difference in the cation size would be reflected in the EISF-dependencies. It is also typical for both samples that the decrease of EISF becomes steeper with increasing temperature, signaling gradual growth of the confinement size.

It is quite a common approach that, after the preliminary model-independent step has been performed, $\text{EISF}(Q)$ is fitted to Eq. 2.31 or any other explicit expression for EISF of the model chosen. In this way radii of confinement can be evaluated. Nevertheless, in this work it was decided not to follow this procedure for several reasons. First, one broad Lorentzian curve does not really substitute all the summands in the series of the scattering law (Eq. 2.29). For this reason EISF is not computed accurately, especially for larger Q -values, where it becomes more obvious that two Lorentzians are a coarse approximation. For a broader energy transfer window more Lorentzian contributions are needed to describe the spectrum more precisely. Furthermore, the values of the fit parameters noticeably depend on the chosen dynamic range. Second, at small Q -values the ratio of the Lorentzian linewidths related to the two processes is of the order of 50, whereas it reaches the value of 20 for $Q > 1.5 \text{ \AA}^{-1}$. It means that the separation of the underlying localized and global dynamics becomes less unambiguous. A possible solution to improve the reliability of the fitting routine is to choose explicit models for data analysis and to use the 2-D fitting procedure described in Chapter 4. The reasons, why and which analytical models discussed in Chapter 2.3 for both restricted and unrestricted motions should be included in the final expression of the scattering law, will be considered in the following part.

5.3. Dynamic structure factor models for pyridinium-based ILs

In the case of the slower long-range process the jump-diffusion model was chosen (see 2.3.2). It is already applicable to $\Gamma_{\text{glob}}(Q)$ in the frame of the model-independent approach. The dashed lines in Figure 5.5 (1a–1b) illustrate the validity of this assumption. Besides, the

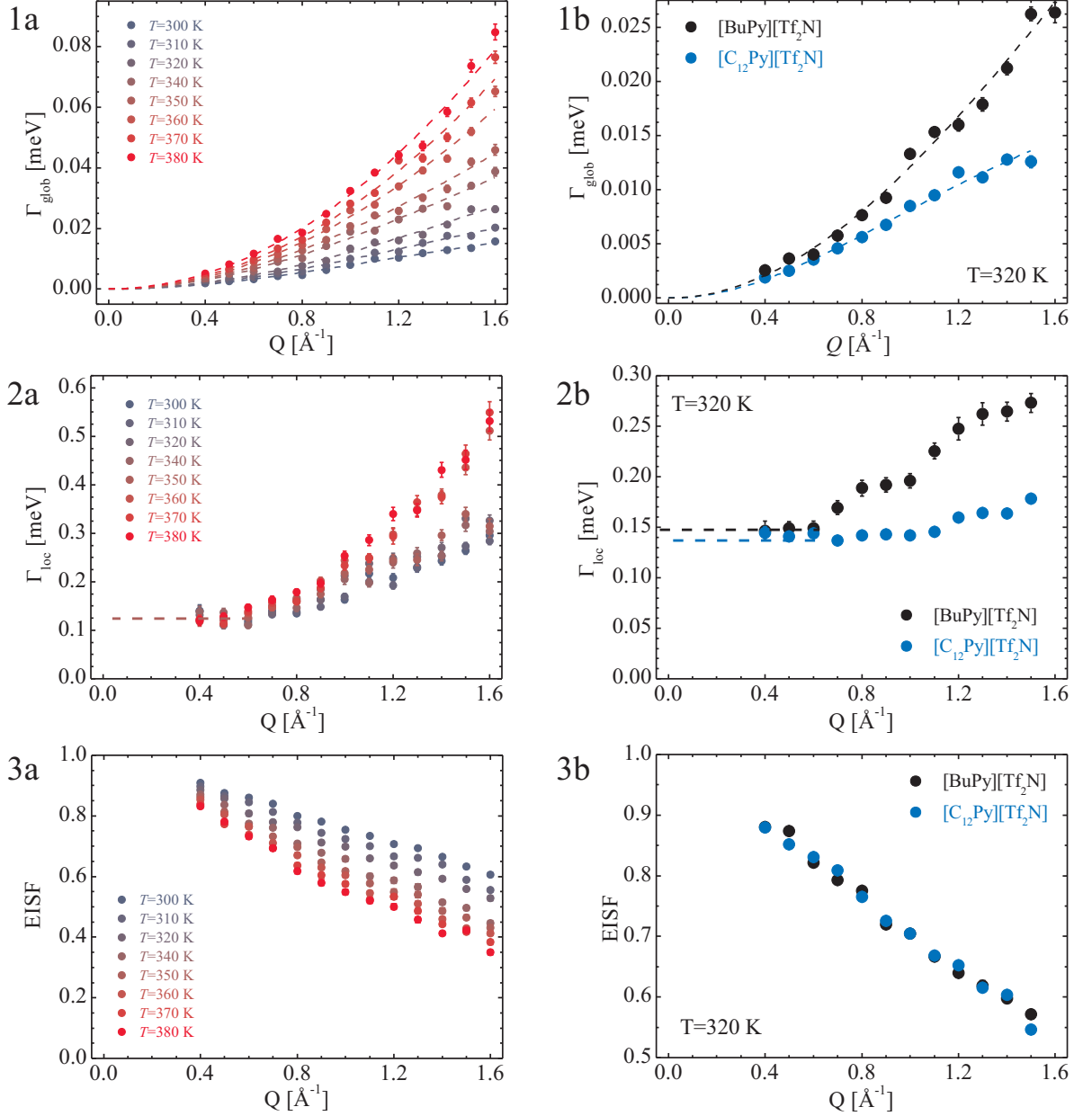


Figure 5.5. *Left:* Model-independent fit parameters for [BuPy][Tf₂N] as a function of wavevector transfer Q at different temperatures: 1 – linewidths of the slower global process (the dashed lines are fits according to Eq. 2.24); 2 – linewidths of the faster localized dynamics and 3 – elastic incoherent structure factor. *Right:* Comparison of the model-independent fit parameters for [BuPy][Tf₂N] and [C₁₂Py][Tf₂N] evaluated at temperature $T=320$ K.

jump-diffusion model was successfully applied to some similar systems [76, 79]. From the fitting procedure of the linewidths $\Gamma_{\text{glob}}(Q)$ to Eq. 2.24 it is possible to extract the diffusion coefficients D and the residence time τ_0 , respectively. Both parameters are plotted as a function of the inverse temperature in Figure 5.6–5.7. The temperature dependence of the self-diffusion coefficient can be modelled by the Arrhenius equation:

$$D(T) = D_0 \exp[-E_a/RT] \quad (5.4)$$

where $R=8.31 \text{ J}/(\text{mol}\cdot\text{K})$ denotes the gas constant and E_a is the activation energy for the corresponding process. The unrestricted motion of $[\text{C}_{12}\text{Py}]$ is slower for all the considered temperatures, as it has been shown before. However, the activation energy values ($\sim 12.5 \text{ kJ}/\text{mol}$) are very similar despite of the chain length, as one can see from the almost identical slopes of the dashed lines (Fig. 5.6). The solid line represents the results obtained by Tokuda et al. [134] using NMR methods. The difference between our values of the diffusion coefficient and the latter can be, most likely, explained by the different time scales, on which the two experimental methods operate. As it was demonstrated by numerous molecular dynamics simulations [56], the gradient of MSD-curves changes with observation time, causing different regimes of dynamics. With QENS one gets the short-time (on the picosecond time scale) diffusion coefficient, whereas PFG NMR probes the long-time diffusion coefficient on the microsecond time scale.

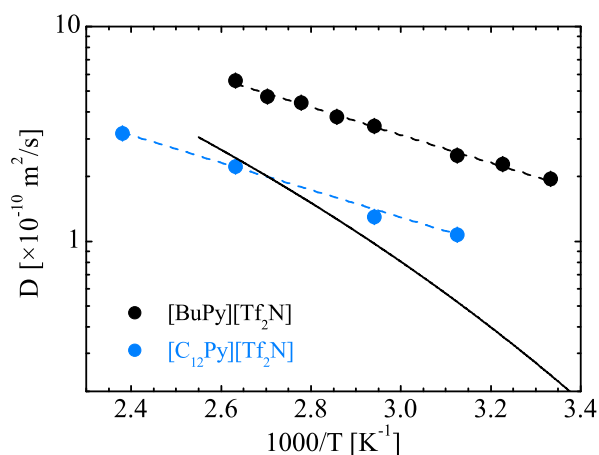


Figure 5.6. Diffusion coefficient D as a function of the inverse temperature; the dashed lines represent fits to Eq. 5.4 and the solid line is the results of PFG NMR measurements

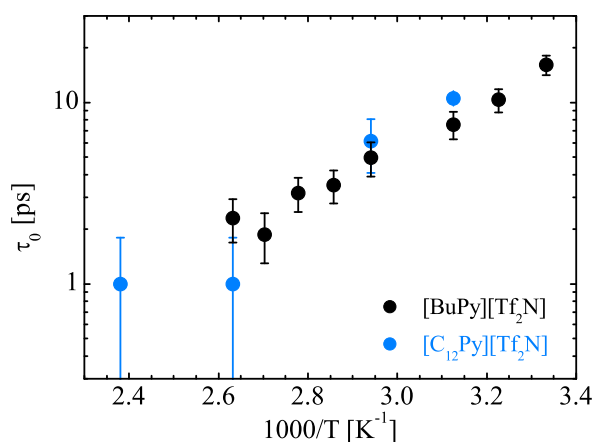


Figure 5.7. Residence time τ_0 as a function of the inverse temperature

The choice of an analytical model for the localized process is not straightforward. All the three models mentioned in Chapter 2.3 are equally acceptable from the physical point of

view. Thus, all of them were applied and $S_{\text{loc}}(Q, E)$ in Eq. 2.16 was sequentially substituted by Eq. 2.28 (continuous rotational diffusion), 2.29 (diffusion in a sphere) and 2.41 (Gaussian model). The fitting proved that all the dynamic structure factors could fairly capture the scattering profiles. The reason for this can be clearly seen from Figure 5.8, where the EISF(Q) dependences of all the three models are plotted. As an example the following radii of confinement were taken accordingly: $R=0.75 \text{ \AA}$, $a=1.00 \text{ \AA}$ and $\sigma=0.45 \text{ \AA}$. The corresponding EISF-curves are nearly indistinguishable in the Q -range accessible in a QENS experiment. A slight difference shows up only for $Q > 2 \text{ \AA}^{-1}$.

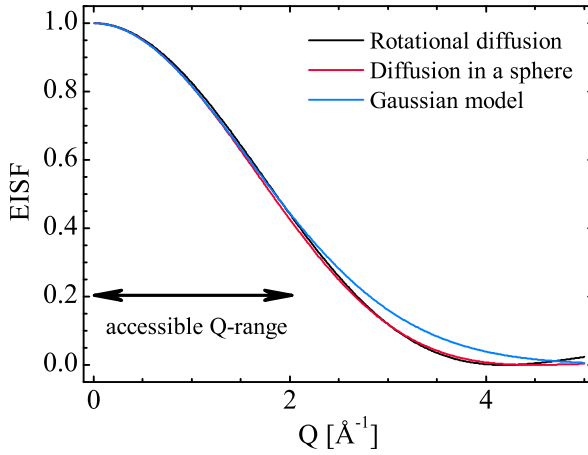


Figure 5.8. EISF as a function of the wavevector transfer calculated from Eq. 2.28, 2.31 and 2.41

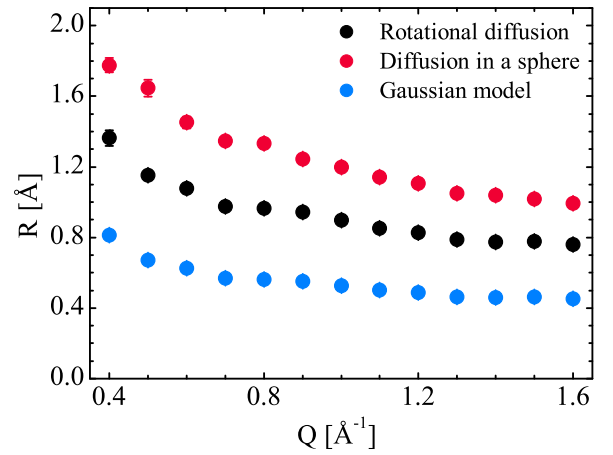


Figure 5.9. Radii of confinement as a function of wavevector transfer Q calculated according to three different models

Before further discussion, a technical digression about the fitting procedure is in order. The experimental spectra are fitted to the scattering functions, which contain a convolution of two functions. Therefore, the choice of an analytical model for the localized process may influence the fit parameters of the slower translational diffusion. However, it might not be the case if the motions are relatively well separated on the time scale of the experiment. Table 5.3 summarizes the fit parameters of the jump diffusion model calculated for the [BuPy] cation at $T=300 \text{ K}$, while different models were applied to render cation motion in a confinement. The convolution with the rotational diffusion scattering function provides the parameter values closest to the results of the model-independent fits, because the series of this model converge quite rapidly. The diffusion in a sphere and Gaussian models with a broader spectrum of Lorentzians in the series yield the values, which decline to a greater extent. So, the effect of the model choice is present, luckily it does not lead to unreasonable divergence of the results.

Although all the models give reasonable results for every Q -group independently, a difficulty was encountered. All of the evaluated parameters, as radii, relaxation times or diffusion

Table 5.3. Diffusion coefficient D and residence time τ_0 , derived for [BuPy] at $T=300$ K from the jump diffusion model convoluted with different models for localized motion

Model	$D \cdot 10^{-10}$, m ² /s	τ_0 , ps
Model-independent	1.95 ± 0.11	16 ± 2
Rotational diffusion	2.00 ± 0.11	18 ± 2
Diffusion in a sphere	1.70 ± 0.06	17 ± 2
Gaussian model	1.95 ± 0.05	25 ± 1

coefficients exhibit a Q -dependence (Fig. 5.9), which is physically not correct. A possible explanation of this effect is that we observe a superposition of dynamical processes from all the protons within the cation, characterized by different mobility. Therefore, a distribution of volume sizes, in which they can move, should be taken into account (Fig. 5.11). Introduction of new parameters associated with distribution functions, however, compels an improved fitting routine, namely, the 2D-approach discussed in Chapter 4. Starting from now, if not otherwise stated, 2D-fitting is applied.

5.3.1 Dynamic structure factor for the alkyl chain and the pyridinium ring

To simplify the analysis of the localized motions of the pyridinium-based cation [BuPy], two types of partially deuterated samples were studied. This allowed extracting the contributions to the faster process from different parts of the cation: either the pyridinium ring or the alkyl chain was deuterated. The QENS-experiments were carried out on FOCUS with the same setting of the instrument used before ($\lambda=5.75$ Å). It is necessary to keep in mind that the coherent contribution becomes more significant with increasing degree of deuteration. However, in our recent investigation [125] it was shown that although collective effects can influence unrestricted jump-diffusion, the localized dynamics remain unaffected. A broad QENS-contribution, which is related to the spatially restricted motions, appears in the spectra of both partially deuterated samples (Fig. 5.10). If the pyridinium ring were immobile relative to the centre of mass of the cation, the observed QENS-line resulting from the long-range diffusion would be much narrower. Thus, it is necessary to consider both restricted and global motions for both parts (pyridinium ring and alkyl chain) of the cation.

The local motion of the butyl chain can be envisaged as chain librations relative to the carbon atom, where the chain is attached to the ring, as torsional rotations of the chain backbone, or as methyl group rotations. In order to capture this diversity, a scattering law

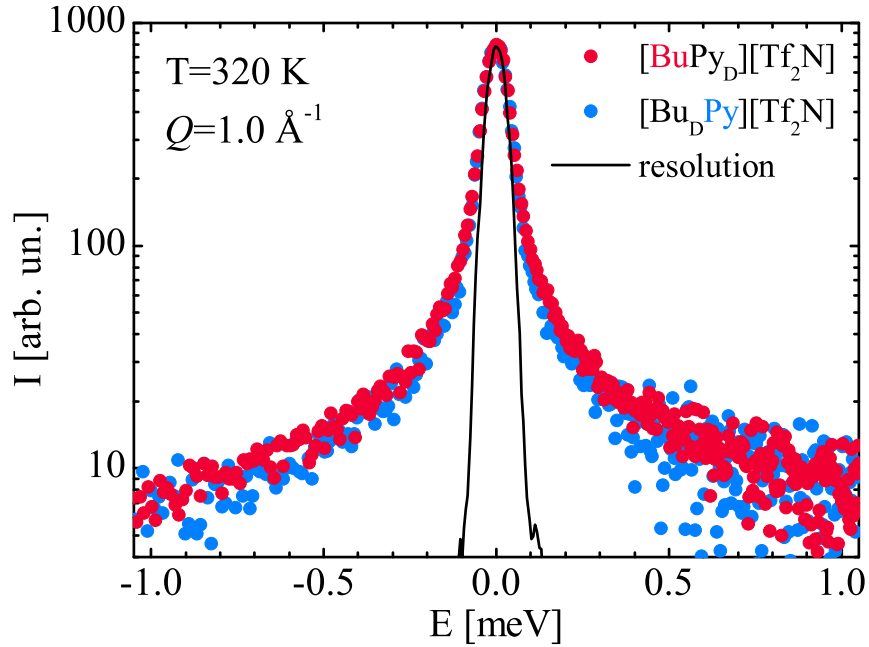


Figure 5.10. Comparison of the measured quasielastic intensity for two partially deuterated samples at $T=320$ K and $Q=1.0 \text{ \AA}^{-1}$.

based on the Gaussian model with a distribution function was used (Fig. 5.11–5.12). The other models discussed in this work were applied as well. However, the continuous rotation model led to non-physical temperature dependence of the relaxation time. The diffusion in a sphere model yielded results, similar to those of the Gaussian model. The diffusion coefficients had approximately the same values; the radius of an impermeable sphere being ~ 2.25 greater than the characteristic size of a confinement with soft boundaries. So, as the diffusion in a sphere model is computationally more expensive, it was decided in favour of the Gaussian model for performing further computations.

The simplest distribution law used to describe the local dynamics of the alkyl groups is a linear variation of the radii of the spherical volumes as a function of the number of the carbon atom, to which the hydrogen atoms are bounded [121, 174]. There are some advanced distribution functions for rigidly fixed molecules, which take into account chain rotation about its own axis or in a cone with or without additional body fluctuations [175]. The latter approach still requires additional information about the molecule structure (bond length and angles). As long as molecular dynamic simulations are not performed for the studied cation, this approach remains just an approximation. Therefore, the total dynamic structure factor for fitting the spectra of [BuPy_D] was taken in the following form:

$$S_I(Q, E) = I_0(Q) \cdot \frac{1}{\pi} \frac{\Gamma_{\text{glob}}}{\Gamma_{\text{glob}}^2 + E^2} \otimes \left\{ \sum_{i=0}^3 p_i \cdot S_G(Q, E; \sigma_i) \right\} \otimes R(Q, E) + a + bE \quad (5.5)$$

where $S_G(Q, E; \sigma_i)$ is expressed by Eq. 2.41, Γ_{glob} is modelled by the jump diffusion (Eq. 2.24), $p_i = \{2/9, 2/9, 2/9, 3/9\}$ is the vector of the fractions of the hydrogen atoms in the chain moving in a confinement with the characteristic size of $\sigma_i = \sigma_{\text{min}} + (\sigma_{\text{max}} - \sigma_{\text{min}}) \cdot i/3$, $i = \{0, 1, 2, 3\}$. The results of the fitting procedure are summarized in Table 5.4 and graphically presented in Figure 5.13–5.14.

Table 5.4. Diffusion coefficients for the long-range and localized diffusion, D and D_{loc} , residence time τ_0 and characteristic radii of confinement, σ_{min} and σ_{max} , as obtained from the fitting of the [BuPy_D] data with Eq. 5.5 at different temperatures

T , K	$D \cdot 10^{-10}$, m ² /s	τ_0 , ps	$D_{\text{loc}} \cdot 10^{-10}$, m ² /s	σ_{min} , Å	σ_{max} , Å
310.0	1.62±0.02	16.5±0.3	9.24±0.03	0.108±0.003	0.873±0.002
330.0	2.15±0.02	11.4±0.3	10.49±0.03	0.160±0.003	1.026±0.002
350.0	2.85±0.02	6.7±0.2	12.59±0.03	0.225±0.003	1.116±0.002
370.0	3.69±0.02	5.0±0.2	14.84±0.03	0.285±0.002	1.222±0.002
390.0	4.64±0.02	4.0±0.2	16.20±0.02	0.367±0.003	1.307±0.002

There are several points to discuss about the evaluated parameters. If we compare the values of the diffusion coefficient related to the long-range diffusion, we will see that the inclusion of the radii distribution function leads to systematically lower values of the diffusion coefficient than in the case of the model independent fits. The reason lies in the inverse square dependence of the Lorentzian linewidths on the confinement size in the series (Eq. 2.41). The larger the value of the radius, the greater the number of narrower Lorentzians is in the series. These contributions are comparable with the linewidth associated with the unrestricted

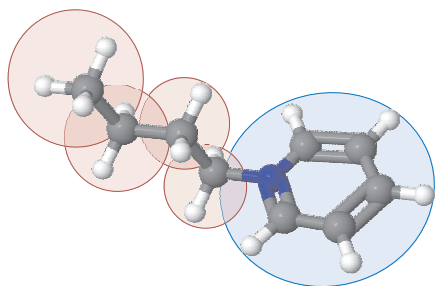


Figure 5.11. Sketch of different possible radii of confinement distributed along the [BuPy] cation

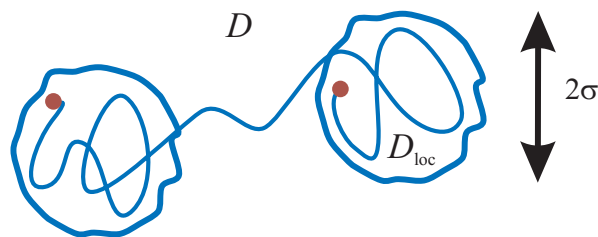


Figure 5.12. Sketch of the different dynamic processes. The localized motion occurs in a volume of the linear size 2σ and is characterized by D_{loc} , while the global process is described by the diffusion coefficient D

motion at higher Q -values. This is a sign that the two processes can be separated on the time scale only approximately, what has been already mentioned.

The second important question is whether it is well-grounded to use only one value of the diffusion coefficient for an adequate characterization of the restricted dynamics. Mukhopadhyay et al. [175] introduced a linear distribution function for both the diffusion coefficient and the radius, assuming that the hydrogen atoms closer to the core of the molecules might move more slowly. Technically, the inclusion of one more parameter in the fit function renders even the 2D-fitting routine unstable. The authors of the above mentioned work avoided this issue by performing fitting with several steps. After carrying out model independent fits, the radii were extracted from the EISF-dependencies. They were used as fixed parameters for the further fits of $\Gamma_{\text{loc}}(Q)$, which gave the values of the diffusion coefficients of the localized motions. However, this approach is legitimate only if the two processes are really distinguishable on the time scale of the experiment, which is not the case for the studied ILs in the investigated temperature range, as it was shown before. Therefore, keeping in mind that it is an approximation, the further analysis will be proceeded with only one “mean” value of the diffusion coefficient characterising the localized motions.

Third, the linear distribution function has its shortcoming. It does not simulate flexibility of the alkyl chain properly. The bond connecting the ring and the chain is rigid and rotations of the first CH_2 -unit is very likely hindered. One can clearly see this from the values of σ_{min} . Although they increase with temperature, they remain even less than the characteristic C-H bond length. It means that the hydrogen atoms closest to the nitrogen atom of the ring are at least partially immobile. The volumes predicted from the linear variation for the outer atoms might also be too large due to steric restrictions. Both σ_{min} and σ_{max} dependencies are given in Figure 5.14 and exhibit steady increase within the considered temperature range due to enhanced flexibility of the chain at elevated temperatures.

As well as in the case of the model independent approach the temperature dependencies of all diffusion coefficients for both the global and the restricted dynamics follow the Arrhenius equation with the parameters listed in Table 5.6.

For what concerns the pyridinium ring, its scattering law was also based on the Gaussian model in order to have the possibility to compare the time characteristics of the localized dynamics. For the pyridinium ring one may consider a sort of out-of-plane librations and rotations. Although it is characterized by a “higher” symmetry, Eq. 2.41 without any modification was not sufficient to predict the profile of the QENS-spectrum. For a consistent description it was necessary to assume that a fraction of the hydrogen atoms remains immobile on the time scale of the experiment, so that the scattering law is given by [76, 176]:

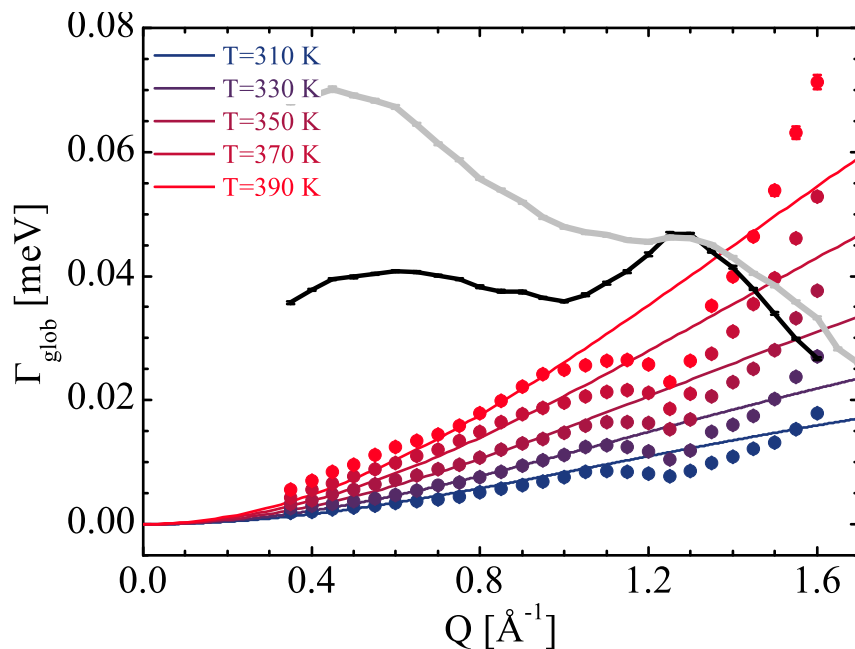


Figure 5.13. Linewidths of the long-range diffusional process as a function of the wavevector transfer Q at different temperatures. The solid colour lines are dependencies expressed by Eq. 2.24 and plotted for the D and τ_0 values evaluated with the help of the 2D-fitting routine for $[\text{BuPy}_D]$ and presented in Table 5.4. The colour symbols are the fit results for the $[\text{Bu}_D\text{Py}]$ spectra without implying a distinct Q -dependence for the long-range diffusion process. The grey and black solid lines represent the Q -dependence of the intensity factor $I(Q)$ for $[\text{BuPy}_D]$ and $[\text{Bu}_D\text{Py}]$ respectively

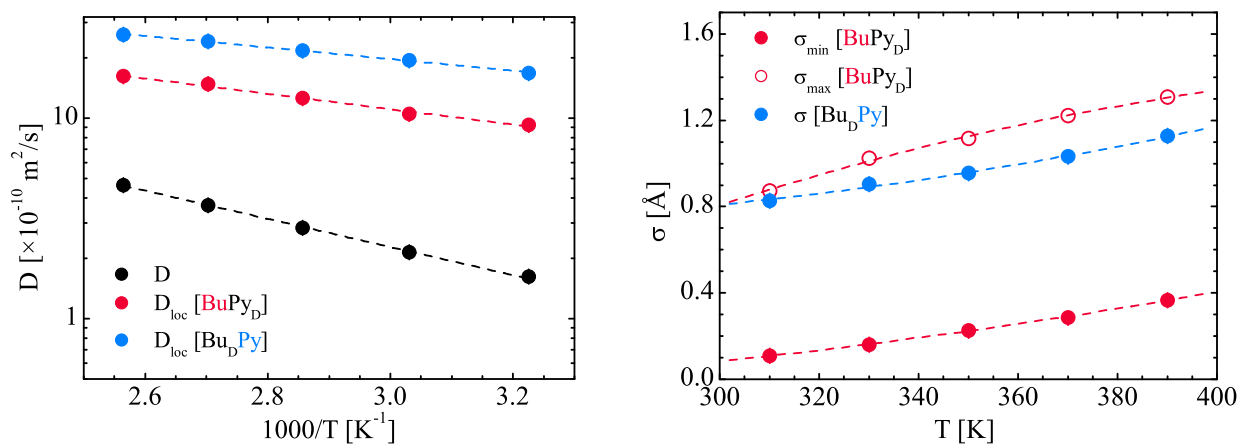


Figure 5.14. *Left:* Diffusion coefficients for the long-range and localized processes of the $[\text{BuPy}]$ cation, D and D_{loc} , as a function of the inverse temperature; the dashed lines represent fits to Eq. 5.4. *Right:* Temperature dependences of the radii characterizing the localized motion of the chain, σ_{min} and σ_{max} , and of the ring, σ . The dashed lines are given as guides to the eye

$$S_I(Q, E) = I_0(Q) \cdot \frac{1}{\pi} \frac{\Gamma_{\text{glob}}}{\Gamma_{\text{glob}}^2 + E^2} \otimes \quad (5.6)$$

$$\otimes \{(1 - p_{\text{mob}})\delta(E) + p_{\text{mob}}S_G(Q, E; \sigma)\} \otimes R(Q, E) + a + bE$$

where p_{mob} denotes the fraction of the mobile particles. The results of the fits are summed up in Table 5.5 and also presented in Figure 5.13–5.14 with the already discussed results, obtained for the sample with the protonated butyl chain.

Table 5.5. Diffusion coefficients of the localized diffusion D_{loc} , characteristic radii of confinement σ , and fraction of mobile particles p_{mob} , as obtained from the fitting of the [Bu_DPy] data with Eq. 5.6 at different temperatures

T , K	$D_{\text{loc}} \cdot 10^{-10}$, m ² /s	σ , Å	p_{mob}
310.0	16.80±0.06	0.827±0.003	0.457±0.002
330.0	19.47±0.05	0.904±0.003	0.514±0.002
350.0	21.73±0.05	0.955±0.002	0.567±0.001
370.0	24.23±0.05	1.032±0.003	0.611±0.001
390.0	26.17±0.06	1.129±0.003	0.625±0.001

As opposed to the [BuPy_D] sample, the intensity factor $I_0(Q)$ of the [Bu_DPy] cation has a more pronounced broad peak around $Q=1.3 \text{ \AA}^{-1}$. This is an indication of substantial coherent scattering in this Q -range, which has a strong impact on the narrower linewidth of the diffusional process. That is why Γ_{glob} was included in Eq. 5.6 without implying any explicit analytical dependence on the wavevector transfer Q . The narrow Lorentzian linewidths are visibly modulated at the above mentioned Q -value at all the temperatures. It is obvious that these dependencies cannot be used for evaluation of the parameters of the jump-diffusion model, D and τ_0 . Still, it is worth mentioning that the linewidths of the narrow Lorentzian contribution for both samples are indeed consistent with each other at all the temperatures, giving one more proof of the validity of the developed approach in the data analysis.

The radii of confinement σ are comparable with σ_{max} calculated for the sample with the protonated butyl chain but feature less rapid increase with temperature. Taking into account that σ is only a characteristic size of a confinement with “soft” boundaries, we may estimate the radius of an impermeable sphere equivalent to that confinement. The experimentally established ratio between the parameters of the two models $R/\sigma \approx 2.25$ gives the value of 2.2 \AA for the radius at $T=350 \text{ K}$. It is in agreement with the distance between the centre of the pyridinium ring and the outer hydrogen atoms ($l_{\text{centre-C}} + l_{\text{C-H}} = 1.400 + 1.084 \approx 2.5 \text{ \AA}$ [167]).

The p_{mob} values different from one show that not all the particles are involved in this type of motion, which seems to be hindered. At elevated temperatures the probability to release these dynamics is higher and hence p_{mob} becomes gradually greater.

A linear Arrhenius plot (Fig. 5.14) of the diffusion coefficient D_{loc} points out to a thermally activated process similar to the dependences obtained for [BuPy_D]. Comparing the restricted motions of the alkyl chain and the pyridinium ring, we see that they are characterized by the values of the diffusion coefficient, which are different but of the same order of magnitude. Moreover, the activation energy values (Table 5.6) are pretty close.

Table 5.6. Best fit parameters of the temperature dependences of the diffusion coefficients to the Arrhenius equation (Eq. 5.4)

	$D_0 \cdot 10^{-8}$, m ² /s	E_a , kJ/mol
long-range diffusion	2.93±0.15	13.46±0.15
restricted diffusion, chain	1.57±0.02	7.34±0.04
restricted diffusion, ring	1.45±0.02	5.53±0.05

To sum up, the partially deuterated samples allow a deeper insight into the restricted dynamics. The numerical values of σ , σ_{min} , σ_{max} support the view that the considered localized dynamics do not correspond to the movement of the cation as a whole in the cage formed by its neighbours, but to chain conformations and ring librations, in other words, the dynamics are geometrically restricted. Global rotation of the cation is likely to be much slower [53, 80, 172] and its contribution is implicitly included in the linewidth of the long-range diffusion. The diffusion coefficients of the localized processes turned out to be different for the different parts of the cation; the ring out-of-plane motions are faster than the chain dynamics. Anyway, the characteristic times of the processes are too close on the time scale to be resolved for the totally protonated sample.

5.3.2 Dynamic structure factor for the totally protonated pyridinium-based cations

For the analysis of the totally protonated samples [BuPy][Tf₂N] and [C₁₂Py][Tf₂N] a more general radius distribution function is required to modify the scattering law based on the Gaussian model. As we could see, the volume explored by a particle becomes greater with the number of a carbon atom in the chain, while a fraction of hydrogen atoms in the pyridinium ring remains immobile. Either a Gaussian distribution or a log-normal distribution can be used to model the situation schematically represented in Figure 5.11. The main difference

between the two (among many possible) functions is the behaviour at $r = 0$. The log-normal distribution function ensures $f(r = 0) = 0$, whereas for the Gaussian function $f(r = 0) > 0$. If the radius of confinement is equal to zero, the corresponding particle is immobile. This feature of the Gaussian distribution could be beneficial, because, as discussed, a certain fraction of hydrogen atoms in the alkyl chain and in the pyridinium ring could be immobile (Fig. 5.15). However, when this fraction has quite a great value, the fitting routine produces divergent results. Zero or small radii generate a flat contribution to the spectrum ($D_{\text{loc}}/a^2 \rightarrow \infty$) and can be indeed mixed up with faster components taken into account by the flat background ($a+bE$ -item) in Eq. 2.21. To describe the influence of partial immobility, one can also introduce an additional parameter p_{mob} (the fraction of mobile particles) in the scattering law. But as p_{mob} and the variance of the distribution functions are not independent variables, the fitting routine does not provide stable results as well. To avoid this ambiguity the log-normal distribution function was applied [177]:

$$f(r; \mu, \sigma_{\text{lgN}}) = \frac{1}{\sigma_{\text{lgN}} r \sqrt{2\pi}} \exp \left[-\frac{\ln^2(r/\mu)}{2\sigma_{\text{lgN}}^2} \right] \quad (5.7)$$

where μ is the median of the distribution and σ_{lgN} stands for the standard deviation of the variable's natural logarithm. In the interest of brevity, further in this work the latter will be referred to as the shape parameter, as it determines the broadness and the skewness of the distribution. Taking into account that the mode of the lognormal distribution a (the value that appears most often in a set of data and corresponds to the maximum of the distribution) is related to its median μ as:

$$a = \mu \exp(-\sigma_{\text{lgN}}^2) \quad (5.8)$$

the lognormal distribution can be rewritten in the following way:

$$f(r; a, \sigma_{\text{lgN}}) = \frac{1}{\sigma_{\text{lgN}} r \sqrt{2\pi}} \exp \left[-\frac{(\ln(r/a) - \sigma_{\text{lgN}}^2)^2}{2\sigma_{\text{lgN}}^2} \right] \quad (5.9)$$

Finally, the following expression has been used to fit the data:

$$S_I(Q, E) = I_0(Q) \cdot \frac{1}{\pi} \frac{\Gamma_{\text{glob}}}{\Gamma_{\text{glob}}^2 + E^2} \otimes \left\{ \int_0^\infty f(r_\sigma; a, \sigma_{\text{lgN}}) S_G(Q, E; r_\sigma) dr_\sigma \right\} \otimes R(Q, E) + a + bE \quad (5.10)$$

Table 5.7 contains the final fit results for both samples. The difference in the global diffusion dynamics, already observed in the model independent approach and discussed earlier, is also present in the parameters evaluated within the proposed model, even though all

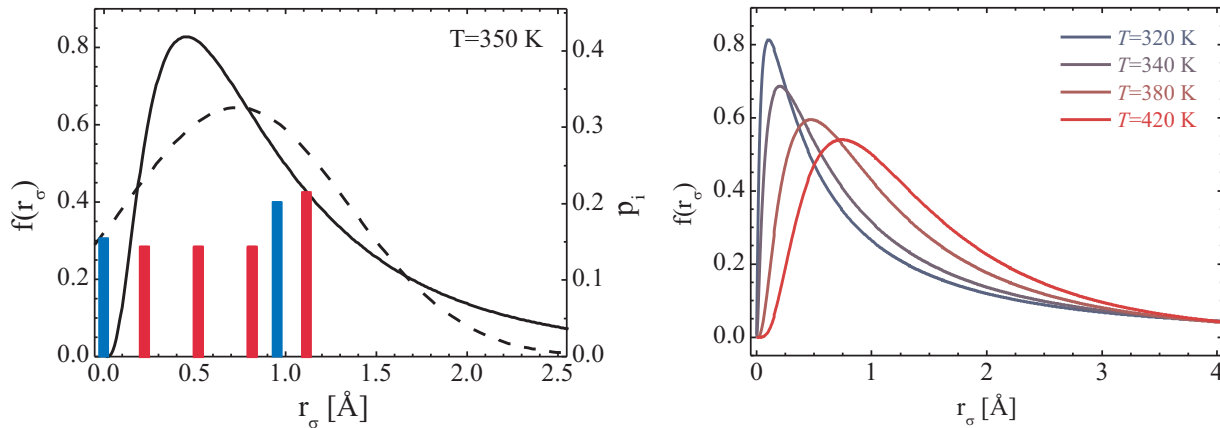


Figure 5.15. *Left:* Radius distribution functions for the [BuPy] cation. The black solid and dashed lines are a log-normal and Gaussian distribution plotted for the values through fitting to Eq. 5.10 at $T=350$ K. The bar plot is the discrete distribution function p_i at $T=350$ K introduced to describe localized motion in the butyl chain and the pyridinium ring (see 5.3.1, Eq. 5.5, 5.6). The red and blue colours denote the chain and ring contribution respectively. *Right:* Radii distribution function of the [C₁₂Py] cation at different temperatures

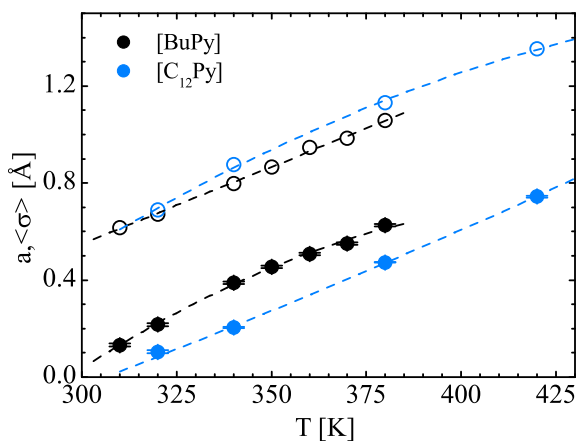


Figure 5.16. Temperature dependence of the linear dimension of the region with a soft boundary for the two pyridinium based ILs. The solid symbols denote the mode a of the log-normal distribution function listed in Table 5.7; the open symbols represent the mean radius values $\langle \sigma \rangle$. The dashed lines are guides to the eye

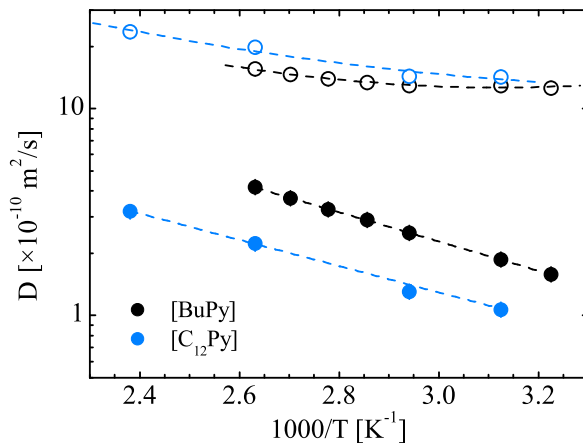


Figure 5.17. Diffusion coefficient as a function of the inverse temperature for the two cations with side chain of different length. The solid symbols represent the diffusion coefficients of the global translational process, whereas the diffusion coefficients of the restricted dynamics are shown by the open symbols. The dashed lines are guides to the eye

Table 5.7. Diffusion coefficients for the long-range and localized diffusion, D and D_{loc} , residence time τ_0 and mode and shape parameter of the log-normal distribution, a and σ_{lgN} , as obtained from the fitting of the [BuPy] and [C₁₂Py] data with Eq. 5.10 at different temperatures

T , K	$D \cdot 10^{-10}$, m ² /s	τ_0 , ps	$D_{\text{loc}} \cdot 10^{-10}$, m ² /s	a , Å	σ_{lgN}
[BuPy][Tf ₂ N]					
310.0	1.58±0.01	11.4±0.3	12.6±0.2	0.132±0.006	1.32±0.06
320.0	1.87±0.01	8.9±0.2	13.0±0.3	0.217±0.006	1.09±0.05
340.0	2.51±0.02	7.2±0.2	13.0±0.2	0.389±0.005	0.83±0.02
350.0	2.89±0.02	6.5±0.2	13.4±0.2	0.454±0.004	0.78±0.01
360.0	3.26±0.02	5.8±0.2	14.0±0.2	0.508±0.005	0.77±0.01
370.0	3.69±0.02	4.1±0.2	14.7±0.2	0.551±0.005	0.74±0.01
380.0	4.18±0.03	4.1±0.2	15.6±0.2	0.626±0.006	0.70±0.01
[C ₁₂ Py][Tf ₂ N]					
320.0	1.07±0.05	10.5±0.6	14.3±0.3	0.104±0.012	1.51±0.03
340.0	1.31±0.02	6.1±0.5	14.4±0.2	0.205±0.007	1.27±0.02
380.0	2.23±0.03	0.0	19.8±0.3	0.473±0.010	0.93±0.02
420.0	3.18±0.07	0.0	23.6±0.4	0.744±0.010	0.75±0.02

the absolute values of the diffusion coefficients are slightly less than in the previous case, owing to the introduced distribution function (Fig. 5.17). As for the localized dynamics, superposition of different motions closely distributed on the time scale occurs and cannot be separated. Due to the complexity of the studied dynamic picture the temperature dependence of the “mean” diffusion coefficient D_{loc} associated with the restricted process is not described by the Arrhenius law in contrast to the previous results. Moreover, for [BuPy] D_{loc} increases insignificantly with temperature, what could be also inferred from $\Gamma_{\text{loc}}(Q)$ in the model independent approach (Fig. 5.5, 3a–b).

The other studied pyridinium-based IL [C₁₂Py][Tf₂N] has a dodecyl chain connected to the ring. The alkyl substituent contains 25 protons, in contrast to 9 protons in the [BuPy] cation. So, the relative contribution of the five protons of the ring to the total scattering is less significant in the case of [C₁₂Py][Tf₂N]. Thus, one may neglect the superposition of the chain and the ring localized motions and consider only the chain dynamics. On the other hand, the dodecyl chain has more degrees of freedom concerning torsional rotations; its higher flexibility complicates the analysis. In the temperature range close to the melting points of both samples ($T \sim 300$ K) their localized dynamics are characterized approximately by the same value of D_{loc} . However, gradual increase in temperature drives conformational

changes in the alkyl chain and it starts “melting”. As the result the localized diffusion coefficient for [C₁₂Py] becomes larger relatively to that of [BuPy] at higher temperatures.

Figure 5.15 displays the radius distribution functions at different temperatures for the [C₁₂Py] cation. With the temperature increase the distribution function gradually becomes narrower, but in no case narrower than for the [BuPy] cation at the corresponding temperature, and shifts to greater radii. The latter is illustrated in Figure 5.16 additionally, where the temperature dependences of the mode of the distribution function and the mean values are presented. The mode is not a very informative characteristic, it turns out to be even less for [C₁₂Py] than for [BuPy] despite of the higher flexibility of the dodecyl chain. The mean spatial dimension of the confinement suits better in this case, as it takes into account the shape parameter of the distribution function. Although a real mean value must be calculated by integrating from 0 to infinity, the presented values were obtained for a physically reasonable r_σ -range, which was used during the fitting procedure as well. Quite low values of the mode a at T=300–340 K and correspondingly high values of the shape parameter σ_{ign} are a sign of the partial immobility of the butyl and dodecyl chains in this temperature range, when only its outer part undergoes conformational changes.

Thus, opposite to the slower global translational diffusion the localized dynamics of the [C₁₂Py] turned out to be richer and faster than for [BuPy] especially at higher temperatures. This information could only be obtained implying a radii distribution function and remains inaccessible for the commonly applied model independent approach.

5.4. Exploring the relaxation time landscape of the cationic dynamics

The previously discussed spectra of the pyridinium-based ILs were measured using only one setting of FOCUS with the wavelength of incident neutrons $\lambda=5.75$ Å, which provided a resolution function with FWHM=60 μeV and a corresponding observation time t_{obs} of 22 ps (Fig. 3.3). Although valuable information can be obtained from the quasielastic broadening observed under these experimental conditions, some details remain undisclosed. First, all the applied fit models include a flat contribution, which accounts for faster unresolved processes (Eq. 5.5, 5.6). If to expand the dynamic range from the energy gain side to a value of $-4.0 - -3.0$ meV, it becomes visible that this component can only roughly be presented as a linear function and only for a limited energy window ($\sim [-1.0, 1.0]$ meV), its linewidth being close to the value of 1.2–1.5 meV. Second, the single Lorentzian describing the global

diffusion is an acceptable approximation only for a coarser resolution function. This description is not valid any more for a backscattering spectrometer with finer resolution [79]. Therefore, we expanded the observation time scale by performing QENS-experiments on the two partially deuterated samples [BuPy_D] and [Bu_DPy] on TOFTOF at FRM II with two complementary wavelengths of incident neutrons $\lambda=3.00 \text{ \AA}$ ($t_{\text{obs}} \sim 3 \text{ ps}$) and $\lambda=12.0 \text{ \AA}$ ($t_{\text{obs}} \sim 150 \text{ ps}$) at the temperature of $T=310 \text{ K}$.

Neutrons with $\lambda=3.00 \text{ \AA}$ were intended to probe relaxation processes faster than 1 ps. The global diffusion and localized dynamics observed in the FOCUS spectra ($\lambda=5.75 \text{ \AA}$) can not be resolved in this case and were modelled by a single Lorentzian contribution without applying any explicit analytical expression for its analysis. To prove the validity of this approach, the best fit parameters and the corresponding fit model (Table 5.4) were used to generate an artificial spectrum of [BuPy_D] for the coarser resolution function at $\lambda=3.00 \text{ \AA}$. At the Q -values of 1.4 and 1.5 \AA^{-1} the linewidths of the narrow Lorentzian component in the simulated spectrum equal 55 and 60 μeV ; whereas for the measured Q -set of the spectra ($\lambda=3.00 \text{ \AA}$) these quantities amount to 41 and 53 μeV , respectively. This demonstrates that the long-range as well as the localized components, seen with $\lambda=5.75 \text{ \AA}$, are merged into a single Lorentzian contribution for the coarser instrumental resolution. At the same time the broader contribution is, indeed, characterized by the linewidth of 1.1 meV, close to the estimated value in the case of $\lambda=5.75 \text{ \AA}$.

The narrower Lorentzian curve $\Gamma_{\text{eff}}(Q)$, which substitutes more precise description of the long-range and localized processes seen with the wavelength $\lambda=5.75 \text{ \AA}$, may be treated as an indication of a diffusional process with characteristics such as “effective” diffusion coefficient, which depends on the chosen observation time [98]. But this approach is quite descriptive and does not allow to consider the relaxation time landscape in more detail. Even for $\lambda=5.75 \text{ \AA}$ the process denoted as the long-range diffusion is a superposition of translational and rotational motions of the whole cation, occurring on a similar time scale. Thus, introduction of an “effective” diffusion coefficient does not simplify the analysed picture of molecular motions and the following scattering law was used for fitting the data collected at $\lambda=3.00 \text{ \AA}$:

$$S_I(Q, E) = I_0(Q) \cdot \frac{1}{\pi} \frac{\Gamma_{\text{eff}}}{\Gamma_{\text{eff}}^2 + E^2} \otimes \otimes \{(1 - p_{\text{mob}})\delta(E) + p_{\text{mob}}S_G(Q, E; \sigma_{\text{fast}}, D_{\text{fast}})\} \otimes R(Q, E) + a + bE \quad (5.11)$$

where the faster process with the linewidth of $\sim 1 \text{ meV}$ was modelled by the Gaussian model with the parameters D_{fast} and σ_{fast} ; p_{mob} is the fraction of mobile particles. The best fit parameters for the both partially deuterated samples are listed in Table 5.8. In order not

Table 5.8. Diffusion coefficients D_{fast} , confinement radius σ_{fast} and fraction of mobile particles p_{mob} for the fast localized process, as obtained from the fitting of the [BuPy_D] and [Bu_DPy] data with Eq. 5.11 at the temperature $T=310$ K

sample	$D_{\text{fast}} \cdot 10^{-10}$, m ² /s	σ_{fast} , Å	p_{mob}
[BuPy _D]	35.0±0.4	0.510±0.004	0.922±0.008
[Bu _D Py]	35.1±0.4	0.486±0.004	0.958±0.009

to place too many restrictions in the fit model, p_{mob} was not fixed. However, the estimated values of this adjustable parameter turned out to be anyway close to one. Surprisingly, no distinct difference between the dynamics of the ring and chain was detected on the time scale faster than 1 ps. This fact points out to the common character of this rattling motion. On the other hand, the linewidths of $\Gamma_{\text{eff}}(Q)$ of the ring are definitely narrower at every accessible Q -group than those of the chain. It means that the slower dynamics of the hydrogen atoms are defined by the part of the cation, to which they belong, as it was observed and analysed for the FOCUS spectra ($\lambda=5.75$ Å).

In contrast to $\lambda=5.75$ Å, the wavelength of $\lambda=12.0$ Å provides quite a narrow resolution function (FWHM = 7–8 μeV), which allows to investigate the slowest detected diffusional process in more detail. As it turned out, the slow translational motion cannot be described by a single relaxation time or one Lorentzian, as in the case of the FOCUS data. In the time domain, this means, that the intermediate scattering function $I(Q, t)$, which is a Fourier transform of the dynamic structure factor:

$$I(Q, t) = \int_{-\infty}^{\infty} S(Q, E) \exp\left(i\frac{E}{\hbar}t\right) dE \quad (5.12)$$

deviates from the exponential behaviour at larger times, when the so-called α process occurs. It succeeds the ballistic regime at shorter times, when the particles move almost freely, and β -process at intermediate times, when the particles are trapped in the cages formed by their neighbours [58]. The deviation of the final decay from the exponential behaviour is quite a common situation for polymers and glass forming materials; the intermediate scattering function $I(Q, t)$ is often approximated by the so-called stretched exponential function (also known as Kohlrausch-Williams-Watts law) in this case [55, 99, 152, 178–180]:

$$I(Q, t) \sim \exp\left[-\left(\frac{t}{\tau_{\alpha}}\right)^{\beta}\right] \quad (5.13)$$

where τ_{α} is the relaxation time, which may depend on Q , and β is the stretching parameter ($0 < \beta \leq 1$). There are two possible explanations, why the time correlation function features

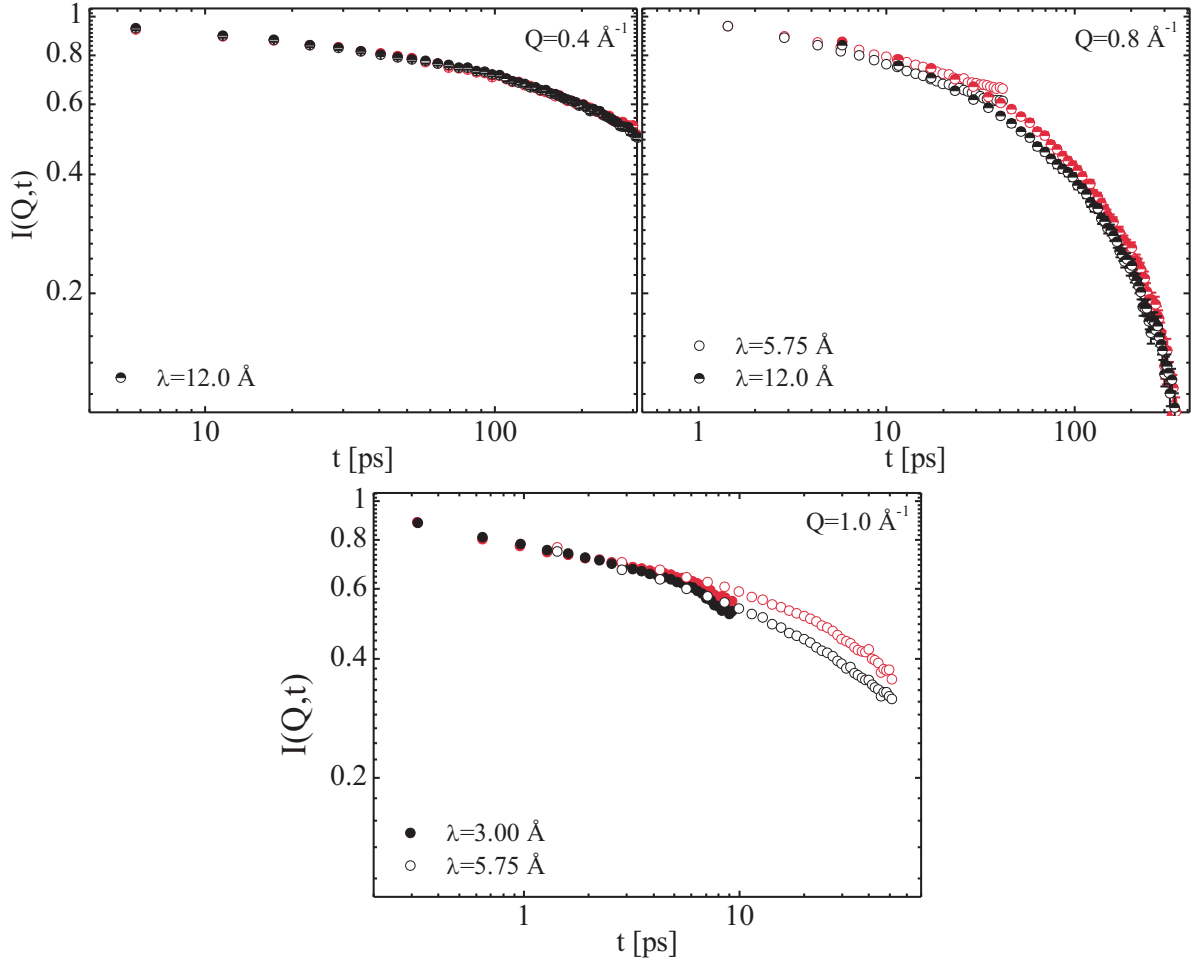


Figure 5.18. Intermediate scattering function of the partially deuterated pyridinium-based ILs obtained within different observation time ranges. The black and red symbols represent the correlation functions of [BuPy_D] and [Bu_DPy], respectively. The wavelengths of incident neutrons ($\lambda=3.00$; 5.75 ; 12.0 Å) are displayed on each plot separately

non-exponential, or non-Debye behaviour [58]. First, the system may be characterized by a distribution of relaxation times due to the disorder and a slightly different neighbourhood of each particle in the system. The second interpretation implies that the disorder of the system causes an intrinsic non-exponential behaviour of each particle. The true reason remains a matter of debate. Mamontov et al. [79] showed that a finer resolution function allows to extract a sub- α diffusional process in an IL, which can be linked to the clustering or nanoscale inhomogeneity effects, as it is spatially localized on the length scale of ≈ 10 Å.

The QENS data were transformed from the (Q, E) - into (Q, t) -space by performing a Fourier transform with the “Fourier Transform Toolkit” in DAVE. The results for different sets of the data (wavelengths of incident neutrons $\lambda=3.00$; 5.75 ; 12.0 Å) and Q -groups for both partially deuterated samples are presented in Figure 5.18. The difference in the decay

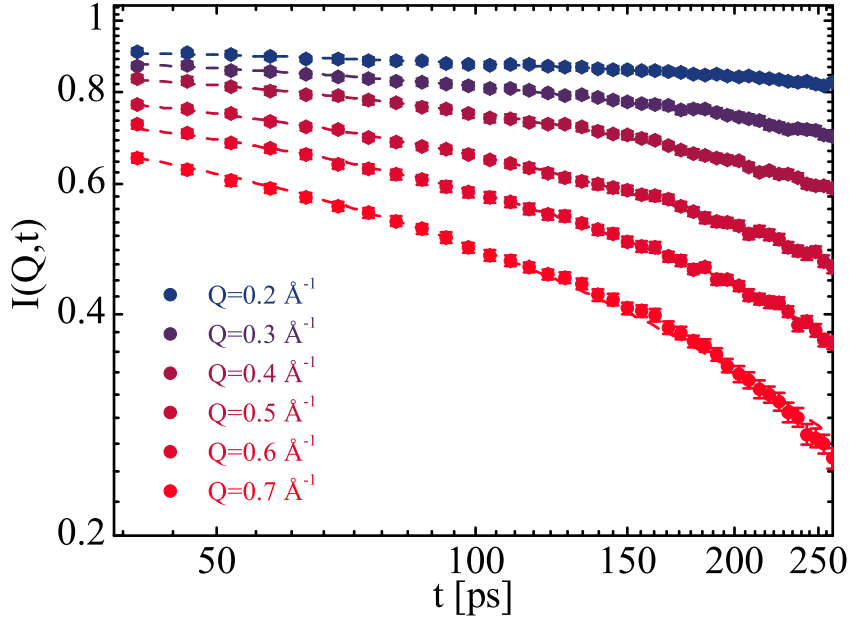


Figure 5.19. Different Q -groups of the intermediate scattering function $I(Q, t)$ of [BuPy_D] (solid symbols) and fits to Eq. 5.13–5.14 (dashed lines)

rates for both the chain and the ring is almost negligible for $t < 1$ ps even at higher Q -values, which is in agreement with the results of the analysis in the (Q, E) -domain. The decrease in the intermediate scattering function of the chain is more rapid at the intermediate time ($1 \text{ ps} < t < 100 \text{ ps}$) than that of the ring, the gap between the two branches of $I(Q, t)$ for each part of the cation being Q -dependent. At larger times ($t > 100 \text{ ps}$) the difference between the two decay curves disappear again, as this time range corresponds to the motion of the cation as a whole. However, only the Q -groups up to 0.8 \AA^{-1} were accessible with the wavelength $\lambda = 12.0 \text{ \AA}$ of incident neutrons. In this case the spatial characteristics of the sub- α diffusional process observed by Mamontov [79] could not be reliably calculated. Therefore, a more descriptive approach based on the stretched exponential function was applied in the time-domain. The 2D-arrays of $I(Q, t)$ were fitted to Eq. 5.13 ($40 \text{ ps} < t < 250 \text{ ps}$, so that the localized processes seen in the FOCUS data can be excluded), assuming that β does not depend on the wavevector transfer Q . Moreover, because a number of investigations on hydrogen-rich materials has shown that the slow dynamics can be characterized by a power law dependence of the characteristic time versus Q [77, 181], the following equation was employed as well:

$$\tau_{\alpha} = \tau_{\alpha 0} (aQ)^{-\nu} \quad (5.14)$$

where $\tau_{\alpha 0}$ corresponds to τ_{α} at $Q=1.0 \text{ \AA}^{-1}$, ν is the exponent characterizing this power dependence and $a=1 \text{ \AA}$. Table 5.9 and Figure 5.19 present the best fit results of $I(Q, t)$ to Eq. 5.13–5.14 for the partially deuterated samples. The calculated values illustrate once more that the long-range process of the different parts of the cation is identical at larger times.

Table 5.9. Characteristic relaxation time $\tau_{\alpha 0}$, exponent ν and stretching parameter β for the slow diffusional process, as obtained from the fitting of the [BuPy_D] and [Bu_DPy] data ($\lambda=12.0 \text{ \AA}$) with Eq. 5.13–5.14 at the temperature $T=310 \text{ K}$

parameter	[BuPy _D]	[Bu _D Py]
$\tau_{\alpha 0}$, ps	97±9	95±8
ν	1.96±0.12	1.96±0.11
β	0.73±0.05	0.76±0.04

To sum up, the experiments on the partially deuterated pyridinium based ILs clearly established that subdivision of the accessible time scale into three regions is reasonable. At shorter times ($< 1 \text{ ps}$) the rattling motions of the protons belonging to the butyl chain or to the pyridinium ring have similar time and spatial characteristics. At the intermediate time ($5 \text{ ps} < t < 50 \text{ ps}$) internal movements of the different parts of the cation come into play. Consequently, a gap between the two branches of the intermediate scattering function appears. At longer times ($t > 100 \text{ ps}$) the correlation function is determined by the long-range motion of the cation as a whole and features a non-Debye relaxation.

5.5. Summary

The main aim in this chapter was to consider different aspects of the picosecond dynamics of two pyridinium-based ILs with the [Tf₂N] anion. For this purpose the samples with different lengths of the alkyl substituent in the cation ([BuPy], [C₁₂Py]), as well as the partially deuterated samples ([Bu_DPy], [BuPy_D]) have been investigated in a broad temperature range.

The low-temperature dynamics were studied by means of the backscattering technique. Both elastic scan and QENS measurements were performed and showed the presence of thermally activated rotation of the end methyl groups. This process appears in the elastic intensity scans of [BuPy_D] as a step-like curve in the temperature range of 100–180 K, whereas the elastic intensity of [Bu_DPy] falls gradually in the whole temperature range.

For the analysis of the QENS-spectra of the ILs in the liquid state several approaches have been applied. The most descriptive model independent fits allowed us to make out two distinct processes occurring on picosecond time scale: spatially restricted dynamics and unrestricted diffusion. As the next step, some analytical models and their modifications with distribution functions were used. The long-range diffusion is satisfactorily described by the jump-diffusion model, the diffusion coefficients changing with temperature according to the Arrhenius equation. However, the observed long-range process is a combination of true translational motion of the cation and its slow rotation as a whole. These processes occur on a fairly close time scale and, hence, cannot be distinguished by QENS. The Gaussian model proved to be the most appropriate in representing the localized motions. The usage of the partially deuterated samples made the independent analysis of the chain and ring dynamics feasible. The flexibility of the alkyl substituent in the cation was modelled by the linear distribution function, whereas the volume, accessible for the protons in the ring, is characterized by one radius. For the totally protonated samples, owing to a larger number of tangled processes, observed at the same time, a more general distribution (log-normal) was employed. This made it possible to compare the dynamics of the two samples with the butyl and dodecyl chains. The influence of the substituent was detected for both processes: the long-range dynamics are slower in the case of $[C_{12}Py]$, while the localized dynamics are characterized by a broader distribution function of radii and larger diffusion coefficients especially at elevated temperatures.

Combining experiments carried out with different wavelengths of incident neutrons and, hence, with different linewidths of the instrumental resolution function, a careful investigation of the relaxation landscape of the pyridinium-based ILs has been performed. The representation of the spectra in the time domain allowed to see that three dynamical regions can be considered in the time range of 0.2–200 ps; the intermediate time range (5–50 ps) exhibits a pronounced difference between the intermediate scattering functions of the butyl chain and the pyridinium ring. A non-Debye behaviour of the slowest process was observed for both samples.

6. Cation dynamics in a PIL

In this chapter QENS experiments on the protic ionic liquid TEA-TF and the interpretation of their results are presented. The studied PIL is formed by a proton transfer from trifluoromethanesulfonic acid, which is considered to be one of the strongest acids, to triethylamine. A property of PILs crucial for electrochemical applications is their anhydrous conductivity and the N-H proton is a key charge carrier in this case. The dynamics of this species, however, have not been totally clarified yet.

For the combination of the acid and the base in TEA-TF the complete proton transfer is expected. The PFG-NMR measurements showed that the diffusion coefficients of H^+ and the amine are similar and greater than that of the anion [130]. This agrees with the idea of a vehicular mechanism of proton transport by triethylammonium (migration of the whole TEA cation). On the other hand, from conductivity measurements lower values of the diffusion coefficient are predicted, because the proton transfer might be incomplete, resulting in the neutral acid and base species, aggregation and association either of ions or uncharged particles.

The presence of hydrogen-donor and -acceptor sites also leads to a fast fluctuating hydrogen bond network [41], which affects melting points, dielectric permittivity, viscosity, and diffusivity, and may contribute to formation of widely discussed ion pairs. The hydrogen bond between cations and anions was studied by several spectroscopic methods. A frequency shift due to the hydrogen bond enhancing anion-cation interaction could be observed by terahertz (THz) and far-infrared (FIR) spectroscopy [182]. Stretching vibrational modes can be investigated by IR spectroscopy in the frequency range around 3000 cm^{-1} [183]. From NMR chemical shifts one can detect an exchange of proton between donor and acceptor sites [183, 184].

Molecular dynamic simulations provide a more straightforward description of hydrogen bond dynamics via correlation functions. For example, the accepted average hydrogen bond lifetime in liquid water under ambient conditions is about 1 ps [185], which is also a characteristic time for a number of dynamical processes connected with single molecule reorientations.

In contrast to this the simulation data on hydrogen bond dynamics in ILs is much more scant; the time range mentioned in these works is broader and specific to a certain IL [41, 48, 186] and hence cannot be viewed as common. Anyway, it may match the energy and time scale accessible in QENS-experiments. To focus on the dynamics of the N-H proton a sample with the deuterated alkyl side chains was investigated in this work (TEA_D-TF). As in this case the incoherent signal comes from the tagged hydrogen atom mainly, it can provide insight into the global motion of the cation and specific dynamics of the proton at the same time.

The mechanism of the proton transport was not the only interest in this chapter. To study the cation dynamics of the totally protonated TEA-TF on different time scales both elastic scan measurements and QENS-experiments were performed on the IN10 and IN5 spectrometers at ILL and FOCUS at SINQ. The temperature range considered during the experiments (2-440 K) encompassed the regions where the sample undergoes several phase transitions with the corresponding changes in the global and localized dynamics of the cation. At higher temperatures all the following types of motions contribute to the quasielastic broadening: long-range ion diffusion, rotation, ethyl groups librations, etc.; they are gradually switched off with the temperature decrease.

6.1. Low-temperature dynamics in TEA-TF

The settings for an experimental investigation of the low-temperature dynamics of TEA-TF on IN10 were the same as in the case of the pyridinium-based IL and are given in Chapter 5.1. The abrupt decrease of the elastic intensity on heating at $T=306$ K and $T=230$ K (Fig. 6.1) agrees with the phase transition temperatures measured by DSC and reported in Table 3.3. As opposed to the heating regime, the temperatures $T=260$ K and $T=213$ K, at which the elastic intensity suddenly increases on cooling, are quite different from those obtained by the DSC-method, because the start of the phase transition in the IL is very sensitive to the cooling rate. To achieve a proper sample thermalisation and satisfactory scattering statistics, the elastic scans measurements could not be carried out at a higher rate than 0.50 K/min, which is much less than a usual experimental setting in a DSC-measurement.

In the same way it was done for [BuPy] the temperature dependence of the elastic intensity of TEA-TF was fitted to the three-fold jump rotation (Eq. 5.1) and rotational diffusion (Eq. 5.2) models at $Q=1.85 \text{ \AA}^{-1}$, where there are no intense structural maxima leading to great coherent contributions (Fig. 6.1). The results of the fits are listed in Table 6.1. The fraction of mobile hydrogen atoms p_{mob} turned out to equal 0.66 and 0.58 for both models,

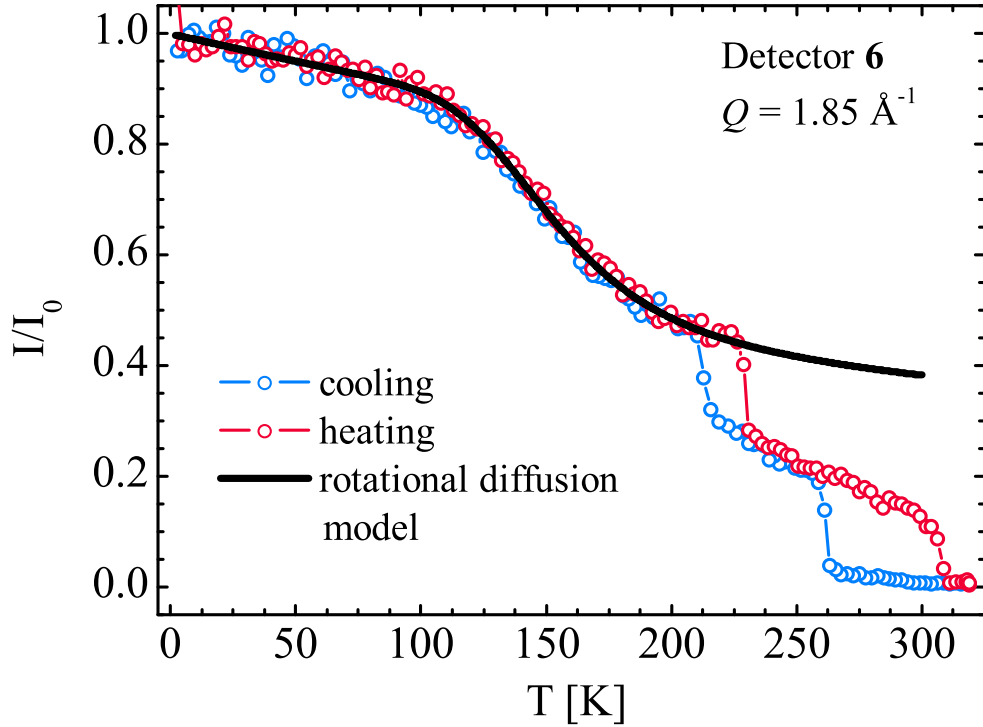


Figure 6.1. Elastic scan measurements on TEA-TF on cooling and heating. The solid line represents the result of the fit to the rotational diffusion model (Eq. 5.2)

respectively. The number of protons in the end methyl groups is nine in total. If to assume that only their rotation causes gradual decrease of the elastic intensity in the temperature range of 100 to 215 K, before the first melting transition occurs, then p_{mob} would be equal to $9/16$ in the ideal case, which is close to the values obtained for both models. The radii of the spheres are also in a good agreement with the length of the C–H bond in the methyl group. This allows concluding that the thermally activated methyl group rotation was detected in the discussed temperature range.

Proton dynamics of TEA-TF in the temperature range between the two melting transitions was analysed on the basis of the QENS-spectra collected on IN5 with the wavelength of

Table 6.1. Fit results of the elastic intensity scans in the temperature range from 2 to 215 K from TEA-TF according to Eq. 5.1 and 5.2

	three-fold jump rotation	rotational diffusion
τ_0 , ps	3.2 ± 0.6	0.57 ± 0.15
E_a , kJ/mol	8.7 ± 0.3	9.5 ± 0.4
R , Å	1.16 ± 0.05	1.16 ± 0.07
p_{mob}	0.66 ± 0.02	0.58 ± 0.02

Table 6.2. Fit results of the QENS spectra of TEA-TF in the temperature range from 250 to 290 K according to Eq. 6.1

T , K	R , Å	p_{mob}	τ_R , ps
250.0	1.07 ± 0.05	0.53 ± 0.03	3.8 ± 0.2
270.0	1.16 ± 0.05	0.55 ± 0.02	3.9 ± 0.2
280.0	1.13 ± 0.04	0.55 ± 0.02	3.7 ± 0.2
290.0	1.47 ± 0.05	0.58 ± 0.02	3.9 ± 0.2

incident neutrons $\lambda=5.00$ Å. The resolution of the instrument allowed to observe a quasielastic contribution, which is enough intense at $T > 270$ K, so that the fitting procedure can be performed. The scattering law used for the fits in the above mentioned temperature range reads:

$$S_I(Q, E) = I_0(Q) \cdot ((1 - p_{\text{mob}})\delta(E) + p_{\text{mob}}S_R(Q, E)) \otimes R(Q, E) + a + bE \quad (6.1)$$

where $S_R(Q, E)$ is defined by Eq. 2.28. The evaluated parameter values are summarized in Table 6.2. The value p_{mob} proved to be equal to 0.55 ($\approx 9/16$); the relaxation time τ_R amounted to ~ 4 ps; the radius of the sphere R increases gradually from 1.16 Å to 1.45 Å, indicating that the carbon atoms attached to the central nitrogen atom become more mobile and the whole alkyl chain becomes more flexible. In the same temperature range the QENS-broadening of the partially deuterated TEA is suppressed and very weak to carry out a fitting procedure, giving another experimental indication that the considered process arises from the alkyl-chains (Fig. 6.2).

As it was mentioned in Chapter 3.1.2, the two successive endothermic phase transitions are ascribed to melting of pure PIL and water-PIL domains. A trace amount of water is present all the time in IL samples. However, the QENS experiments cannot corroborate this statement. First, the spectra at the temperature higher than that of the first melting transition do not exhibit enhanced unrestricted dynamics of the cation compared to the range below the first melting point. The substantial elastic contribution proves that the particles are immobile at least on the time scale of several picoseconds. In its turn, the observed QENS-broadening is connected with the localized motions of the side alkyl chains. But indeed, the relaxation time of this process becomes abruptly less than for the lower temperatures. Second, if to compare the integrated intensities within the energy window of $[-2.0, 2.0]$ meV, we see that the patterns resemble spectra of a solid characterized by narrow sharp Bragg peaks. When the first melting occurs, their position changes and the

redistribution of intensity is observed, but only with the second melting transition all the peaks are smeared. And the integrated intensity exhibits wide maxima typical for molten salts in the liquid state (Fig. 6.3).

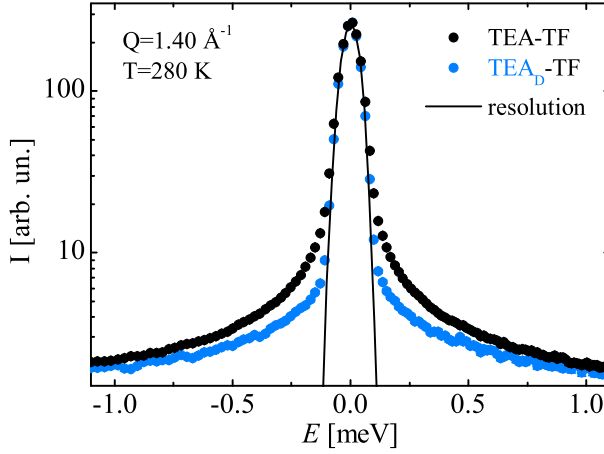


Figure 6.2. QENS spectra of the completely protonated and partially deuterated samples of TEA-TF measured at $T=280$ K and $Q=1.40 \text{ \AA}^{-1}$ (symbols) on IN5 together with the resolution function (solid line)

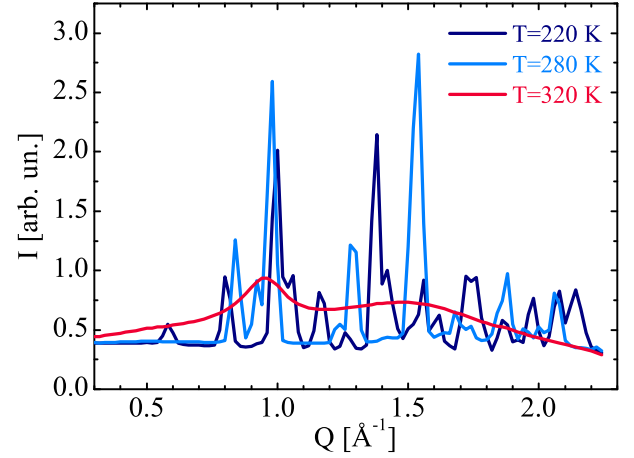


Figure 6.3. Integrated intensity of the partially deuterated sample TEA_D-TF measured on IN5 on heating at the temperatures, when the sample is in the solid or liquid states

6.2. Dynamic structure factor for TEA-TF

The data measured both on FOCUS with $\lambda=5.75 \text{ \AA}$ and IN5 with $\lambda=5.00 \text{ \AA}$ at ambient and elevated temperatures are presented here. As the linewidths of the resolution functions differed by a factor of 1.5 (Table 3.5), the observation time available on FOCUS was 1.5 more than on IN5 and equaled 3 ps (Fig. 3.3).

In the frame of the model independent approach, the QENS-spectra of both TEA-TF and TEA_D-TF in the liquid state can be presented by two Lorentzian curves (see Chapter 2.3). In the same way, as it was applied to the pyridinium-based ILs, the narrower Lorentzian contribution was ascribed to the motion of the whole cation, the second broader curve accounting for various types of localized processes.

The fact that the second broader Lorentzian contribution is necessary to describe the entire spectrum of TEA_D-TF, or $[\text{NH}(\text{C}_2\text{D}_5)_3]$ was surprising. As only one proton, playing a role of a tagged particle, is present in the structure of the cation, one would expect that only one Lorentzian related to the global diffusion is sufficient to capture the profile of the spectra. It is important to keep in mind that the analysis of the TEA_D-TF data is not straightforward

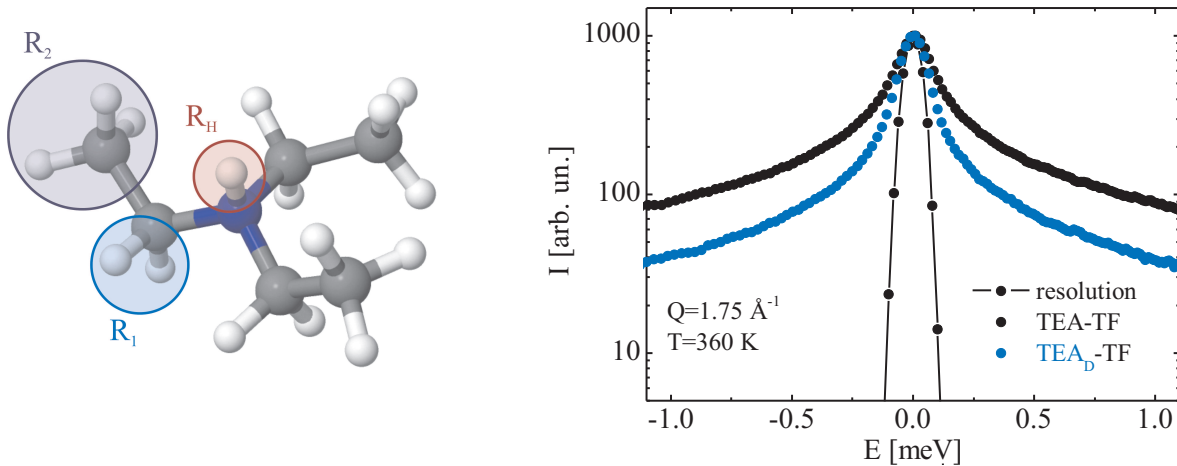


Figure 6.4. *Left:* Cation structure of TEA-TF and sketch of different possible radii of confinement. *Right:* Comparison of the measured quasielastic intensity for the totally protonated and partially deuterated samples of TEA-TF measured at $T=360$ K and $Q=1.75 \text{ \AA}^{-1}$ on IN5.

as in the case of the totally protonated sample. The reason for this it that the spectra of the partially deuterated IL exhibit a substantial coherent component from both the cation and the anion (Table 3.4). The incoherent scattering from the 15 deuterium atoms is also comparable with the contribution from one proton. If we assume that the total scattering of the protonated sample $S_H(Q, E)$ is dominated by the incoherent scattering from the ethyl-chains, then the incoherent contribution from the 15 deuterium atoms can be excluded from consideration by subtracting as:

$$S_{Dcorr}(Q, E) = S_D(Q, E) - \frac{\sigma_D}{\sigma_H} S_H(Q, E) \quad (6.2)$$

where $S_D(Q, E)$ is the experimentally obtained dynamical structure factor of the partially deuterated sample, σ_H and σ_D are the incoherent cross sections of the hydrogen and the deuterium, respectively. Unfortunately, this correction does not allow eliminating the coherent scattering, but our recent experiment on separation of coherent and incoherent contributions indicated that interference effects are crucial for the long-range diffusion only (see Chapter 7). From Fig. 6.4 it is clear that the undertaken correction has not removed the broader QENS-contribution and the N-H proton performs a sort of localized motion on the time scale of the instrument. So, for the further analysis of stochastic motions in TEA-TF several groups of “equivalent” hydrogen atoms can be considered (Fig. 6.4): the single N-H proton (R_H), the six proton of the ethyl chains closest to the nitrogen atom (R_1) and the nine protons of the end groups (R_2).

Taking this into account, it was decided not to include any explicit model for the slower process in the case of TEA_D-TF and to choose the Gaussian model (Eq. 2.41) for describing the localized dynamics of the single proton. The scattering law used for the fits of the partially deuterated sample reads:

$$S_{\text{Dcorr}}(Q, E) = I_0(Q) \cdot \frac{1}{\pi} \frac{\Gamma_{\text{glob}}}{\Gamma_{\text{glob}}^2 + E^2} \otimes S_{\text{G}}(Q, E; R_{\text{H}}, D_{\text{H}}) \otimes R(Q, E) + a + bE \quad (6.3)$$

where D_{H} is the diffusion coefficient characterising the localized dynamics of the proton.

In the case of the totally protonated sample it was possible to perform the fitting routine including the jump-diffusion model (Eq. 2.24) explicitly for the long-range diffusion (Γ_{glob}), the dynamic structure factor for the localized dynamics containing components from each group of the protons:

$$S_I(Q, E) = I_0(Q) \cdot \frac{1}{\pi} \frac{\Gamma_{\text{glob}}}{\Gamma_{\text{glob}}^2 + E^2} \otimes \left\{ \frac{1}{16} S_{\text{G}}(Q, E; R_{\text{H}}, D_{\text{H}}) + \right. \\ \left. + \frac{6}{16} S_{\text{G}}(Q, E; R_1, D_{\text{loc}}) + \frac{9}{16} S_{\text{G}}(Q, E; R_2, D_{\text{loc}}) \right\} \otimes R(Q, E) + a + bE \quad (6.4)$$

The 2D-fit routine, however, does not permit to estimate all the variables in Eq. 6.4 reliably, as the contribution of the N-H proton is much weaker than that of the other 15 hydrogen atoms. To circumvent this, R_{H} and D_{H} were fixed to the values calculated from the TEA_D-TF spectra. Table 6.3 and 6.4 summarize the results of the fits according to Eq. 6.3–6.4

The linewidths of the Lorentzian curve attributed to the long-range diffusion are depicted in Figure 6.5 as a function of Q for both spectrometers. At first glance the results look similar. The linewidth of the protonated sample follows the Q^2 -law at smaller Q -values, whereas deviation from this law is observed in the higher Q -region. The linewidth of the partially deuterated sample features so called “de Gennes line narrowing” [73] (modulations of the linewidth at those Q -values, where there are the maxima of the broad lines in the $I_0(Q)$ dependence), indicating the presence of a relatively large coherent contribution. The “depth” of this modulation depends both on the temperature and the instrumental resolution function. The coherent contribution determines this behaviour; the shorter the observation time-scale is, the more visible are interference effects in the long-range diffusion of the TEA cation. Therefore, the deviation of the quantity $\Gamma_{\text{glob}}^{\text{prot}}(Q)/\Gamma_{\text{glob}}^{\text{deut}}(Q)$ from one is much more pronounced at lower temperatures for the IN5 data.

For some PILs the diffusivity of the N-H proton is considerably facilitated in comparison with that of the cation through the Grotthus mechanism (proton hopping through the hydrogen bond network). The interplay of the vehicular and Grotthus mechanisms has been

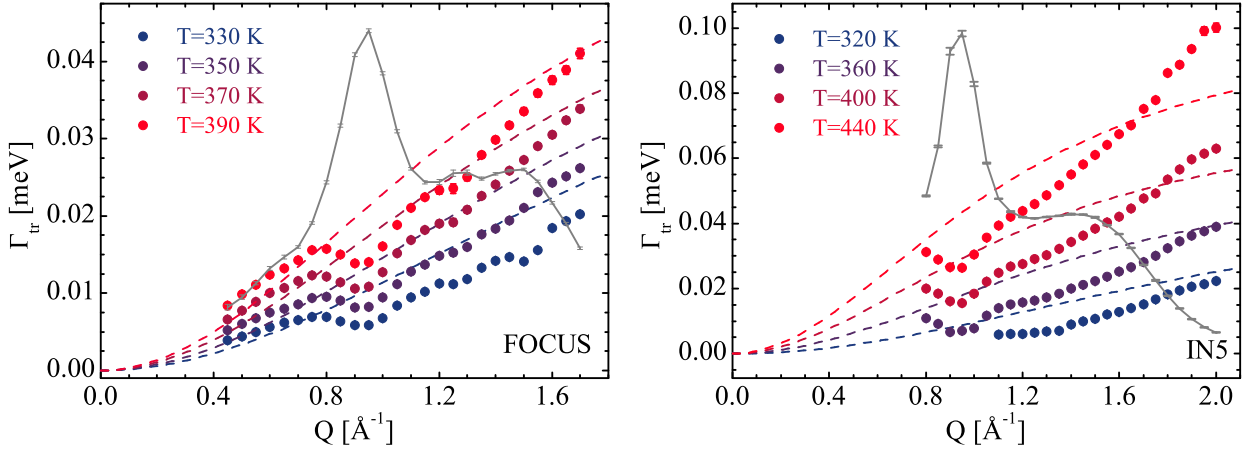


Figure 6.5. Comparison of the fit results for the linewidth of the slow diffusional process obtained for the completely protonated (dashed lines) and partially deuterated samples (solid dots) on FOCUS (left panel) and IN5 (right panel). Owing to the coherent contribution the long-range translational process in TEA_D-TF is slower at those Q -values which correspond to the location of maxima in $S(Q)$. The grey solid line is the $I_0(Q)$ dependence obtained from the spectra of the partially deuterated sample.

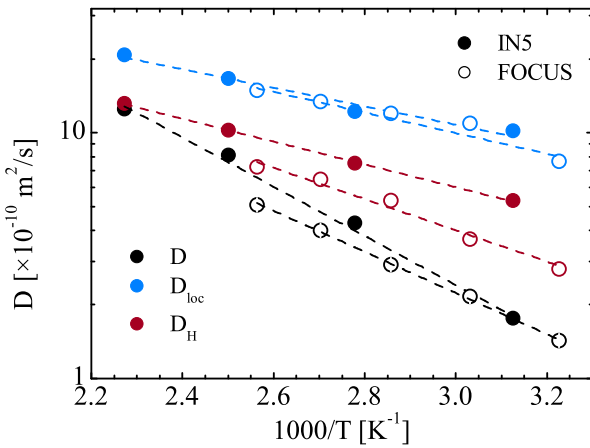


Figure 6.6. Arrhenius plots of the diffusion coefficients describing the long-range diffusion and the localized dynamics of the TEA-cation. The open symbols denote the parameters evaluated from the FOCUS data; the solid symbols represent the IN5 results. The dashed lines are the fits according to Eq. 5.4.

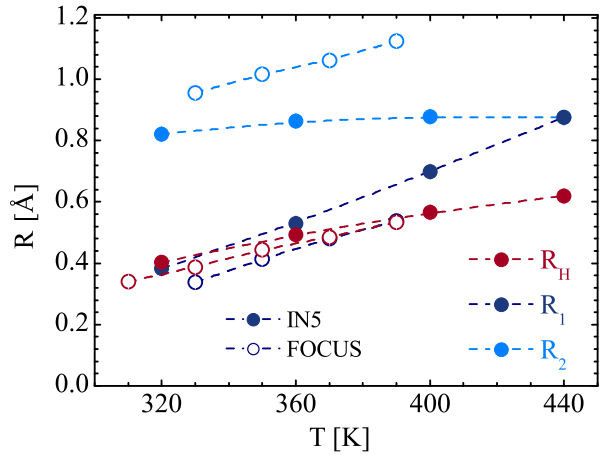


Figure 6.7. Temperature dependencies of the confinement dimension for the three proton groups of the TEA cation. The open symbols denote the parameters evaluated from the FOCUS data; the solid symbols represent the IN5 results. The dashed lines are guides to the eye.

Table 6.3. Temperature dependence of the radii characterizing the localized motion of the different parts of the TEA cation

T [K]	R_H [Å]	R_1 [Å]	R_2 [Å]
FOCUS			
310.0	0.339 ± 0.003	0.010 ± 0.003	0.784 ± 0.003
330.0	0.386 ± 0.003	0.338 ± 0.002	0.954 ± 0.002
350.0	0.444 ± 0.003	0.414 ± 0.002	1.016 ± 0.003
370.0	0.485 ± 0.003	0.481 ± 0.003	1.061 ± 0.004
390.0	0.533 ± 0.003	0.537 ± 0.002	1.125 ± 0.004
IN 5			
320.0	0.403 ± 0.004	0.384 ± 0.002	0.822 ± 0.005
360.0	0.492 ± 0.004	0.529 ± 0.011	0.865 ± 0.006
400.0	0.567 ± 0.005	0.699 ± 0.016	0.877 ± 0.010
440.0	0.620 ± 0.006	0.876 ± 0.004	0.876 ± 0.004

Table 6.4. Best fit parameters of the temperature dependence of the diffusion coefficients characterising the TEA dynamics to the Arrhenius equation (Eq. 5.4)

	$D_0 \cdot 10^{-8}$, m ² /s	E_a , kJ/mol
FOCUS		
long-range diffusion (D)	7.28 ± 0.15	16.04 ± 0.06
restricted motion of the alkyl chains (D_{loc})	1.81 ± 0.02	8.04 ± 0.03
restricted diffusion of the N-H proton (D_H)	3.25 ± 0.04	12.18 ± 0.04
IN5		
long-range diffusion (D)	24.3 ± 0.5	19.18 ± 0.07
restricted motion of the alkyl chains (D_{loc})	1.45 ± 0.01	7.20 ± 0.02
restricted diffusion of the N-H proton (D_H)	1.50 ± 0.03	8.90 ± 0.05

studied for [Im][TFSI] theoretically [187] as well as experimentally [108]. In the latter work it was demonstrated by PGF NMR that the proton hopping is temperature dependent and becomes less efficient with increase in temperature, because the number of hydrogen bonds and their lifetime decrease. The authors also employed QENS to investigate this process and proposed to use the residence time τ_0 in the jump-diffusion model (Eq. 2.24) to quantify its effectiveness. This parameter determines deviation from the Q^2 -law at high Q -values corresponding to length scales smaller than the characteristic interaction distance. However, for partially deuterated samples the estimation accuracy is very poor, owing to the presence of coherent scattering in the most valuable for this purpose high Q -range.

In the case of TEA-TF the whole set of the $\Gamma_{\text{glob}}(Q)$ dependencies for both the protonated and partially deuterated samples does not disclose any enhanced proton dynamics. Moreover, the “apparent” diffusion coefficient of the N-H proton is even less than for the whole cation because of the coherent contribution. But on the other hand, the spectra of TEA_D-TF exhibit a broader Lorentzian contribution and, hence, point out to the existence of a localized process of the N-H proton. So, this hydrogen atom is not tightly connected to the core of the cation and has additional degrees of freedom as compared to the translational motion of the cation as a whole. The origin of this broad component in the spectra of TEA-TF will be discussed later.

For the broader QENS-component of the TEA_D-TF spectra the Gaussian model (Eq. 6.3) yielded the results displayed in Figure 6.6–6.7. For illustrative purposes the fit parameters of the long-range diffusion and the localized dynamics of the ethyl chains are plotted on the graphs as well. The diffusion coefficients depend on the instrumental resolution function, owing to two reasons that may come into interplay. First, very narrow Lorentzian contributions cannot be reliably resolved if the resolution function is much broader, or vice versa broader contributions cannot be fitted if the available dynamical range is too narrow. Second, the dynamics of ILs proved to be decidedly heterogeneous, as it has been stated before in the Introduction; the relaxation processes in ILs have in principle non-Debye behaviour. By altering the linewidth of the instrumental resolution function one adjusts the “exposure time”, during which the information about particle motions is acquired [98]. And it is evident that one Lorentzian (or single exponential decay) for the description, for example, of the long-range diffusion is only an approximation valid for a certain accessible time-scale. That is why, quite often the intermediate scattering function is fitted with the stretched exponential function in the (Q, t) -domain [55, 77].

The restricted motion of the N-H proton is found to be mostly affected by the above mentioned factor, while the IN5 and FOCUS diffusion coefficients characterising the confined motions of the alkyl chains are pretty similar. In the latter case the resolution effect becomes

apparent in the temperature dependence of the confinement size (Fig. 6.7). The difference in the radii of the inner and outer hydrogen atoms is less for the IN5 data than for FOCUS; R_1 and R_2 even tend to one value at elevated temperatures. The interplay of several localized motions occurring on close but different time scales (chain librations, torsional rotations) may lead to this sort of results. If the “exposition” is less than the mean time between distinct conformational states of the chains then the proton is detected around more or less the same position; while the observation time greater than the relaxation time of torsional rotations would allow capturing the proton dynamics over a larger volume.

The temperature dependence of all the diffusion coefficients can be modelled by the Arrhenius equation with the fit parameters summarized in Table 6.4. It is worth mentioning that D_{loc} attributed to the alkyl side groups is very close to the analogous value calculated for the butyl chain of the pyridinium-based IL (Table 5.6).

There remains an open question about the origin of the dynamical process related to the second broad contribution in the spectra of the partially deuterated sample. Several explanations are possible. It seems reasonable that owing to the chain librations and recoil effect the centre of the cation performs a sort of localized motion. But there are some facts that do not corroborate this assumption. First, the diffusion coefficients D_{loc} and D_{H} are not similar. The D_{H} values lie even closer to D , which describes the long-range diffusion. Second, although the radii of confinement are similar to the radii of the inner protons belonging to the ethyl chains at room temperature, their temperature dependence is decidedly different. Moreover, at $T=300$ K near to the phase transition the alkyl chains are partially “frozen”, which is manifested by $R_1=0.010$ Å, whereas the localized process can still be observed for the N-H proton. The second plausible explanation would be that this spatially restricted process and the QENS-broadening associated with it is just a remainder of the global diffusion, which cannot be satisfactorily presented by a single Lorentzian curve and is not visible for the totally protonated sample because of the other quasielastic contributions. This argument can be disproved as well. The trace of the discussed broadening is detectable even at the temperatures lower than the melting point (Fig. 6.2), when the cation is immobile as a whole. On the other hand, dynamics of hydrogen bonds and ion pairs, proton transfer from the cation to the anion and vice versa remain possible explanations, as their time and length scale match nicely those of the discussed localized process.

Only a few molecular dynamic simulations were reported for the family of the studied PIL [183, 184, 188], and unfortunately no information is available for TEA-TF at all. These works proved that interactions in PILs have strong directionality in comparison with similar aprotic liquids due to hydrogen bonds. For the family of alkylammonium salts with the trifluoromethanesulfonate anion it was shown that the most stable and energetically

favourable geometry is when the anion has contact with the N-H bond. The interatomic distances between the key particles (the oxygen atom of TF, the nitrogen atom of TEA and the N-H proton) in the most energetically favourable configuration are $R(\text{O-H})=0.97 \text{ \AA}$ (the proton belongs to the acid); $R(\text{N-H})=1.06 \text{ \AA}$ and $R(\text{O-H})=1.59 \text{ \AA}$ (the proton belongs to the base) [184, 188]. The characteristic size of the confinement with a soft boundary is about 0.45 \AA ($T=350 \text{ K}$). It means that the diffusion in a sphere model would yield a value of approximately 1.0 \AA , the correlation time $\tau_0 = R_{\text{H}}^2/D_{\text{H}} \approx 4 \text{ ps}$. This estimation affirms the assumption that the observed localized process might be connected with the proton exchange between the ions and formation of ion pairs.

6.3. Summary

Both the low temperature dynamics and the dynamics of TEA-TF in the liquid state have been studied and summarized in this chapter. The measurements performed on a backscattering spectrometer showed the presence of thermally activated methyl group rotation at temperatures below the first melting point. The temperature range between the two endothermic phase transitions was investigated by means of the QENS-method. This region was also characterized by localized motions of the end methyl groups, while the core of the TEA cation remained “frozen”. Thus, no individual melting transitions of PIL-water and pure PIL domains were detected. Moreover, the integrated intensity clearly displayed two distinct diffraction patterns for the temperatures below the first and the second melting points.

The dynamical behaviour of the totally protonated and partially deuterated samples have been compared for the temperatures higher than the second melting phase transition. The long-range diffusion, as well as the localized process was observed for both samples. The spectra profiles were satisfactorily captured by the scattering law that included the jump-diffusion model and the Gaussian model for the separate groups of the hydrogen atoms in the cation. The most important finding in this context was the enhanced dynamics of the N-H proton detected in the spectra of the partially deuterated sample $\text{TEA}_{\text{D}}\text{-TF}$.

7. Collective and single particle dynamics

QENS analysis of stochastic motions in hydrogen-rich samples is usually started with the assumption that the incoherent signal from hydrogen atoms determines the total scattering intensity, while the coherent contribution is considered to be negligible. On the other hand the structure factor of many ionic liquids features some so-called pre-peaks in the Q -range accessible normally by QENS [9, 47, 189–191]. Thus, this assumption for such kinds of samples is questionable.

The origin of these pre-peaks in ILs is the source of a long-lasting and extensive debate [189, 192]. In this respect, the issue has been most thoroughly explored for the class of imidazolium based ILs. At first, their pre-peaks were interpreted as a fingerprint of highly structured domain formation on the nanometer length scale. The presence and position of the first maximum at the lowest Q -value exhibited dependence on both the number of carbon atoms in the side alkyl chains and temperature [9, 190]. Therefore, alkyl substituents were considered as a driving force for this intermediate range order. Owing to the recent experiments [191] this explanation has gained credence. However, the possibility that these low Q diffraction features reflect nm-scale structural organisation has been questioned. First, the pre-peaks or the first sharp diffraction peaks are not a peculiar or exclusive feature of ILs. It was also highlighted that the presence of the bulky alkyl chains leads to different patterns of ion coordination. The pre-peaks could be simply a result of this geometrical anisotropy, but not a result of creating complex morphologies from the alkyl tails [47, 192]. Thus, the broad peak at around 1.4 \AA^{-1} corresponds to a spatial correlation length of 4.5 \AA and points out to intramolecular and close contact intermolecular interactions (correlations between ion pairs, adjacent alkyl chains). The peak at around $0.8\text{--}0.9 \text{ \AA}^{-1}$ usually depends on the length of the alkyl chain and is connected with cooperative effects between polar groups of the same sign. These features can be found in the diffraction spectrum of [BuPy][Tf₂N] as well (Fig. 7.1). Consequently, the discussed correlations in structure either on the nanometer length scale or between the nearest neighbours will be reflected in dynamics of the studied IL and in its QENS spectra as a coherent component, which cannot be neglected.

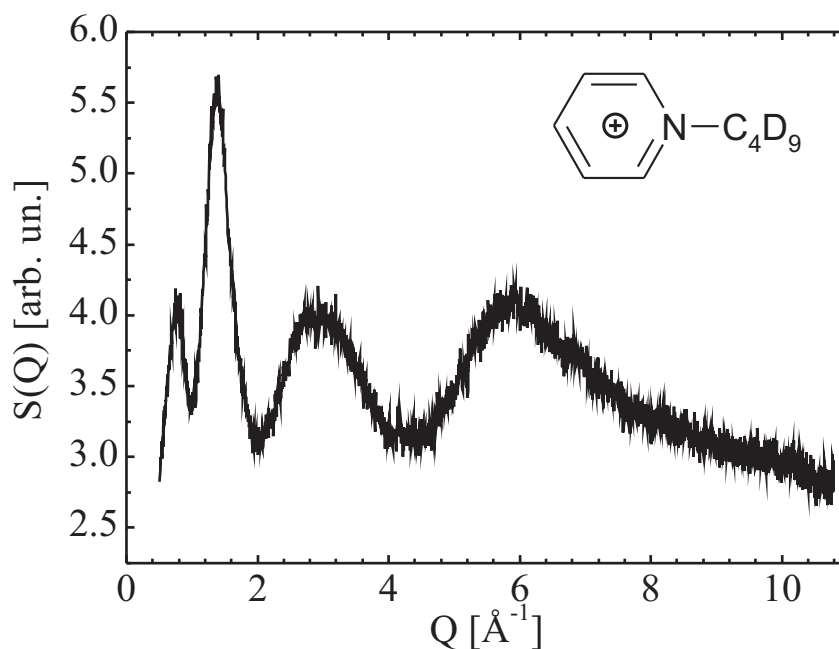


Figure 7.1. Intensity as a function of Q as measured on a completely deuterated sample, $[\text{Bu}_D\text{Py}_D][\text{Tf}_2\text{N}]$. The experiment was performed on the thermal neutron diffractometer HRPT at SINQ, using incident neutrons with $\lambda=1.5 \text{ \AA}$

For this reason the experiment on separation of coherent and spin-incoherent scattering of $[\text{BuPy}][\text{Tf}_2\text{N}]$ was conducted on D7 at ILL (see Chapter 3.2.2). The aim of the investigation was twofold. First, the obtained “pure” incoherent spectra would give access to the values of the time and length characteristics that are closer to the actual values and would allow to estimate a systematic error, to which measurements are prone, if one assumes that coherent scattering is negligible and the total scattering is incoherent in nature. Second, the coherent contribution is by no means a waste in this kind of experiment. It also provides information about dynamical processes of particles with regard to their surroundings. Therefore, analysis of the coherent component of the spectra was performed in the second part of this chapter.

7.1. Incoherent contribution

Following the method described in Chapter 3.2.2, the coherent and spin-incoherent contributions of the total scattering from the $[\text{BuPy}][\text{Tf}_2\text{N}]$ sample at four different temperatures were separated. The 2D intensity maps after data reduction are presented in Figure 7.2(a). For illustration the integrated intensity as a function of Q and a constant Q -cut are added as well. From the plot of the integrated intensity (Fig. 7.2(b)) we see that the incoherent component decreases gradually with wave number transfer in accordance with energy

redistribution due to the high frequency vibrations (Debye Waller factor). The coherent integrated intensity follows the structure factor measured on the totally deuterated sample (Fig. 7.1). Figure 7.2(c) demonstrates the spectrum of the Q -group at $Q=1.3 \text{ \AA}^{-1}$, where the coherent scattering is very strong with respect to the incoherent part.

Once the contributions had been separated, the analysis of both the incoherent and total spectra were performed. At first, a model independent fit was applied in order to explore how the systematic error connected with coherent scattering affects the time and length characteristics of the studied processes. The previous study (see Chapter 2.3, 5.2) showed that the incoherent scattering law for the total scattering in the quasielastic region can be considered as a convolution of the global and localized parts. The same was assumed for the “pure” incoherent spectra.

The linewidths attributed to the long-range diffusion were found to be prone to larger values than those of the total spectra and effected most of all (Fig. 7.3). If the input spectra are not corrected for the coherent scattering, the corresponding function has even a kind of modulation following the structure factor; the linewidth $\Gamma_{\text{glob}}(Q)$ is clearly narrower than that of the incoherent spectra at $Q=1.3 \text{ \AA}^{-1}$. These modulations are even more pronounced for the totally deuterated sample studied in the recent work [125], when the coherent scattering dominates. This phenomenon, often referred to as “de Gennes narrowing”, may be considered as a structural relaxation with longer lifetimes and was observed for some other systems [193, 194].

Unlike the totally deuterated sample, for which the presence of the dominating coherent scattering is not reflected in the linewidth of the spatially restricted dynamics, the separation of the contributions led to broadening of $\Gamma_{\text{loc}}(Q)$. As the diffusion coefficients are evaluated from the $\Gamma(Q)$ dependencies, it means that a systematic error will be encountered in estimated time characteristics, the diffusion coefficients tending to lower values than the actual ones. On the other hand, the EISF, which contains the information about the geometry of the localized motion, remains almost unaffected; it means that spatial parameters of the system may be estimated quite well only from spectra with unseparated components.

For the analysis of the incoherent spectra the jump-diffusion model (Eq. 2.24) for the long-range process and the Gaussian model (Eq. 2.41) with one radius of confinement for the localized dynamics were employed, so that the scattering law reads:

$$S_{\text{inc}}(Q, E) = I_0^{\text{inc}}(Q) \cdot \frac{1}{\pi} \frac{\Gamma_{\text{glob}}}{\Gamma_{\text{glob}}^2 + E^2} \otimes S_{\text{G}}(Q, E; D_{\text{loc}}) \otimes R(Q, E) + a + bE \quad (7.1)$$

The fact that only one characteristic size is necessary to capture the broader quasielastic contribution is explained by a coarser resolution function of the D7 spectrometer (FWHM

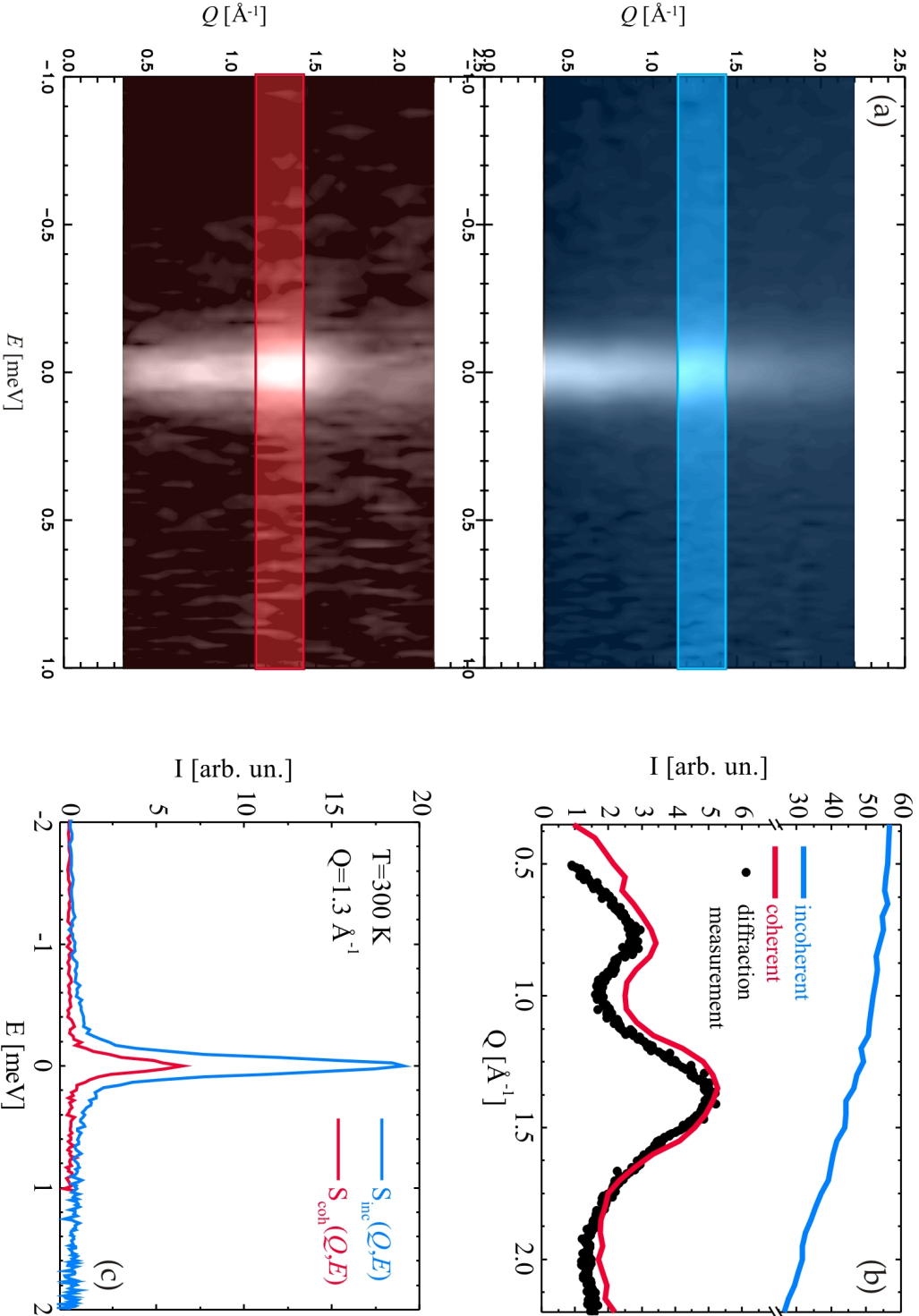


Figure 7.2. *Panel (a):* Intensity maps of the incoherent (blue) and coherent (red) contributions of [BuPy][Tf₂N]. *Panel (b):* Integrated intensity over the $[-2.0; 2.0]$ meV energy range as a function of Q . *Panel (c):* Constant Q -cut taken through the measured spectra of the incoherent and coherent components (a) at $Q=1.3 \text{ \AA}^{-1}$.

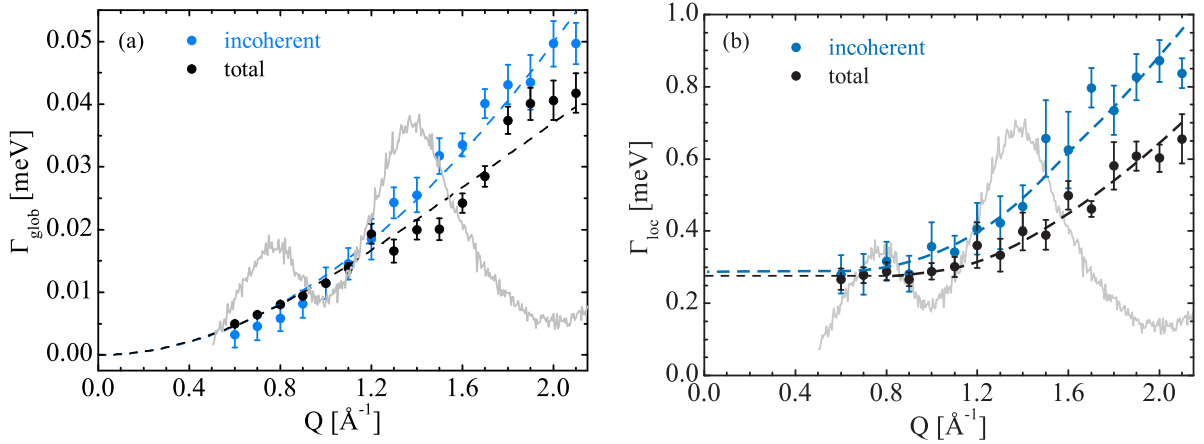


Figure 7.3. Q -dependences of the linewidth characterising the global (a) and localized (b) dynamics of [BuPy][Tf₂N] and evaluated from the incoherent part of the spectrum as well as from the total spectrum at $T=300$ K. The grey solid line is the diffraction spectrum measured on the completely deuterated sample

= $140 \mu\text{eV}$) than that of FOCUS ($\lambda = 5.75 \text{ \AA}$, $\text{FWHM}=60 \mu\text{eV}$) and, hence, by a shorter observation time. The results of the fitting procedure are included in Table 7.1.

The diffusion coefficients of the long-range motion and localized motion differ by a factor of five and their temperature dependence is consistent with the Arrhenius law (Eq. 5.4). The activation energy values equal 12.3 and 8.2 kJ/mol for the global and local processes, respectively, and are in agreement with the values calculated from the FOCUS spectra (Table 5.6). The radius of confinement, in which particles are moving, increases with temperature increase as well. The same calculations were performed for the spectra with unseparated contributions. The difference in the equivalent values of the diffusion coefficients amounts to 10-20%, of the radii $\sim 1\%$. So, as already discussed, the coherent contribution affects time characteristics first of all and, in this respect, should not be neglected.

Table 7.1. Diffusion coefficients of the global, D , and localized diffusion, D_{loc} , characteristic radii of confinement σ and residence time τ_0 as obtained from the incoherent spectra of the [BuPy] sample with Eq. 7.1 at different temperatures

T , K	$D \cdot 10^{-10}$, m^2/s	τ_0 , ps	$D_{\text{loc}} \cdot 10^{-10}$, m^2/s	σ , \AA
300.0	2.44 ± 0.03	7.3 ± 0.4	9.34 ± 0.05	0.416 ± 0.003
320.0	3.21 ± 0.04	5.9 ± 0.3	10.7 ± 0.07	0.492 ± 0.003
340.0	4.73 ± 0.04	5.7 ± 0.3	14.1 ± 0.07	0.567 ± 0.003
360.0	5.51 ± 0.04	4.6 ± 0.3	15.7 ± 0.08	0.636 ± 0.004

7.2. Coherent contribution

Although the coherent contribution is a source of valuable information, because it provides insight into collective processes and interference effects, the number of works on coherent quasielastic scattering is small. Moreover, for the objects of the investigations only diffusion processes were of relevance, concerning the time and length scale of QENS [193, 195, 196]. The number of analytical models, which are applicable for localized dynamics, is even much more limited [197]. Of course, all these examples are far from an ionic liquid, but some common approaches can be applied as a rough approximation to analyse the data.

Vineyard studied the relationship between the coherent and incoherent quasielastic component in the static approximation [198]. He started with the assumption that the time-displaced pair distribution function can be expressed by the self part of the function and the radial-distribution function $g(\mathbf{r}')$:

$$G(\mathbf{r}, t) \cong G_s(\mathbf{r}, t) + \int g(\mathbf{r}') G_s(\mathbf{r} - \mathbf{r}', t) d\mathbf{r}' \quad (7.2)$$

This led him to a simple formula, which connects the coherent and incoherent contributions of a diffusion process. The linewidth should be the same as for the incoherent contribution, only intensity is modulated:

$$S_{\text{coh}}(Q, E) = S_{\text{inc}}(Q, E) S(Q) \quad (7.3)$$

where $S(Q)$ is the static structure factor. Eq. 7.3 does not fulfil the second moment sum rule [85], so it is necessary to keep in mind that it is only a rough approximation.

However, it turned out that Eq. 7.1 is not the best choice to fit the coherent part of the spectra. The profile of the quasielastic broadening is simpler and can be presented by a single Lorentzian. The linewidths of the Lorentzian curves are close to the values obtained for the long-range diffusion from the incoherent contribution. Therefore, for the further data evaluation the following function was used in the fitting routine:

$$S_{\text{coh}}(Q, E) = I_0^{\text{coh}}(Q) \cdot \frac{1}{\pi} \frac{\Gamma_{\text{glob}}}{\Gamma_{\text{glob}}^2 + E^2} \otimes R(Q, E) + a + bE \quad (7.4)$$

where Γ_{glob} is expressed by Eq. 2.24 in terms of the jump diffusion model, $I_0^{\text{coh}}(Q)$ is the intensity factor of the coherent contribution.

Figure 7.4 shows two Q -dependences of the Lorentzian linewidth at two different temperatures with the function (Eq. 2.24), which fits to the experimental points satisfactorily well. The shortcoming of this approach, however, is that the diffusion coefficients are different from those obtained from the incoherent contribution (Fig. 7.5) and the modulation

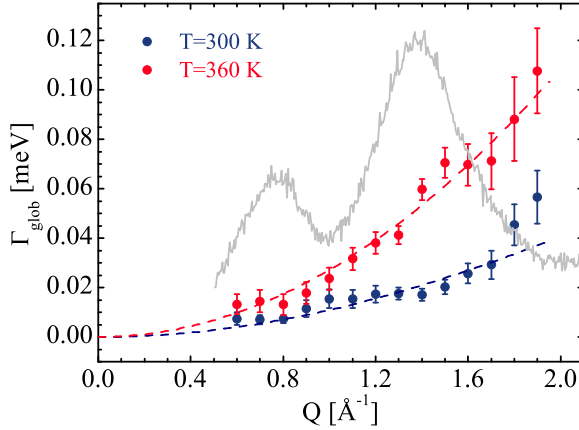


Figure 7.4. Q -dependence of the coherent quasielastic broadening at different temperatures. The grey solid line is the diffraction spectrum measured on the completely deuterated sample

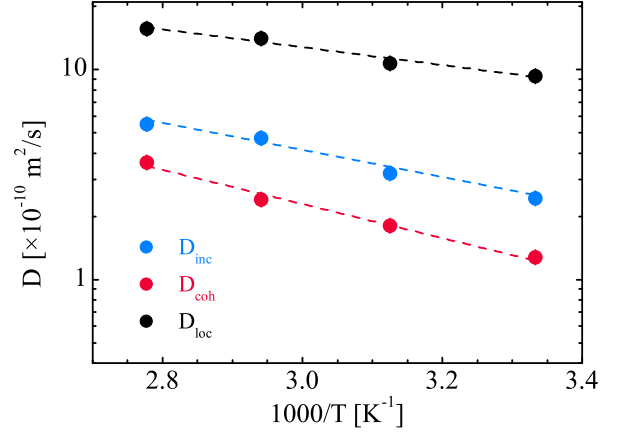


Figure 7.5. Arrhenius plots of the diffusion coefficients characterizing the long-range, D_{coh} and D_{coh} , and spatially restricted diffusion, D_{loc} .

of the linewidth is still observed at the Q -values corresponding to the maxima of the static structure factor. Even if the difference between the values of the diffusion coefficients could be explained by the fact that the source of the coherent scattering is not only the cation but the anion as well, the modulation of the linewidths remains a problem. Vineyard’s approximation does not explain “de Gennes narrowing” and, therefore, was criticized.

The Sköld’s ansatz can be employed as the next approximation in describing the coherent part [193, 199]:

$$S_{\text{coh}}(Q, E) = S_{\text{inc}} \left(\frac{Q}{\sqrt{S(Q)}}, E \right) S(Q) \quad (7.5)$$

The substitution of Q by $Q/\sqrt{S(Q)}$ introduced by Sköld helps to overcome the problem with the violation of the second moments sum rule. The same result was obtained by Leitner and Vogl [200] in their work, where they considered the diffusion of interacting particles on a Bravais lattice in the limit of weak or short-order interactions. Qualitatively this substitution may be understood in the following way [199]. The coherently scattered intensity is composed of the scattering from several atoms, $S(Q)$ being the measure of the effective number of atoms which contribute to the intensity at wave vector Q . The recoil energy transferred to the system is therefore $S(Q)$ times less, the same as if the recoiling mass were $S(Q)$ times greater. Unfortunately, the actual static structure factor of the studied IL has not been measured. But the intensity factor $I_0^{\text{coh}}(Q)$ is definitely connected with this characteristic and, in the first approximation, may be considered to be proportional to $S(Q)$. So one more parameter, the proportionality constant α , was introduced in the fit model. It

equals $I_0^{\text{coh}}(Q)$ at those Q -points where $S(Q) = 1$. The dynamic structure factor reads then:

$$S_{\text{coh}}(Q, E) = I_0^{\text{coh}}(Q) \cdot \frac{1}{\pi} \frac{\Gamma'_{\text{glob}}}{\Gamma_{\text{glob}}^2 + E^2} \otimes R(Q, E) + a + bE \quad (7.6)$$

where Γ'_{glob} is the linewidth of the diffusional process modified according to Eq. 7.5:

$$\Gamma'_{\text{glob}} = \frac{\hbar D_{\text{coh}} Q^2 \frac{\alpha}{I_0^{\text{coh}}(Q)}}{1 + D_{\text{coh}} Q^2 \frac{\alpha}{I_0^{\text{coh}}(Q)} \tau_0} \quad (7.7)$$

The fitting routine with Eq. 7.6–7.7 was carried out at temperature $T=300$ K, because quite a noisy signal at elevated temperatures rendered the procedure unstable. The estimated value of α and the intensity factor as a function of Q are shown in Figure 7.6. At the same time the diffusion coefficient reached the corresponding value of the incoherent contribution. So it is a good sign, but the absence of reliable results at the other temperatures does not allow us to completely approve the validity of this approach. Besides, it definitely helps to overcome the difficulties with the modulations of the linewidth and decrease the discrepancy between the diffusion coefficients obtained from the coherent and incoherent parts.

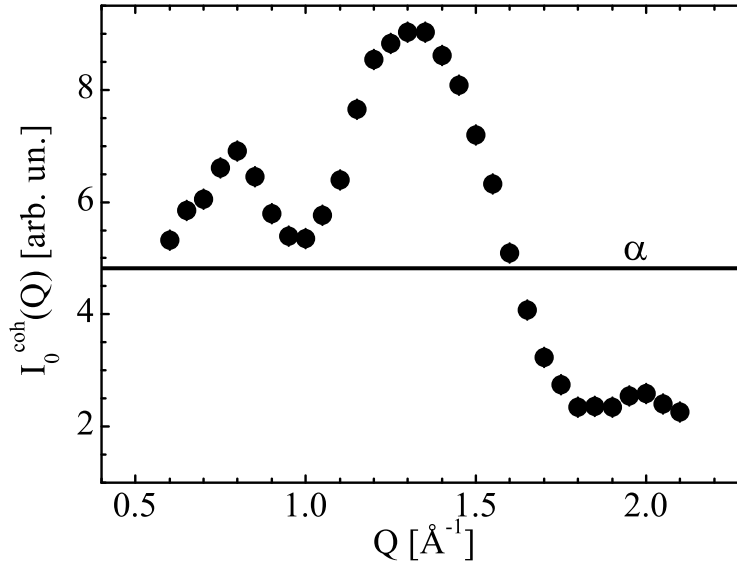


Figure 7.6. Intensity factor $I_0^{\text{coh}}(Q)$ and α derived for the coherent component of the spectrum at $T=300$ K according to Eq. 7.6–7.7

7.3. Summary

To sum up, the first slower process detected for [BuPy][Tf₂N] is diffusive in nature, the linewidth of this process can be well described by the jump diffusion model. This process shows up both in the coherent and incoherent contribution, so it is at least partially of

collective nature. At Q -values where there are the maxima of the static structure factor the modulation of the linewidth is observed. Indeed, maxima of $S(Q)$ imply that the particles prefer to build local arrangements, in which the correlated motion of neighbouring particles is energetically favoured. It takes more energy to break such arrangements up and hence they are longer-lived. Collective translational and rotational motion was also described in the work by Schröder [201], where he studied the dielectric behaviour of a imidazolium-based IL.

The second faster process is not affected by the structure and cannot be extracted from the coherent contribution; so, chain librations and their conformational changes, associated with this process are a true single particle process on a shorter time scale.

8. General conclusions and outlook

Knowledge about dynamical processes is a key to better understanding many fascinating properties of ILs and, hence, important for their manifold potential future applications. In this thesis cation dynamics in ILs have been investigated by means of QENS, primarily using the time-of-flight technique. In particular, the representatives of two classes were studied: pyridinium-based ILs and alkylammonium-based protic ILs. Although the studied samples were mainly used in this work as model compounds, the evaluated data on their diffusivity is of interest for the application fields, where they have been already tested.

For the description of the QENS-spectra of the studied ILs on the nanosecond-picosecond time scale analytical forms of the scattering laws have been worked out on the basis of simpler and well-known theoretical models. The tested equations gave reasonable results in a broad temperature range and can be generalized for a larger group of ILs. However, owing to diverse processes occurring in the ILs, the models are characterized by a sufficiently great number of free parameters. To make the fitting routine more stable and unambiguous data evaluation feasible, the more stringent 2D-fitting approach was applied in this thesis. Both the energy and the wavevector transfer, the quantities which provide information about time and spatial characteristics of the processes, respectively, were treated as independent variables. It allows fitting to more complicated analytical expressions than the conventional approach, when parameters are evaluated for every Q -group independently. The corresponding program module with user-interface was written to fulfil the requirements of QENS-data analysis.

Different aspects of the cation dynamics in ILs have been studied in the present work. The major achievements are highlighted as follows. In the low temperature range one process mainly influences the spectra. This is the thermally activated rotation of the end methyl groups. At elevated temperatures for all the studied compounds two major processes have been generally established on picosecond time scale: long-range diffusion, which can be described in terms of the jump-diffusion model, and more tangled localized motions. In contrast to other experimental methods (in particular PFG-NMR), due to shorter times probed, the temperature dependences of the diffusion coefficients were found to obey Arrhenius' law. For

the characterization of the restricted dynamics several distribution functions were proposed, which account for different volume sizes accessible for the various groups of the hydrogen atoms in the cations and, hence, allow for the flexibility of the alkyl substituents.

To unravel complex localized motions intrinsic to the different parts of the cation (torsional rotations, libration of the whole chain, methyl group rotations, out-of-plane libration of the pyridinium ring), the benefit of deuterium labelling was used. Thus, in the case of the pyridinium-based ILs two partially deuterated samples of [BuPy][Tf₂N] were investigated: either the butyl chain of the cation [Bu_DPy][Tf₂N] or the pyridinium ring [BuPy_D][Tf₂N] were deuterated. The results of the analysis have shown, that the confined motion of the flexible alkyl chain, as well as the pyridinium ring gives rise to the broadening of the elastic line, observed from the totally protonated sample. The evaluated numerical values of the spatial characteristics point to the motions restricted by the cation geometry, but not to the global rotation inside the cage formed by the neighbouring ions.

A broader dynamic range was covered by using spectrometers with tuneable resolution functions. While changing the experimental observation time, it was possible to focus either on the long-range translational motion, which was seen as a single Lorentzian for the usually applied instrument setting, or on very fast processes, presented by the flat background in the used fit models. This information is even more precious, because it was acquired for the partially deuterated samples, which made the independent analysis of the different groups of atoms possible. As a result, different relaxation behaviour was detected in the intermediate time range (several picoseconds) for the butyl chain and the pyridinium ring. However, our data is yet limited to one set measured at one temperature. For a more thorough investigation these experiments should be performed for various temperatures (close to the melting point, below and above, for both the liquid and solid/amorphous state).

Partial deuteration was applied in the case of the protic IL TEA-TF as well. The side ethyl chains of the cation were excluded from the consideration by substituting hydrogen atoms with deuterium atoms; only one proton, which allows anhydrous conductivity, was left and used as a tagged particle to trace the global dynamics of the cation. From the comparison of the linewidths related to the long-range diffusion of both the protonated and partially deuterated samples no long-distance hops of the proton have been detected. On the other hand, the N-H proton exhibits enhanced localized dynamics on a length scale of ~ 1 Å and on a time scale of ~ 4 ps, which might be connected with the proton exchange between the cation and the adjacent anion.

Experimental separation of coherent and spin-incoherent scattering, which gives insight into collective and single-particle dynamics, respectively, has been performed for the pyridinium based IL [BuPy][Tf₂N]. This is, to our knowledge, the first experiment of this kind

on ILs. It showed that the localized motions of the butyl chain and the pyridinium ring are true single-particle processes in nature; whereas the long-range dynamics are affected by the structure of the ionic liquid. The correlations between neighbouring ions slow down the diffusion, until these local arrangements are broken up.

QENS experiments with the polarization analysis are very promising in the case of partially deuterated samples as well. Allowing the investigation of distinct groups of hydrogen atoms, partial deuteration of the samples leads to the more intense coherent contribution at the same time. Then, on one hand, separation of the coherent and spin-incoherent components would provide means to study the pure single-particle dynamics of the separate groups of the cation, and on the other hand, it would allow obtaining spectra of the coherent dynamic structure factor, characterized by better statistics in the case of deuterated samples. In general a more systematic QENS study with polarized neutrons is required for the future.

As the next step, it would be important to incorporate the support of MD simulations into the study of ILs by means of neutron scattering. This would give a direct access to the dynamic structure factor in the same (Q, E) -range covered in the QENS method. The computed quantities could be then compared with the experimentally obtained ones. Moreover, for the interpretation of the coherent contribution it would be even more crucial, as there are very few analytical models describing it.

As for the data reduction step, multiple scattering correction of raw spectra could be undertaken for a more sophisticated data analysis and more precise evaluation of parameters.

References

- [1] B. Kirchner, editor. *Ionic liquids*, volume 290. Springer, 2010.
- [2] J. P. Hallett and T. Welton. Room-temperature ionic liquids: solvents for synthesis and catalysis. 2. *Chemical Reviews*, 111(5):3508–3576, 2011.
- [3] N. V. Plechkova and K. R. Seddon. Applications of ionic liquids in the chemical industry. *Chemical Society Reviews*, 37(1):123–150, 2008.
- [4] Ionic Liquids Database- (ILThermo) NIST standard reference database. <http://ilthermo.boulder.nist.gov/ILThermo/mainmenu.uix>, July 2013.
- [5] W. Schröer. A short history of phase transitions in ionic fluids. *Contributions to Plasma Physics*, 52(1):78–88, 2012.
- [6] C. P. Fredlake, J. M. Crosthwaite, D. G. Hert, S. N. V. K. Aki, and J. F. Brennecke. Thermophysical properties of imidazolium-based ionic liquids. *The Journal of Chemical & Engineering Data*, 49(4):954–964, 2004.
- [7] S. I. Fletcher, F. B. Sillars, N. E. Hudson, and P. J. Hall. Physical properties of selected ionic liquids for use as electrolytes and other industrial applications. *The Journal of Chemical & Engineering Data*, 55(2):778–782, 2010.
- [8] J. N. A. Canongia Lopes and A. A. H. Pádua. Nanostructural organization in ionic liquids. *The Journal of Physical Chemistry B*, 110(7):3330–3335, 2006.
- [9] D. Xiao, L. G. Hines, S. Li, R. A. Bartsch, E. L. Quitevis, O. Russina, and A. Triolo. Effect of cation symmetry and alkyl chain length on the structure and intermolecular dynamics of 1,3-dialkylimidazolium bis(trifluoromethanesulfonyl)amide ionic liquids. *The Journal of Physical Chemistry B*, 113(18):6426–6433, 2009.
- [10] M. Khamooshi, K. Parham, and U. Atikol. Overview of ionic liquids used as working fluids in absorption cycles. *Advances in Mechanical Engineering*, 2013:620592, 2013.
- [11] R. N. Das and K. Roy. Advances in QSPR/QSTR models of ionic liquids for the design of greener solvents of the future. *Molecular Diversity*, 17(1):151–196, 2013.

- [12] H. Li, P. S. Bhadury, B. Song, and S. Yang. Immobilized functional ionic liquids: efficient, green, and reusable catalysts. *RSC Advances*, 2(33):12525–12551, 2012.
- [13] C. Yue, D. Fang, L. Liu, and T.-F. Yia. Synthesis and application of task-specific ionic liquids used as catalysts and/or solvents in organic unit reactions. *Journal of Molecular Liquids*, 163(3):99–121, 2011.
- [14] H. Olivier-Bourbigou, L. Magna, and D. Morvan. Ionic liquids and catalysis: Recent progress from knowledge to applications. *Applied Catalysis A: General*, 373(1–2):1–56, 2010.
- [15] M. Palacio and B. Bhushan. A review of ionic liquids for green molecular lubrication in nanotechnology. *Tribology Letters*, 40(2):247–268, 2010.
- [16] H. Zhao. Innovative applications of ionic liquids as "green" engineering liquids. *Chemical Engineering Communications*, 193(12):1660–1677, 2006.
- [17] E. Reichert, R. Wintringer, D. A. Volmer, and R. Hempelmann. Electro-catalytic oxidative cleavage of lignin in a protic ionic liquid. *Physical Chemistry Chemical Physics*, 14(15):5214–5221, 2012.
- [18] C.-Z. Liu, F. Wang, A. R. Stiles, and C. Guo. Ionic liquids for biofuel production: Opportunities and challenges. *Applied Energy*, 92:406–414, 2012.
- [19] F. Karadas, B. Köz, J. Jacquemin, E. Deniz, D. Rooney, J. Thompson, C. T. Yavuz, M. Khraisheh, S. Aparicio, and M. Atihan. High pressure CO₂ absorption studies on imidazolium-based ionic liquids: Experimental and simulation approaches. *Fluid Phase Equilibria*, 351:74–86, 2013.
- [20] V. V. Chaban and O. V. Prezhdo. Ionic and molecular liquids: Working together for robust engineering. *The Journal of Physical Chemistry Letters*, 4(9):1423–1431, 2013.
- [21] H. Ohno, editor. *Electrochemical Aspects of Ionic Liquids*. John Wiley & Sons, Inc., Hoboken, New Jersey., 2005.
- [22] D. Wei. Dye sensitized solar cells. *International Journal of Molecular Sciences*, 11(3):1103–1113, 2010.
- [23] K. Takagi, S. Magaino, H. Saito, T. Aoki, and D. Aoki. Measurements and evaluation of dye-sensitized solar cell performance. *Journal of Photochemistry and Photobiology C: Photochemistry Reviews*, 14:1–12, 2013.
- [24] C. Pinilla, M. G. Del Popolo, R. M. Lynden-Bell, and J. Kohanoff. Structure and dynamics of a confined ionic liquid. Topics of relevance to dye-sensitized solar cells. *The Journal of Physical Chemistry B*, 109(38):17922–17927, 2005.
- [25] U. A. Rana, M. Forsyth, D. R. MacFarlane, and J. M. Pringle. Toward protic ionic liquid and organic ionic plastic crystal electrolytes for fuel cells. *Electrochimica Acta*, 84:213–222,

- 2012.
- [26] G. Saito and Y. Yoshida. Frontiers of organic conductors and superconductors. *Unimolecular and Supramolecular Electronics I. Topics in Current Chemistry*, 312:67–126, 2012.
- [27] A. Lewandowski and A. Swiderska-Mocek. Ionic liquids as electrolytes for Li-ion batteries an overview of electrochemical studies. *Journal of Power Sources*, 194(2):601–609, 2009.
- [28] L. T. Costa and M. C. C. Ribeiro. Molecular dynamics simulation of polymer electrolytes based on poly(ethylene oxide) and ionic liquids. I. Structural properties. *The Journal of Chemical Physics*, 124(18):184902, 2006.
- [29] L. T. Costa and M. C. C. Ribeiro. Molecular dynamics simulation of polymer electrolytes based on poly(ethylene oxide) and ionic liquids. II. Dynamical properties. *The Journal of Chemical Physics*, 127(16):164901, 2007.
- [30] M. Galinski, A. Lewandowski, and I. Stepniak. Ionic liquids as electrolytes. *Electrochimica Acta*, 51(26):5567–5580, 2006.
- [31] T. Fujimoto and K. Awaga. Electric-double-layer field-effect transistors with ionic liquids. *Physical Chemistry Chemical Physics*, 15(23):8983–9006, 2013.
- [32] D. Wei and A. Ivaska. Applications of ionic liquids in electrochemical sensors. *Analytica Chimica Acta*, 607(2):126–135, 2008.
- [33] D. S. Silvester. Recent advances in the use of ionic liquids for electrochemical sensing. *Analyst*, 136:4871–4882, 2011.
- [34] W. Simka, D. Puszczuk, and G. Nawrat. Electrodeposition of metals from non-aqueous solutions. *Electrochimica Acta*, 54(23):5307–5319, 2009.
- [35] A. Garcia-Saiz, I. de Pedro, J. A. Blanco, J. Gonzalez, and J. R. Fernandez. Pressure effects on emim[FeCl₄], a magnetic ionic liquid with three-dimensional magnetic ordering. *The Journal of Physical Chemistry B*, 117(11):3198–3206, 2013.
- [36] E. Sloutskin, R. M. Lynden-Bell, S. Balasubramanian, and M. Deutsch. The surface structure of ionic liquids: Comparing simulations with x-ray measurements. *The Journal of Chemical Physics*, 125(17):174715, 2006.
- [37] B. L. Bhargava and S. Balasubramanian. Insights into the structure and dynamics of a room-temperature ionic liquid: Ab initio molecular dynamics simulation studies of 1-*n*-butyl-3-methylimidazolium hexafluorophosphate ([bmim][PF₆]) and the [bmim][PF₆]-CO₂ mixture. *The Journal of Physical Chemistry B*, 111(17):4477–4487, 2007.
- [38] C. Spickermann, J. Thar, S. B. C. Lehmann, S. Zahn, J. Hunger, R. Buchner, P. A. Hunt, T. Welton, and B. Kirchner. Why are ionic liquid ions mainly associated in water? A Car-Parrinello study of 1-ethyl-3-methyl-imidazolium chloride water mixture. *The Journal of*

- Chemical Physics*, 129(10):104505, 2008.
- [39] M. H. Kowsari, S. Alavi, M. Ashrafizaadeh, and B. Najafi. Molecular dynamics study of congruent melting of the equimolar ionic liquid-benzene inclusion crystal [emim][NTf₂]C₆H₆. *The Journal of Chemical Physics*, 132(4):044507, 2010.
- [40] T. Yan, S. Li, W. Jiang, X. Gao, B. Xiang, and G. A. Voth. Structure of the liquid–vacuum interface of room-temperature ionic liquids: A molecular dynamics study. *The Journal of Physical Chemistry B*, 110(4):1800–1806, 2006.
- [41] S. Zahn, J. Thar, and B. Kirchner. Structure and dynamics of the protic ionic liquid monomethylammonium nitrate ([CH₃NH₃][NO₃]) from ab initio molecular dynamics simulations. *The Journal of Chemical Physics*, 132(12):124506, 2010.
- [42] L. Gontrani, O. Russina, F. Lo Celso, R. Caminiti, G. Annat, and A. Triolo. Liquid structure of trihexyltetradecylphosphonium chloride at ambient temperature: An x-ray scattering and simulation study. *The Journal of Physical Chemistry B*, 113(27):9235–9240, 2009.
- [43] Y. Wang. Disorder and reordering of ionic liquids under an external electric field. *The Journal of Physical Chemistry B*, 113(32):11058–11060, 2009.
- [44] K. Fujii, Y. Soejima, Y. Kyoshoin, S. Fukuda, R. Kanzaki, Y. Umebayashi, T. Yamaguchi, S.-i. Ishiguro, and T. Takamuku. Liquid structure of room-temperature ionic liquid, 1-ethyl-3-methylimidazolium bis-(trifluoromethanesulfonyl) imide. *The Journal of Physical Chemistry B*, 112:4329–4336, 2008.
- [45] D. Bedrov, O. Borodin, Z. Li, and G. D. Smith. Influence of polarization on structural, thermodynamic, and dynamic properties of ionic liquids obtained from molecular dynamics simulations. *The Journal of Physical Chemistry B*, 114(15):4984–4997, 2010.
- [46] M. H. Ghatee and Y. Ansari. Ab initio molecular dynamics simulation of ionic liquids. *The Journal of Chemical Physics*, 126(15):154502, 2007.
- [47] H. K. Kashyap, C. S. Santos, H. V. R. Annapureddy, N. S. Murthy, C. J. Margulis, and E. W. Castner. Temperature-dependent structure of ionic liquids: X-ray scattering and simulations. *Faraday Discussions*, 154:133–143, 2012.
- [48] H. V. Spohr and G. N. Patey. Structural and dynamical properties of ionic liquids: The influence of charge location. *The Journal of Chemical Physics*, 130(10):104506, 2009.
- [49] S. M. Urahata and M. C. C. Ribeiro. Collective excitations in an ionic liquid. *The Journal of Chemical Physics*, 124(7):074513, 2006.
- [50] L. J. A. Siqueira and M. C. C. Ribeiro. Molecular dynamics simulation of the ionic liquid N-ethyl-N,N-dimethyl-N-(2-methoxyethyl)ammonium bis(trifluoromethanesulfonyl)imide. *The Journal of Physical Chemistry B*, 111(40):11776–11785, 2007.

- [51] M. H. Kowsari, S. Alavi, M. Ashrafizaadeh, and B. Najafi. Molecular dynamics simulation of imidazolium-based ionic liquids. I. Dynamics and diffusion coefficient. *The Journal of Chemical Physics*, 129(22):224508, 2008.
- [52] H. Liu and E. Maginn. A molecular dynamics investigation of the structural and dynamic properties of the ionic liquid 1-n-butyl-3-methylimidazolium bis(trifluoromethanesulfonyl)imide. *The Journal of Chemical Physics*, 135(12):124507, 2011.
- [53] S. M. Urahata and M. C. C. Ribeiro. Single particle dynamics in ionic liquids of 1-alkyl-3-methylimidazolium cations. *The Journal of Chemical Physics*, 122(2):024511, 2005.
- [54] Z. Hu and C. J. Margulis. Heterogeneity in a room-temperature ionic liquid: Persistent local environments and the red-edge effect. *Proceedings of the National Academy of Sciences of the United States of America*, 103(4):831–836, 2006.
- [55] S. S. Sarangi, W. Zhao, F. Müller-Plathe, and S. Balasubramanian. Correlation between dynamic heterogeneity and local structure in a room-temperature ionic liquid: A molecular dynamics study of [bmim][PF₆]. *A European Journal of Chemical Physics and Physical Chemistry*, 11(9):2001–2010, 2010.
- [56] J. Habasaki and K. L. Ngai. Heterogeneous dynamics of ionic liquids from molecular dynamics simulations. *The Journal of Chemical Physics*, 129(19):194501, 2008.
- [57] M. G. Del Popolo and G. A. Voth. On the structure and dynamics of ionic liquids. *The Journal of Physical Chemistry B*, 108(5):17441752, 2004.
- [58] W. Kob. Supercooled liquids, the glass transition, and computer simulations. *e-print arXiv:cond-mat/0212344v1*, 2002.
- [59] F. Dommert, K. Wendler, R. Berger, L. Delle Site, and C. Holm. Force fields for studying the structure and dynamics of ionic liquids: A critical review of recent developments. *A European Journal of Chemical Physics and Physical Chemistry*, 13(7):1625–1637, 2012.
- [60] T. Köddermann, D. Paschek, and R. Ludwig. Molecular dynamic simulations of ionic liquids: A reliable description of structure, thermodynamics and dynamics. *A European Journal of Chemical Physics and Physical Chemistry*, 8(17):2464–2470, 2007.
- [61] B. Kirchner, P. J. di Dio, and J. Hutter. Real-world predictions from ab initio molecular dynamics simulations. *Topics in Current Chemistry*, 307:109–153, 2012.
- [62] E. W. Castner and J. F. Wishart. Spotlight on ionic liquids. *The Journal of Chemical Physics*, 132(12):120901, 2010.
- [63] H. Weingärtner. Understanding ionic liquids at the molecular level: Facts, problems, and controversies. *Angewandte Chemie*, 47(4):654–670, 2008.
- [64] J. Wuttke, I. Chang, O. G. Randl, F. Fujara, and W. Petry. Tagged-particle motion in viscous

- glycerol: Diffusion-relaxation crossover. *Physical Review E: Statistical, Nonlinear, and Soft Matter Physics*, 54(5):5364–5369, 1996.
- [65] H. Weingärtner. NMR studies of ionic liquids: Structure and dynamics. *Current Opinion in Colloid & Interface Science*, 18(3):183–189, 2013.
- [66] H. Tokuda, K. Hayamizu, K. Ishii, Md. Abu Bin Hasan Susan, and M. Watanabe. Physicochemical properties and structures of room temperature ionic liquids. 2. Variation of alkyl chain length in imidazolium cation. *The Journal of Physical Chemistry B*, 109(13):6103–6110, 2005.
- [67] A. Filippov, F. U. Shah, M. Taher, S. Glavatskih, and O. N. Antzutkin. NMR self-diffusion study of a phosphonium bis(mandelato)borate ionic liquid. *Physical Chemistry Chemical Physics*, 15(23):9281–9287, 2013.
- [68] S. Pandey, S. N. Baker, S. Pandey, and G. A. Baker. Fluorescent probe studies of polarity and solvation within room temperature ionic liquids: A review. *Journal of Fluorescence*, 22(5):1313–1343, 2012.
- [69] D. Xiao, J. R. Rajian, A. Cady, S. Li, R. A. Bartsch, and E. L. Quitevis. Nanostructural organization and anion effects on the temperature dependence of the optical Kerr effect spectra of ionic liquids. *The Journal of Physical Chemistry B*, 111(18):4669–4677, 2007.
- [70] D. Xiao, J. R. Rajian, L. G. Hines, S. Li, R. A. Bartsch, and E. L. Quitevis. Nanostructural organization and anion effects in the optical Kerr effect spectra of binary ionic liquid mixtures. *The Journal of Physical Chemistry B*, 112(42):13316–13325, 2008.
- [71] G. Giraud, C. M. Gordon, I. R. Dunkin, and K. Wynne. The effects of anion and cation substitution on the ultrafast solvent dynamics of ionic liquids: A time-resolved optical Kerr-effect spectroscopic study. *The Journal of Chemical Physics*, 119(1):464–477, 2003.
- [72] D. A. Turton, J. Hunger, A. Stoppa, G. Hefter, A. Thoman, M. Walther, R. Buchner, and K. Wynne. Dynamics of imidazolium ionic liquids from a combined dielectric relaxation and optical Kerr effect study: Evidence for mesoscopic aggregation. *Journal of the American Chemical Society*, 131(31):11140–11146, 2009.
- [73] R. Hempelmann. *Quasielastic neutron scattering and solid state diffusion*. Oxford series on neutron scattering in condensed matter. Clarendon Press, Oxford, 2000.
- [74] J. Fitter, T. Gutberlet, and J. Katsaras, editors. *Neutron scattering in Biology*. Biological and Medical Physics, Biomedical Engineering. Springer, 2006.
- [75] V. G. Sakai and A. Arbe. Quasielastic neutron scattering in soft matter. *Current Opinion in Colloid & Interface Science*, 14:381–390, 2009.
- [76] E. Mamontov, H. Luo, and S. Dai. Proton dynamics in N,N,N',N'-tetramethylguanidinium

- bis(perfluoroethylsulfonyl)imide protic ionic liquid probed by quasielastic neutron scattering. *The Journal of Physical Chemistry B*, 113(1):159–169, 2009.
- [77] A. Triolo, O. Russina, V. Arrighi, F. Juranyi, S. Janssen, and C. M. Gordon. Quasielastic neutron scattering characterization of the relaxation processes in a room temperature ionic liquid. *The Journal of Chemical Physics*, 119(16):8549–8557, 2003.
- [78] J. De Roche, C. M. Gordon, C. T. Imrie, M. D. Ingram, A. R. Kennedy, F. Lo Celso, and A. Triolo. Application of complementary experimental techniques to characterization of the phase behavior of [C₁₆mim][PF₆] and [C₁₄mim][PF₆]. *Chemistry of Materials*, 15(16):3089–3097, 2003.
- [79] E. Mamontov, G. A. Baker, H. Luo, and S. Dai. Microscopic diffusion dynamics of silver complex-based room-temperature ionic liquids probed by quasielastic neutron scattering. *A European Journal of Chemical Physics and Physical Chemistry*, 12(5):944–950, 2011.
- [80] B. Aoun, M. A. González, J. Ollivier, M. Russina, Z. Izaola, D. L. Price, and M.-L. Saboungi. Translational and reorientational dynamics of an imidazolium-based ionic liquid. *The Journal of Physical Chemistry Letters*, 1(17):2503–2507, 2010.
- [81] B. Aoun, M. A. González, M. Russina, D. L. Price, and M.-L. Saboungi. Dynamics of butyl- and hexyl-methylimidazolium bromide ionic liquids. *Journal of the Physical Society of Japan*, 82(Suppl.A):SA002, 2013.
- [82] S. M. Chathoth, E. Mamontov, S. Dai, X. Wang, P. F. Fulvio, and D. J. Wesolowski. Fast diffusion in a room temperature ionic liquid confined in mesoporous carbon. *Europhysics Letters*, 97(6):66004, 2012.
- [83] S. M. Chathoth, E. Mamontov, P. F. Fulvio, X. Wang, G. A. Baker, S. Dai, and D. J. Wesolowski. An unusual slowdown of fast diffusion in a room temperature ionic liquid confined in mesoporous carbon. *Europhysics Letters*, 102(1):16004, 2013.
- [84] G. L. Squires. *Introduction to the theory of thermal neutron scattering*. Dover Publications Inc., New York, 1996.
- [85] S. W. Lovesey. *Theory of Neutron Scattering from Condensed Matter*. Number 72 in International Series of Monographs on Physics. Oxford University Press, USA, 1986.
- [86] G. Allen and J. S. Higgins. Physico-chemical aspects of neutron studies of molecular motion. *Reports on Progress in Physics*, 36:1073–1133, 1973.
- [87] M. Bée. Localized and long-range diffusion in condensed matter: state of the art of QENS studies and future prospects. *Chemical Physics*, 292(2–3):121–141, 2003.
- [88] S. U. Egelhaaf. Solution scattering. *Soft Condensed Matter Physics in Molecular and Cell Biology*, pages 275–310, 2006.

- [89] J. P. Embs, F. Juranyi, and R. Hempelmann. Introduction to quasielastic neutron scattering. *Zeitschrift für Physikalische Chemie*, 224(1–2):5–32, 2010.
- [90] L. Van Hove. Correlations in space and time and Born approximation scattering in systems of interacting particles. *Physical Review*, 95(1):249–262, 1954.
- [91] R. M. Moon, T. Riste, and W. C. Koehler. Polarization analysis of thermal-neutron scattering. *Physical Review*, 181(2):920–931, 1969.
- [92] J. R. Stewart, P. P. Deen, K. H. Andersen, H. Schober, J.-F. Barthélémy, J. M. Hillier, A. P. Murani, T. Hayes, and B. Lindenau. Disordered materials studied using neutron polarization analysis on the multi-detector spectrometer, D7. *Journal of Applied Crystallography*, 42(1):69–84, 2009.
- [93] O. Schärpf. The spin of the neutron as a measuring probe. `host-82-135-31-182.customer.m-online.net/neutronpol.pdf`, 2010.
- [94] M. Bastos, V. Castro, G. Mrevlishvili, and J. Teixeira. Hydration of ds-DNA and ss-DNA by neutron quasielastic scattering. *Biophysical Journal*, 86(6):3822–3827, 2004.
- [95] G. Gibrat, F. L. Assairi, Y. Blouquit, C. T. Craescu, and M.-C. Bellissent-Funel. Biophysical study of thermal denaturation of apo-calmodulin: Dynamics of native and unfolded states. *Biophysical Journal*, 95(11):5247–5256, 2008.
- [96] A.M. Stadler, I. Digel, G.M. Artmann, J.P. Embs, G. Zaccai, and G. Büldt. Hemoglobin dynamics in red blood cells: Correlation to body temperature. *Biophysical Journal*, 95(11):5449–5461, 2008.
- [97] A. M. Stadler, L. van Eijck, F. Demmel, and G. Artmann. Macromolecular dynamics in red blood cells investigated using neutron spectroscopy. *Journal of the Royal Society, Interface*, 8(57):590–600, 2011.
- [98] T. Unruh, C. Smuda, S. Busch, J. Neuhaus, and W. Petry. Diffusive motions in liquid medium-chain n-alkanes as seen by quasielastic time-of-flight neutron spectroscopy. *The Journal of Chemical Physics*, 129(12):121106, 2008.
- [99] C. Smuda, S. Busch, G. Gemmecker, and T. Unruh. Self-diffusion in molecular liquids: Medium-chain n-alkanes and coenzyme Q10 studied by quasielastic neutron scattering. *The Journal of Chemical Physics*, 129(1):014513, 2008.
- [100] V. K. Sharma, S. Mitra, G. Verma, P. A. Hassan, V. Garcia Sakai, and R. Mukhopadhyay. Internal dynamics in SDS micelles: Neutron scattering study. *The Journal of Physical Chemistry B*, 114(51):17049–17056, 2010.
- [101] S. Mitra, V. K. Sharma, V. Garcia Sakai, J. Peter Embs, and R. Mukhopadhyay. Molecular

- mobility in solid sodium dodecyl sulfate. *The Journal of Physical Chemistry B*, 115(32):9732–9738, 2011.
- [102] C. Smuda, G. Gemmecker, and Tobias Unruh. Quasielastic and inelastic neutron scattering study of methyl group rotation in solid and liquid pentafluoroanisole and pentafluorotoluene. *The Journal of Chemical Physics*, 128(19):194502, 2008.
- [103] J. T. Grissom and D. R. Koehler. Introduction to resolution distortion. *American Journal of Physics*, 35(8):753–760, 1967.
- [104] Y. Inamura, O. Yamamuro, S. Hayashi, and H. Hamaguchi. Dynamics structure of a room-temperature ionic liquid bmimCl. *Physica B: Condensed Matter*, 385–386(1):732–734, 2006.
- [105] S. Jahn, J. Ollivier, and F. Demmel. Fast ionic mobility in cryolite studied by quasielastic neutron scattering. *Solid State Ionics*, 179(35–36):1957–1961, 2008.
- [106] K. S. Singwi and A. Sjölander. Diffusive motions in water and cold neutron scattering. *Physical Review*, 119(3):863–871, 1960.
- [107] L. J. Smith, D. L. Price, Z. Chowdhuri, J. W. Brady, and M.-L. Saboungi. Molecular dynamics of glucose in solution: A quasielastic neutron scattering study. *The Journal of Chemical Physics*, 120(8):3527–3530, 2004.
- [108] M. L. Hoarfrost, M. Tyagi, R. A. Segalman, and J. A. Reimer. Proton hopping and long-range transport in the protic ionic liquid [Im][TFSI], probed by pulsed-field gradient NMR and quasi-elastic neutron scattering. *The Journal of Physical Chemistry B*, 116(28):8201–8209, 2012.
- [109] P. A. Egelstaff. *An Introduction to the Liquid State*. Academic Press, London and New York, 1967.
- [110] M. Bée. *Quasielastic Neutron Scattering, Principles and Applications in Solid State Chemistry, Biology and Materials Science*. Adam Hilger, Bristol, 1988.
- [111] A. J. Dianoux, F. Volino, and H. Hervet. Incoherent scattering law for neutron quasi-elastic scattering in liquid crystals. *Molecular Physics*, 30(4):1181–1194, 1975.
- [112] R. Zorn, B. Frick, and L. J. Fetters. Quasielastic neutron scattering study of the methyl group dynamics in polyisoprene. *The Journal of Chemical Physics*, 116(2):845–853, 2002.
- [113] B. Frick and L. J. Fetters. Methyl group dynamics in glassy polyisoprene: A neutron backscattering investigation. *Macromolecules*, 27(4):974–980, 1994.
- [114] J. H. Roh, J. E. Curtis, V. N. Novikov, I. Peral, Z. Chowdhuri, R. B. Gregory, and A. P. Sokolov. Influence of hydration on the dynamics of lysozyme. *Biophysical Journal*, 91(7):2573–2588, 2006.

- [115] C. Zhang, V. Arrighi, S. Gagliardi, I. J. McEwen, J. Tanchawanich, M. T. F. Telling, and J.-M. Zanotti. Quasielastic neutron scattering measurements of fast process and methyl group dynamics in glassy poly(vinyl acetate). *Chemical Physics*, 328(1–3):53–63, 2006.
- [116] A.-C. Genix, A. Arbe, J. Colmenero, J. Wuttke, and D. Richter. Neutron scattering and X-ray investigation of the structure and dynamics of poly(ethyl methacrylate). *Macromolecules*, 45(5):2522–2536, 2012.
- [117] S. König, E. Sackmann, D. Richter, R. Zorn, C. Carlile, and T. M. Bayerl. Molecular dynamics of water in oriented DPPC multilayers studied by quasielastic neutron scattering and deuteriumnuclear magnetic resonance relaxation. *The Journal of Chemical Physics*, 100(4):3307–3316, 1994.
- [118] C. Toubin, S. Picaud, P. N. M. Hoang, C. Girardet, B. Demirdjian, D. Ferry, and J. Suzanne. Dynamics of ice layers deposited on MgO(001): Quasielastic neutron scattering experiments and molecular dynamics simulations. *The Journal of Chemical Physics*, 114(14):6371–6381, 2001.
- [119] L. E. Bove, S. Klotz, Th. Strässle, M. Koza, J. Teixeira, and A. M. Saitta. Translational and rotational diffusion in water in the gigapascal range. *Physical Review Letters*, 111(18):185901, 2013.
- [120] F. Volino and A.J. Dianoux. Neutron incoherent scattering law for diffusion in a potential of spherical symmetry: general formalism and application to diffusion inside a sphere. *Molecular Physics*, 41(2):271–279, 1980.
- [121] M. Trapp, T. Gutberlet, F. Juranyi, T. Unruh, B. Demé, M. Tehei, and J. Peters. Hydration dependent studies of highly aligned multilayer lipid membranes by neutron scattering. *The Journal of Chemical Physics*, 133(16):164505, 2010.
- [122] F. Volino, J.-C. Perrin, and S. Lyonnard. Gaussian model for localized translational motion: Application to incoherent neutron scattering. *The Journal of Physical Chemistry B*, 110(23):11217–11223, 2006.
- [123] J.-C. Perrin, S. Lyonnard, F. Volino, and A. Guillermo. Gaussian model for localized translational motion. application to water dynamics in Nafion® studied by quasi-elastic neutron scattering. *The European Physical Journal Special Topics*, 141(1):57–60, 2007.
- [124] J.-C. Perrin, S. Lyonnard, and F. Volino. Quasielastic neutron scattering study of water dynamics in hydrated Nafion membranes. *The Journal of Physical Chemistry C*, 111(8):3393–3404, 2007.
- [125] J. P. Embs, T. Burankova, E. Reichert, and R. Hempelmann. Cation dynamics in the pyridinium based ionic liquid 1-n-butylpyridinium bis((trifluoromethyl)sulfonyl) as seen by quasielastic neutron scattering. *The Journal of Physical Chemistry B*, 116(44):13265–13271,

- 2012.
- [126] K. M. Docherty, J. K. Dixon, and C. F. Kulpa Jr. Biodegradability of imidazolium and pyridinium ionic liquids by an activated sludge microbial community. *Biodegradation*, 18(4):481–493, 2007.
- [127] R. Kawano, H. Matsui, C. Matsuyama, A. Sato, Md. Abu Bin Hasan Susan, N. Tanabe, and M. Watanabe. High performance dye-sensitized solar cells using ionic liquids as their electrolytes. *Journal of Photochemistry and Photobiology A: Chemistry*, 164(1–3):87–92, 2004.
- [128] M.-A. Néouze, J. Le Bideau, and A. Vioux. Versatile heat resistant solid electrolytes with performances of liquid electrolytes. *Progress in Solid State Chemistry*, 33(2–4):217–222, 2005.
- [129] T. L. Greaves and C. J. Drummond. Protic ionic liquids: Properties and applications. *Chemical Reviews*, 108:206–237, 2008.
- [130] M. Martinez, Y. Molmeret, L. Cointeaux, C. Iojoiu, J.-C. Lepretre, N. El Kissi, P. Judeinstein, and J.-Y. Sanchez. Proton-conducting ionic liquid-based proton exchange membrane fuel cell membranes: The key role of ionomerionic liquid interaction. *Journal of Power Sources*, 195(18):5829–5839, 2010.
- [131] C. Iojoiu, M. Hana, Y. Molmeret, M. Martinez, L. Cointeaux, N. El Kissi, J. Teles, J.-C. Lepretre, P. Judeinstein, and J.-Y. Sanchez. Ionic liquids and their hosting by polymers for HT-PEMFC membranes. *Fuel Cells*, 10(5):778–789, 2010.
- [132] Q.-S. Liu, M. Yang, P.-F. Yan, X.-M. Liu, Z.-C. Tan, and U. Welz-Biermann. Density and surface tension of ionic liquids [C_nPy][NTf₂] (n = 2, 4, 5). *The Journal of Chemical & Engineering Data*, 55(11):4928–4930, 2010.
- [133] N. M. Yunus, M.I. A. Mutalib, Z. Man, M. Azmi Bustam, and T. Murugesan. Thermophysical properties of 1-alkylpyridinium bis(trifluoromethylsulfonyl)imide ionic liquids. *The Journal of Chemical Thermodynamics*, 42(4):491–495, 2010.
- [134] H. Tokuda, K. Ishii, Md. Abu Bin Hasan Susan, S. Tsuzuki, K. Hayamizu, and M. Watanabe. Physicochemical properties and structures of room-temperature ionic liquids. 3. Variation of cationic structures. *The Journal of Physical Chemistry B*, 110(6):2833–2839, 2006.
- [135] J.-P. Belieres and C. A. Angell. Protic ionic liquids: Preparation, characterization, and proton free energy level representation. *The Journal of Physical Chemistry B*, 111(18):4926–4937, 2007.
- [136] C. Iojoiu, M. Martinez, M. Hanna, Y. Molmeret, L. Cointeaux, J.-C. Lepretre, N. El Kissi, J. Guindet, P. Judeinstein, and J.-Y. Sanchez. PILs-based Nafion membranes: a route to high-temperature PEFMCs dedicated to electric and hybrid vehicles. *Polymers for Advanced Technologies*, 19(10):1406–1414, 2008.

- [137] H. Tokuda, S. Tsuzuki, Md. Abu Bin Hasan Susan, K. Hayamizu, and M. Watanabe. How ionic are room-temperature ionic liquids? An indicator of the physicochemical properties. *The Journal of Physical Chemistry B*, 110(39):19593–19600, 2006.
- [138] F. S. Oliveira, M. G. Freire, P. J. Carvalho, J. A. P. Coutinho, J. N. Canongia Lopes, L. P. N. Rebelo, and I. M. Marrucho. Structural and positional isomerism influence in the physical properties of pyridinium NTf₂-based ionic liquids: Pure and water-saturated mixtures. *The Journal of Chemical & Engineering Data*, 55(10):4514–4520, 2010.
- [139] V. Di Noto, E. Negro, J.-Y. Sanchez, and C. Iojoiu. Structure-relaxation interplay of a new nanostructured membrane based on tetraethylammonium trifluoromethanesulfonate ionic liquid and neutralized Nafion 117 for high-temperature fuel cells. *Journal of the American Chemical Society*, 132(7):2183–2195, 2010.
- [140] Y. Imai, H. Abe, T. Goto, Y. Yoshimura, S. Kushiyama, and H. Matsumoto. Orientational ordering of crystal domains in ionic liquid based mixtures. *The Journal of Physical Chemistry B*, 112(32):9841–9846, 2008.
- [141] FOCUS: time-of-flight spectrometer. <http://www.psi.ch/sinq/focus/>, October 2013.
- [142] C. Beck, S. Janssen, B. Groß, and R. Hempelmann. Neutron time-of-flight spectrometer FOCUS at SINQ: results from nanocrystalline matter studies. *Scripta Materialia*, 44(8–9):2309–2313, 2001.
- [143] J. Mesot, S. Janssen, L. Holitzner, and R. Hempelmann. FOCUS: Project of a space and time focussing time-of-flight spectrometer for cold neutrons at the spallation source SINQ of the Paul Scherrer Institute. *Journal of Neutron Research*, 3(4):293–310, 1996.
- [144] Disk chopper time-of-flight spectrometer IN5. <http://www.ill.eu/en/instruments-support/instruments-groups/instruments/in5/characteristics/>, November 2013.
- [145] TOFTOF – cold neutron time-of-flight spectrometer. <http://www.mlz-garching.de/toftof>, November 2013.
- [146] D7 – Diffuse Scattering Spectrometer. <http://www.ill.eu/?id=13310>, October 2013.
- [147] Cold neutron backscattering spectrometer IN10. <http://www.ill.eu/instruments-support/instruments-groups/instruments/in10/>, October 2013.
- [148] R. C. G. Killeen. An investigation of the Debye-Waller factor and Debye temperature of aluminium using nearest neighbour central force pair interactions. *Journal of Physics F: Metal Physics*, 4(11):1908–1915, 1974.
- [149] R. Zorn. On the evaluation of neutron scattering elastic scan data. *Nuclear Instruments and Methods in Physics Research A*, 603(3):439–445, 2009.

- [150] F. Gabel. Protein dynamics in solution and powder measured by incoherent elastic neutron scattering: the influence of Q-range and energy resolution. *European Biophysics Journal*, 34(1):1–12, 2005.
- [151] R. E. Lechner, H. J. Bleif, H. Dachs, R. Marx, M. Stahn, and I. Anderson. Two-dimensional proton diffusion in CsH₃O₂. *Solid State Ionics*, 46(1–2):25–32, 1991.
- [152] D. Richter, M. Monkenbusch, A. Arbe, and J. Colmenero. Neutron spin echo in polymer systems. *Advances in Polymer Science*, 174:1–221, 2005.
- [153] D. Richter, M. Monkenbusch, and D. Schwahn. Neutron scattering. *Polymer Science: A Comprehensive Reference*, 10(2):331–361, 2012.
- [154] H. H. Paalman and C. J. Pings. Numerical evaluation of X-ray absorption factors for cylindrical samples and annular sample cells. *Journal of Applied Physics*, 33(8):2635–2639, 1962.
- [155] R. T. Azuah, L. R. Kneller, Y. Qiu, P. L. W. Tregenna-Piggott, C. M. Brown, J. R. D. Copley, and R. M. Dimeo. DAVE: A comprehensive software suite for the reduction, visualization, and analysis of low energy neutron spectroscopic data. *Journal of Research of the National Institute of Standards and Technology*, 114(6):341–358, 2009.
- [156] D. Richard, M. Ferrand, G. J. Kearley, and A. D. Bradley. The Lamp book. <http://www.i11.eu/?id=2024>, 2013.
- [157] R. Hempelmann. Diffusion of hydrogen in metals. *Journal of the Less Common Metals*, 101:69–96, 1984.
- [158] Th. Matzke, U. Stimming, Ch. Karmonik, M. Soetratmo, R. Hempelmann, and F. Güthoff. Quasielastic thermal neutron scattering experiment on the proton conductor SrCe_{0.95}Yb_{0.05}H_{0.02}O_{2.985}. *Solid State Ionics*, 86–88:621–628, 1996.
- [159] C. B. Markwardt. Non-linear least squares fitting in IDL with MPFIT. *Astronomical Data Analysis Software and Systems XVIII*, 411:251–254, 2009.
- [160] IDL curve fitting and function optimization. <http://www.physics.wisc.edu/~craigm/idl/fitting.html>, October 2013.
- [161] J. Moré. The Levenberg-Marquardt algorithm: Implementation and theory. *Numerical Analysis*, 630:105–116, 1978.
- [162] R. M. Dimeo. Application development in IDL I. http://www.ncnr.nist.gov/dave/documentation/intro_to_idl1.pdf, September 2011.
- [163] R. M. Dimeo. Application development in IDL II. http://www.ncnr.nist.gov/dave/documentation/intro_to_idl2.pdf, September 2011.
- [164] S. Tsuzuki. Factors controlling the diffusion of ions in ionic liquids. *A European Journal of Chemical Physics and Physical Chemistry*, 13(7):1664–1670, 2012.

- [165] S. Tsuzuki, H. Matsumoto, W. Shinoda, and M. Mikami. Effects of conformational flexibility of alkyl chains of cations on diffusion of ions in ionic liquids. *Physical Chemistry Chemical Physics*, 13(13):5987–5993, 2011.
- [166] H. N. Bordallo, D. N. Argyriou, M. Barthés, W. Kalceff, S. Rols, K. W. Herwig, C. Fehr, F. Juranyi, and Tilo Seydel. Hydrogen in N-methylacetamide: Positions and dynamics of the hydrogen atoms using neutron scattering. *The Journal of Physical Chemistry B*, 111(27):7725–7734, 2007.
- [167] J. F. Shackelford and W. Alexander, editors. *The CRC materials science and engineering handbook*. CRC Press, London, 1992.
- [168] T. Becker and J. C. Smith. Energy resolution and dynamical heterogeneity effects on elastic incoherent neutron scattering from molecular systems. *Physical Review E: Statistical, Nonlinear, and Soft Matter Physics*, 67(2):021904, 2003.
- [169] T. Becker, J. A. Hayward, J. L. Finney, R. M. Daniel, and J. C. Smith. Neutron frequency windows and the protein dynamical transition. *Biophysical Journal*, 87(3):1436–1444, 2004.
- [170] G. Zaccai. The case for an empirical 'high-throughput' neutron scattering approach to protein dynamics. *Biological Crystallography*, D66(11):1224–1228, 2010.
- [171] G. Zaccai. Neutron scattering perspectives for protein dynamics. *Journal of Non-Crystalline Solids*, 357(2):615–621, 2011.
- [172] Z. Hu, X. Huang, H. V. R. Annapureddy, and C. J. Margulis. Molecular dynamics study of the temperature-dependent optical Kerr effect spectra and intermolecular dynamics of room temperature ionic liquid 1-methoxyethylpyridinium dicyanoamide. *The Journal of Physical Chemistry B*, 112(26):7837–7849, 2008.
- [173] M. Imanari, K.-i. Uchida, K. Miyano, H. Seki, and K. Nishikawa. NMR study on relationships between reorientational dynamics and phase behaviour of room-temperature ionic liquids: 1-alkyl-3-methylimidazolium cations. *Physical Chemistry Chemical Physics*, 12(12):2959–2967, 2010.
- [174] L. Carpentier, M. Bée, A. M. Giroud-Godquin, P. Maldivi, and J.C. Marchon. Alkyl chain motions in columnar mesophases. A quasielastic neutron scattering study of dicopper tetrapalmitate. *Molecular Physics*, 68(6):1367–1378, 1989.
- [175] R. Mukhopadhyay, S. Mitra, M. Johnson, V. R. Rajeev Kumar, and T. Pradeep. Evolution of the alkyl-chain dynamics in monolayer-protected gold clusters. *Physical Review B: Condensed Matter and Materials Physics*, 75(7):075414, 2007.
- [176] J. P. Embs, E. Reichert, and R. Hempelmann. Dynamics of room temperature ionic liquids by means of quasielastic neutron scattering. *Swiss Neutron News*, 32:4–9, 2007.

- [177] Engineering statistics. <http://www.itl.nist.gov/div898/handbook/eda/section3/eda3669.htm>, February 2014.
- [178] J. Colmenero, A. Arbe, A. Alegría, M. Monkenbusch, and D. Richter. On the origin of the non-exponential behaviour of the α -relaxation in glass-forming polymers: incoherent neutron scattering and dielectric relaxation results. *Journal of Physics: Condensed Matter*, 11(10A):A363–A370, 1999.
- [179] E. Mamontov. Diffusion dynamics of water molecules in a LiCl solution: A low-temperature crossover. *The Journal of Physical Chemistry B*, 113(43):14073–14078, 2009.
- [180] A. Arbe, A.-C. Genix, S. Arrese-Igor, J. Colmenero, and D. Richter. Dynamics in poly(n-alkyl methacrylates): A neutron scattering, calorimetric, and dielectric study. *Macromolecules*, 43(6):3107–3119, 2010.
- [181] A. Arbe, J. Colmenero, F. Alvarez, M. Monkenbusch, D. Richter, B. Farago, and B. Frick. Experimental evidence by neutron scattering of a crossover from Gaussian to non-Gaussian behavior in the α relaxation of polyisoprene. *Physical Review E: Statistical, Nonlinear, and Soft Matter Physics*, 67(5):051802, 2003.
- [182] K. Fumino, E. Reichert, K. Wittler, R. Hempelmann, and Ralf Ludwig. Low-frequency vibrational modes of protic molten salts and ionic liquids: Detecting and quantifying hydrogen bonds. *Angewandte Chemie, International Edition*, 51(25):6236–6240, 2012.
- [183] K. Mori, S. Hashimoto, T. Yuzuri, and Kazuhisa Sakakibara. Structural and spectroscopic characteristics of a proton-conductive ionic liquid diethylmethylammonium trifluoromethanesulfonate [dema][TfOH]. *Bulletin of the Chemical Society of Japan*, 83(4):328–334, 2010.
- [184] K. Mori, T. Kobayashi, K. Sakakibara, and K. Ueda. Experimental and theoretical investigation of proton exchange reaction between protic ionic liquid diethylmethylammonium trifluoromethanesulfonate and H₂O. *Chemical Physics Letters*, 552:58–63, 2012.
- [185] F. N. Keutsch and R. J. Saykally. Water clusters: Untangling the mysteries of the liquid, one molecule at a time. *Proceedings of the National Academy of Sciences of the United States of America*, 98(19):10533–10540, 2001.
- [186] J. Thar, M. Brehm, A. P. Seitsonen, and B. Kirchner. Unexpected hydrogen bond dynamics in imidazolium-based ionic liquids. *The Journal of Physical Chemistry B*, 113(46):15129–15132, 2009.
- [187] H. Chen, T. Yan, and G. A. Voth. A computer simulation model for proton transport in liquid imidazole. *The Journal of Physical Chemistry A*, 113(16):4507–4517, 2009.
- [188] S. Tsuzuki, W. Shinoda, Md. Shah Miran, H. Kinoshita, T. Yasuda, and M. Watanabe. Interactions in ion pairs of protic ionic liquids: Comparison with aprotic ionic liquids. *The Journal of Chemical Physics*, 139(17):174504, 2013.

- [189] E. W. Castner Jr., C. J. Margulis, M. Maroncelli, and J. F. Wishart. Ionic liquids: Structure and photochemical reactions. *Annual Review of Physical Chemistry*, 62:85–105, 2011.
- [190] O. Russina, A. Triolo, L. Gontrani, and R. Caminiti. Mesoscopic structural heterogeneities in room-temperature ionic liquids. *The Journal of Physical Chemistry Letters*, 3:27–33, 2012.
- [191] O. Russina and A. Triolo. New experimental evidence supporting the mesoscopic segregation model in room temperature ionic liquids. *Faraday Discussions*, 154:97–109, 2012.
- [192] H. V. R. Annapureddy, H. K. Kashyap, P. M. De Biase, and C. J. Margulis. What is the origin of the prepeak in the X-ray scattering of imidazolium-based room-temperature ionic liquids? *The Journal of Physical Chemistry B*, 114(50):16838–16846, 2010.
- [193] K. Sköld, J. M. Rowe, G. Ostrowski, and P. D. Randolph. Coherent- and incoherent-scattering laws of liquid argon. *Physical Review A: Atomic, Molecular, and Optical Physics*, 6(3):1107–1131, 1972.
- [194] M. D. Ruiz-Martn, M. Jimenez-Ruiz, A. Stunault, F. J. Bermejo, R. Fernandez-Perea, and C. Cabrillo. Stochastic dynamics in molten potassium explored by polarized quasielastic neutron scattering. *Physical Review B: Condensed Matter and Materials Physics*, 76(17):174201, 2007.
- [195] J. C. Cook, D. Richter, O. Scharpf, M. J. Benham, D. K. Ross, R. Hempelmann, I. S. Anderson, and S. K. Sinha. A study of tracer and collective diffusional processes in α' -NbD_{0.7} at 600 K using quasielastic neutron scattering with spin analysis. *Journal of Physics: Condensed Matter*, 2(1):79–94, 1990.
- [196] J. C. Cook, D. Richter, R. Hempelmann, D. K. Ross, and H. Züchner. Quasi-elastic neutron scattering studies of collective and correlated tracer diffusion in the systems α' -NbD_x and α' -NbH_x. *Journal of the Less Common Metals*, 172–174:585–594, 1991.
- [197] D. A. Neumann, J. R. D. Copley, R. L. Cappelletti, W. A. Kamitakahara, R. M. Lindstrom, K. M. Creegan, D. M. Cox, W. J. Romanow, N. Coustel, J. P. McCauley, N. C. Maliszewskyj, J. E. Fischer, and A. B. Smith. Coherent quasielastic neutron scattering study of the rotational dynamics of C60 in the orientationally disordered phase. *Physical Review Letters*, 67(27):3808–3811, 1991.
- [198] G. H. Vineyard. Scattering of slow neutrons by a liquid. *Physical Review*, 110(5):999–1010, 1958.
- [199] K. Sköld. Small energy transfer scattering of cold neutrons from liquid argon. *Physical Review Letters*, 19(18):1023–1025, 1967.
- [200] M. Leitner and G. Vogl. Quasi-elastic scattering under short-range order: the linear regime and beyond. *Journal of Physics: Condensed Matter*, 23(25):254206, 2011.

-
- [201] C. Schröder. Collective translational motions and cage relaxations in molecular ionic liquids. *The Journal of Chemical Physics*, 135(2):024502, 2011.